РОССИЙСКИЙ ГОСУДАРСТВЕННЫЙ ПЕДАГОГИЧЕСКИЙ УНИВЕРСИТЕТ им. А. И. ГЕРЦЕНА
HERZEN STATE PEDAGOGICAL UNIVERSITY of RUSSIA

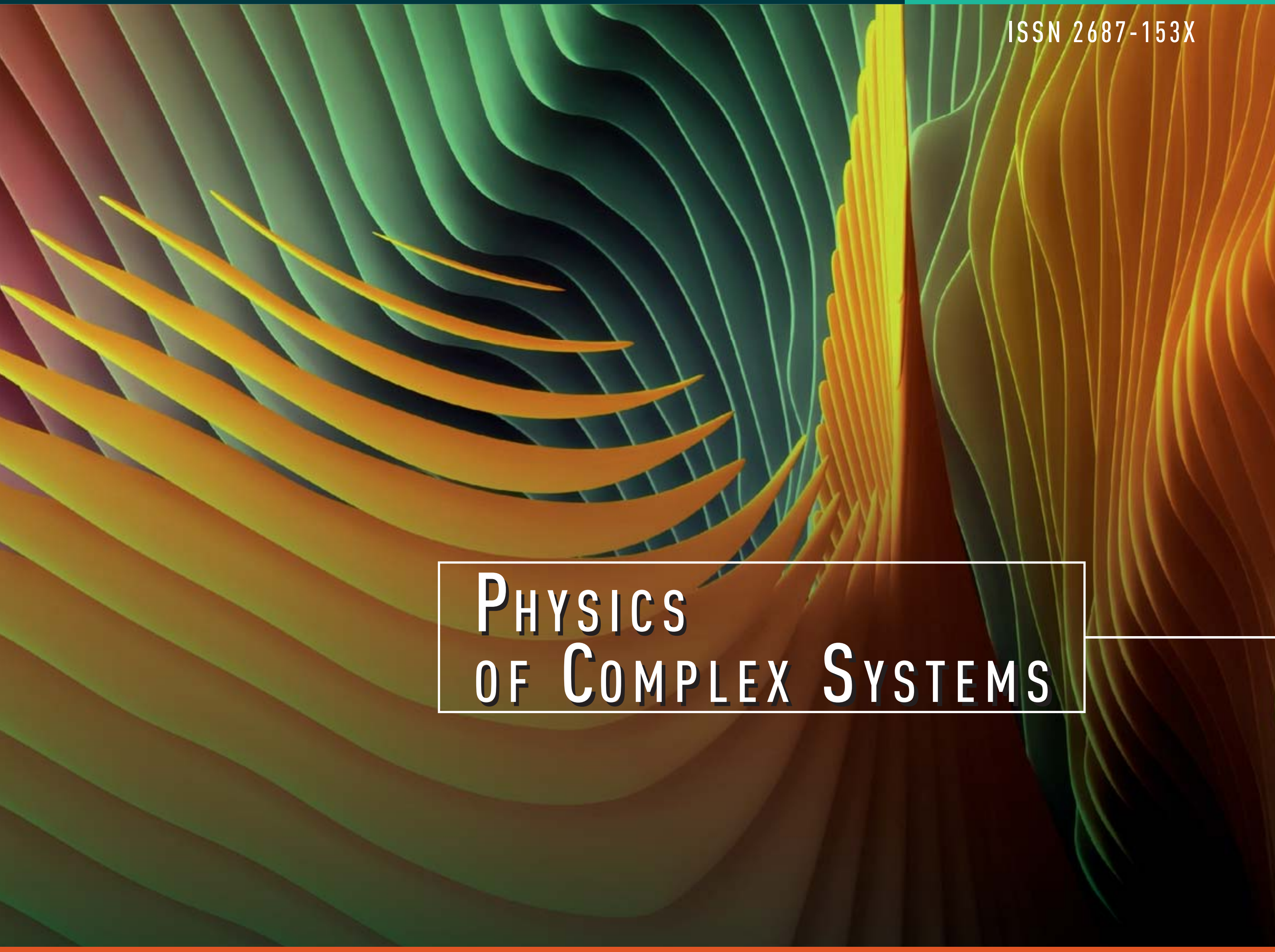

ISSN 2687-153X

PHYSICS OF COMPLEX SYSTEMS

Т. 4 № 3 2023

VOL. 4 NO. 3 2023

1797

Herzen State Pedagogical University of Russia

ISSN 2687-153X (online)
physcomsys.ru
https://www.doi.org/10.33910/2687-153X-2023-4-3
2023. Vol. 4, no. 3

PHYSICS OF COMPLEX SYSTEMS

Mass Media Registration Certificate El No. FS77-77889, issued by Roskomnadzor on 10 February 2020
Peer-reviewed journal
Open Access
Published since 2020
4 issues per year

Editorial Board
Editor-in-chief Alexander V. Kolobov (Saint Petersburg, Russia)
Deputy Editor-in-chief Andrey K. Belyaev (Saint Petersburg, Russia)
Deputy Editor-in-chief Yuri A. Gorokhovatsky (Saint Petersburg, Russia)
Executive Secretary Alexey A. Kononov (Saint Petersburg, Russia)
Vachagan T. Avanesyan (Saint Petersburg, Russia)
Alexander P. Baraban (Saint Petersburg, Russia)
Sergey P. Gavrilov (Saint Petersburg, Russia)
Dmitry M. Gitman (São Paulo, Brazil)
Vladimir M. Grabov (Saint Petersburg, Russia)
Andrey A. Grib (Saint Petersburg, Russia)
Elisabeth Dalimier (Paris, France)
Alexander Z. Devdariani (Saint Petersburg, Russia)
Vadim K. Ivanov (Saint Petersburg, Russia)
Rene A. Castro Arata (Saint Petersburg, Russia)
Miloš Krbal (Pardubice, the Czech Republic)
Sergey A. Nemov (Saint Petersburg, Russia)
Oleg Yu. Prikhodko (Almaty, Kazakhstan)
Igor P. Pronin (Saint Petersburg, Russia)
Mikhail Yu. Puchkov (Saint Petersburg, Russia)
Alexey E. Romanov (Saint Petersburg, Russia)
Pavel P. Seregin (Saint Petersburg, Russia)
Koichi Shimakawa (Gifu, Japan)

Advisory Board
Gennady A. Bordovsky (Saint Petersburg, Russia)
Alexander V. Ivanchik (Saint Petersburg, Russia)
Vladimir V. Laptev (Saint Petersburg, Russia)
Alexander S. Sigov (Moscow, Russia)

Publishing house of Herzen State Pedagogical University of Russia
48 Moika Emb., Saint Petersburg 191186, Russia
E-mail: izdat@herzen.spb.ru
Phone: +7 (812) 312-17-41

Data size 3,05 Mbyte
Published at 07.09.2023

The contents of this journal may not be used in any way without a reference to the journal
“Physics of Complex Systems” and the author(s) of the material in question.

Editor of the English text *I. A. Nagovitsyna*
Corrector *E. V. Novoseltseva*
Cover design by *O. V. Rudneva*
Layout by *A. M. Khodan, L. N. Kliuchanskaya*

Saint Petersburg, 2023
© Herzen State Pedagogical University of Russia, 2023

CONTENTS

In memory of Yuri Andreevich Gorokhovatsky
(17.11.1946 – 09.08.2023)

On August 9, 2023, a renowned scientist and educator, Doctor of Physical and Mathematical Sciences, Professor, Director of the Research Institute of Physics, Head of the Department of General and Experimental Physics of the Herzen State Pedagogical University of Russia, one of the founders of the *journal "Physics of Complex Systems",* Yuri Andreevich Gorokhovatsky passed away.

Professor Gorokhovatsky held the position of Head of the Department of General and Experimental Physics at the Herzen State Pedagogical University of Russia from 1991. Yu. A. Gorokhovatsky showed his bright organization skills during the difficult years of perestroika and the collapse of the USSR when he not only managed to preserve the potential of the physical laboratories, but also succeeded to enhance it to meet the new requirements for educating and training teachers of Physics.

A talented experimental physicist, Yuri Andreevich ran a number of laboratories at the Herzen State Pedagogical University of Russia, where he conducted research based on the methods of thermal activation spectroscopy developed by himself in line with modern trends in dielectric physics. He actively involved students and postgraduates of the faculty in research work in the laboratories.

In May 2007, due to the enthusiasm and hard work of Yuri Andreevich, a Research Institute of Physics was established on the basis of the research laboratories of the Faculty (now the Institute) of Physics of the Herzen State Pedagogical University of Russia. Since its inception, Yuri Andreevich was the head of the Research Institute. Under his leadership the Research Institute was intensively developing, and in 2021, it has become a research center that includes three departments and five centers for collective research.

Yuri Andreevich was a talented lecturer and a considerate mentor throughout his pedagogical career. Over the past twenty years, he was a scientific supervisor of 15 PhD candidates and 2 doctorates in physical and mathematical sciences. As deputy chairman of the dissertation council, head of the postgraduate educational program on Condensed Matter Physics, deputy editor-in-chief of the scientific *journal "Physics of Complex Systems"*, Professor Gorokhovatsky contributed significantly to the development of Russian science.

During the years of work at the higher school, Yuri Andreevich was the author of textbooks on general physics that provide a comprehensive treatment of the basic principles and phenomena.

For many years, Yu. A. Gorokhovatsky was an organizer of the international scientific conferences "Physics of Dielectrics" and "Physics in the system of modern education", which enhanced the role of the Herzen State Pedagogical University of Russia in these scientific fields.

The merits of Yu. A. Gorokhovatsky in the field of development of science and education received well-deserved recognition. By decree of the President of the Russian Federation, he received the honorary title Honored Scientist of the Russian Federation.

The Herzen State Pedagogical University of Russia acknowledged the outstanding achievements of Yuri Andreevich by conferring on him the title of "Honorary Professor of the Herzen State Pedagogical University of Russia", awarding him the medal in honor of I.I. Betskoy and the medal "For Achievements in the field of science and education".

Yuri Andreevich's colleagues at the institute of Physics of the Herzen State Pedagogical University mourn the irreparable loss and express sincere condolences to the family of Yuri Andreevich.

Physics of Complex Systems, 2023, vol. 4, no. 3
www.physcomsys.ru

Check for updates

Condensed Matter Physics. Phase equilibria and phase transitions

UDC 537.311

EDN TODSJI
https://www.doi.org/10.33910/2687-153X-2023-4-3-94-102

Direct synthesis of Mg_2NiH_4 from MgH_2 and Ni

A. P. Baraban✉[1], V. A. Dmitriev[1], I. E. Gabis[1], A. P. Voyt[1], S. N. Klyamkin[2], I. V. Shikin[1]

[1] Saint-Petersburg State University, 7/9 Universitetskaya Emb., Saint Petersburg 199034, Russia
[2] M. V. Lomonosov Moscow State University, 1 Leninskie Gory, Moscow 119991, Russia

Authors
Alexander P. Baraban, ORCID: 0000-0001-8745-7019, e-mail: alnbaraban@yandex.ru
Valentin A. Dmitriev, ORCID: 0000-0003-3604-9490, e-mail: esssec@gmail.com
Igor E. Gabis, ORCID: 0000-0002-9347-1092, e-mail: igor.gabis@gmail.com
Alexey P. Voyt, ORCID: 0000-0001-9568-0376, e-mail: voytalexey@mail.ru
Semen N. Klyamkin, ORCID: 0000-0001-6009-1045, e-mail: klyamkin@highp.chem.msu.ru
Ilia V. Shikin, ORCID: 0000-0002-1691-0186, e-mail: shikin_ilya@mail.ru

For citation: Baraban, A. P., Dmitriev, V. A., Gabis, I. E., Voyt, A. P., Klyamkin, S. N., Shikin, I. V. (2023) Direct synthesis of Mg_2NiH_4 from MgH_2 and Ni. *Physics of Complex Systems*, 4 (3), 94–102. https://www.doi.org/10.33910/2687-153X-2023-4-3-94-102 EDN TODSJI

Received 13 June 2023; reviewed 5 July 2023; accepted 5 July 2023.

Funding: The study did not receive any external funding.

Abstract. We showed that the exposure of a pressed mixture of MgH_2 and Ni powders to a hydrogen atmosphere at 450 °C leads to the direct formation of Mg_2NiH_4. No pre-milling was used. The reaction was carried out at a hydrogen pressure exceeding the equilibrium over MgH_2 and Mg_2NiH_4. The pressure invariability during the synthesis evidences the absence of a separate stage of magnesium hydride decomposition and stabilization of the synthesized hydride. The amount of Mg_2NiH_4 was determined by the XRD and TDS methods. SEM with EDX microanalysis was used to examine the morphology of the reaction products. The influence of the exposure time and the synthesis temperature on the reaction yield was studied.

Keywords: metal hydrides, hydrogen storage materials, solid-state direct synthesis, triple hydride Mg_2NiH_4, intermetallide $MgNi_2$

Introduction

Mg_2NiH_4 is of interest for solid-state hydrogen storage and electrochemical application. It contains up to 3.6 wt.% of hydrogen. Compared with MgH_2, Mg_2NiH_4 has better kinetics of hydrogen absorption and desorption, and a lower temperature (223 °C) corresponding to the equilibrium with the gaseous phase at the pressure of 1 bar. Sustainability in the course of hydrogenation/dehydrogenation cycling is an additional advantage for practical use.

After the article (Reilly, Wiswall 1968) showed that the interaction of intermetallic compound Mg_2Ni with hydrogen results in the reversible formation of Mg_2NiH_4, this route of synthesis was chosen as the primary one. Mg_2Ni can be obtained by laboratory methods (for example, alloying in an induction furnace under argon (Reilly, Wiswall 1968), bulk mechanical alloying and conventional casting techniques (Blomqvist, Noréus 2002; Blomqvist et al. 2002; Mulas et al. 2008)), however, in most cases the commercial-grade material is used.

In addition to hydrogenation of Mg_2Ni, alternative routes for synthesis of Mg_2NiH_4 from MgH_2 and Ni are being actively explored. Most of these studies involve the decomposition of magnesium hydride as an intermediate stage.

The hydriding combustion method reported in (Akiyama et al. 1997;1998; Li et al. 1999; 2001; 2004; 2005; Saita et al. 2003) represents the synthesis of Mg_2NiH_4 as a series of successive chemical transformations. A powdered mixture of MgH_2 and Ni was subjected to heating up to 567 °C that led to the decomposition of MgH_2 and formation of Mg_2Ni intermetallic compounds from metallic magnesium and nickel. Subsequent cooling in a hydrogen atmosphere results in hydrogen absorption by the intermetallic compound. Thus, the Mg_2NiH_4 ternary hydride is the product of the following multistage process:

$$2MgH_2 + Ni \rightarrow 2Mg + 2H_2 + Ni \rightarrow Mg_2Ni + 2H_2 \rightarrow Mg_2NiH_4 \qquad (1)$$

Another synthesis method based on high-energy ball milling was described in (Martinez-Coronado et al. 2012; Orimo et al. 1997; Polanski et al. 2013). Taking into account the known non equilibrium processes occurring during ball milling and the probability of significant local overheating under these conditions, it is natural to assume a partial decomposition of the hydride and, therefore, the formation of a metal phase. So, the authors' statement about "direct reaction" is questionable.

Herein, we demonstrate another synthesis route of Mg_2NiH_4 through direct reaction of magnesium hydride with metallic nickel under moderate pressure-temperature conditions without the intermediate stage of MgH_2 decomposition. In (Kataoka et al. 2007; Martinez-Coronado et al. 2013; Takamura et al. 2002), similar quasi-hydrostatic syntheses under ultra-high pressures (2–5 GPa) have been reported. We have to note here that there are no available data on the phase behavior of MgH_2 at the experimental temperatures (700–800 °C) exceeding the magnesium melting point (650 °C). The obvious impossibility of the *in-situ* control of the course of reaction provides no insights into its possible mechanism. Although the thermodynamic estimation shows that the reaction does not require such harsh conditions, this has never been confirmed experimentally.

In contrast to such rigid conditions of synthesis we found that this reaction occurs at a temperature of 450 °C and hydrogen pressures exceeding the equilibrium decomposition pressures of Mg_2NiH_4 and MgH_2. Such solid-phase interaction that proceeds at a sufficiently low temperature without any intensive mechanical or catalytic assistance is of interest. It should involve mutual penetration of nickel with a melting point of 1453 °C and MgH_2, a salt-like substance, via Mg_2NiH_4. The latter, according to (Blomqvist, Noréus 2002; Humphries et al. 2017), is an insulator at 450 °C.

In (Baraban et al. 2022), the growth of hydride film Mg_2NiH_4 on the flat surface of nickel foil at 450 °C was considered upon interaction with MgH_2 powder in hydrogen at pressures exceeding, as in the present study, the decomposition pressures of MgH_2 and Mg_2NiH_4. The flat configuration of the substrate-film system allowed the growth mechanism to be established. The kinetics of the increasing amount of the reacted fraction (RF) and XRD results obtained in the present work using powders allow us to state that the mechanism of Mg_2NiH_4 hydride synthesis is similar to that described in (Baraban et al. 2022).

Materials and methods

We used the following methods and equipment. The phase composition and the hydrogen content were determined by 2 ways. i) X-Ray Diffraction (XRD) method using the Bruker "D2 Phaser" (Cu) diffractometer (TOPAS software and Rietveld method). ii) Thermal Desorption Spectrometry (TDS) using custom-built vacuum equipment with RGA100 (Stanford Research Systems). The analytical capabilities of Scanning Electron Microscopy (SEM) using the Carl Zeiss Merlin microscope were expanded with additional X-ray energy dispersive microanalysis system by Oxford Instruments INCAx-act for Energy-Dispersive X-ray spectroscopy (EDX).

Magnesium hydride was synthesized in a high-pressure setup by direct hydrogenation of 99.2% pure magnesium powder with the average particle size of 50–100 micron. The synthesis was performed at pressures of 40–60 bar and temperatures of 420–450 °C. According to XRD and TDS analysis, the hydrogenated samples contain 6.9–7.3 mass% of hydrogen that corresponds to H/Mg ratio of 1.8–1.9. The presence of metallic magnesium and magnesium oxide in the main MgH_2 phase has been detected by XRD. The second reagent for the Mg_2NiH_4 synthesis was nickel powder with the purity of 99.92% and the average particle size of 5 μm.

The preparation of samples for the Mg_2NiH_4 synthesis involved thorough mixing of the MgH_2 and Ni powders at the molar ratio of 2:1 and their subsequent pressing to the density of 1.9 ± 0.1 g/cm^3, which corresponds to 70–75% of the theoretic one for the studied composition. The mass of the samples was in the range of 0.2–0.5 g. The detailed description of the equipment and the pressing procedure was previously reported in (Elets et al. 2017).

According to the SEM data, after pressing the material is represented by large MgH_2 particles with finer nickel particles embedded between them (Fig. 1).

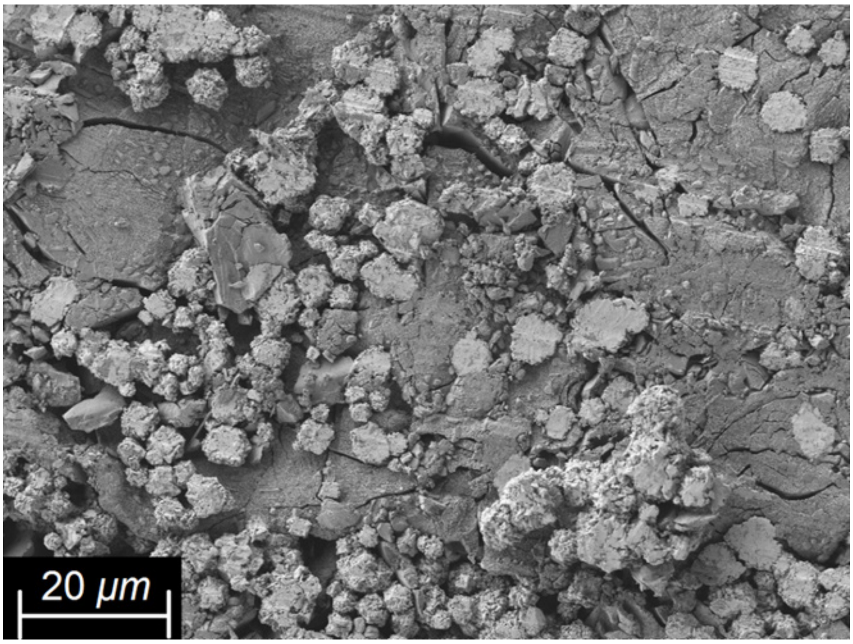

Fig. 1. SEM of the pressed MgH_2+Ni mixture

The idea of the direct synthesis of Mg_2NiH_4 comes down to a solid-state reaction at a hydrogen pressure high enough to avoid the decomposition of both MgH_2 (the initial reagent) and Mg_2NiH_4 (the reaction product). There are no equilibrium hydrogen pressures for these hydrides for the temperature range over 400 °C reported in the literature. Maximum temperatures are 350 °C for MgH_2 (Leng et al. 2014) and 365 °C for Mg_2NiH_4 (Revesz et al. 2017). In this regard, equilibrium pressures for the temperatures of 400, 425, and 450 °C were determined in preliminary experiments on the decomposition of Mg_2NiH_4 and MgH_2. They approximately correspond to the middle part of the desorption branches of the P-C diagrams. The results are shown in Table 1. They correlate with the extrapolation of data from the articles (Leng et al. 2014; Revesz et al. 2017) to the indicated temperature range. All the experiments described below were carried out taking these data into account.

Table 1. Hydrogen desorption equilibrium pressures

T, K (T, ^{0}C)	**673 (400)**	**698 (425)**	**723 (450)**
MgH_2- Mg	16	25.5	38
Mg_2NiH_4- Mg_2Ni	22.6	35.1	48.9

The pressed samples were placed in a stainless steel reactor. After vacuuming, the reactor was filled with hydrogen at a pressure exceeding the equilibrium pressure over Mg_2NiH_4 at the experimental temperature in order to prevent its decomposition. The equilibrium pressures of Mg_2NiH_4 are higher than those of MgH_2, so the decomposition of the latter did not occur, either. The temperature was kept constant during the synthesis (400–450 °C) for 2–12 hours, then, the reactor was cooled. A slight increase in the hydrogen pressure during heating complied with the gas laws. During the exposure at the constant temperature, the pressure variations did not exceed 0.2 bar.

Fig. 2 shows the characteristic curves of pressure in the reactor and its temperature in the synthesis process (note a gap on the abscissa axis made for clarity). Initially the sample contained 63.9 mg of nickel and 58.5 mg of MgH_2. A smooth increase in the hydrogen pressure to 67.5 bar when the sample is heated to 450 °C corresponds to a change in pressure when heating an empty reactor. This indicates the absence of decomposition of MgH_2 and synthesized Mg_2NiH_4. In the syntheses described in this article we used hydrogen pressures exceeding the pressures of MgH_2 and Mg_2NiH_4 decomposition.

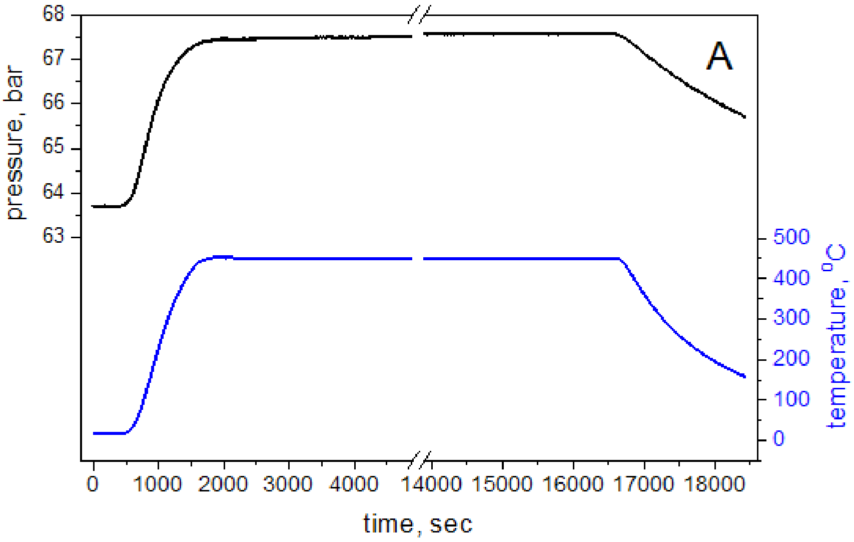

Fig. 2. Pressure and temperature during the synthesis

Results and discussion

The XRD data on the reaction products obtained under different synthesis conditions are presented in Fig. 3. The exposure at 400 °C for 5 hours does not cause visible changes in the phase composition compared with the initial mixture, while an increase to 425 °C results in the formation of Mg_2NiH_4 ternary hydride. The amount of this phase increases significantly with temperature and exposure time, and reaches ~55 mass% after 12 hours at 450 °C. The synthesis parameters and the corresponding phase compositions (in mass%) after 5 hours of exposure are summarized in Table 2. RF stands for the reacted fraction.

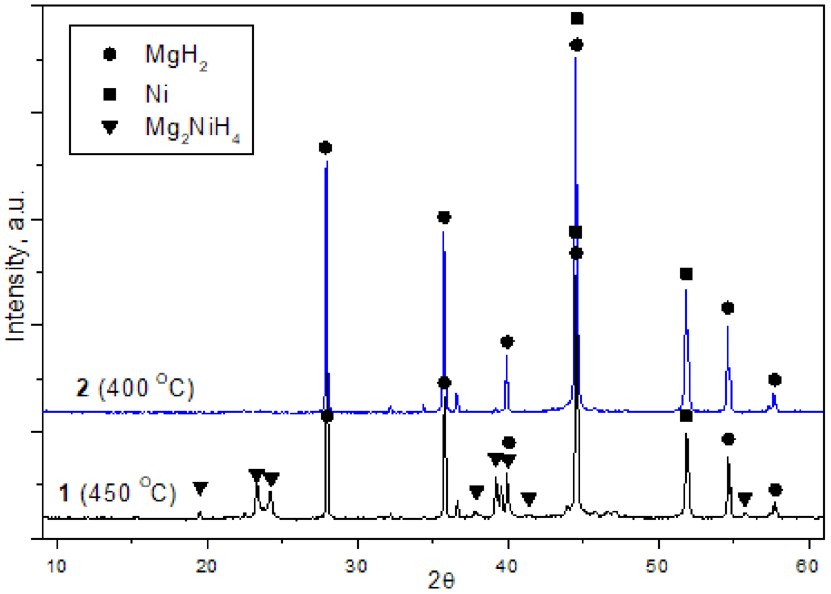

Fig. 3. XRD patterns of the reaction products. Exposure for 5 hours at 450 °C (1) and 400 °C (2)

Table 2. The results of the XRD analysis of reaction products (in percent) and the reacted fraction of Mg_2NiH_4 after a 5-hour exposure at different temperatures and pressures

T, K (T, °C)	**673 (400)**	**698 (425)**	**723 (450)**
P, bar	25.9	39.9	63.4
Phase name (ICDD card number)	mass %		
Mg (03-065-3365)	1.6	1.0	1.3
MgO (01-073-3815)	traces	traces	traces
Ni (03-065-2865)	44.4	36.2	31.8
MgH_2 (01-075-7944)	52.2	52.6	40.5
$MgNi_2$ (03-065-4318)	1.0	1.5	1.7
Mg_2NiH_4 (01-084-0714)	0.0	8.7	24.7
RF	0.0	0.087	0.247

The MgH_2/Mg_2NiH_4 ratio in the synthesis products was also studied by TDS. The typical sample weight was 3–10 mg. In the case of linear heating at a rate of 0.05 K/s, hydrogen evolution from Mg_2NiH_4 in vacuum began at about 200 °C, while the second peak corresponds to the desorption from MgH_2 (Evard et al. 2010). For illustration, Fig. 4 shows the TDS curves for the samples subjected to 3 (A), 6 (B) and 12 (C) hours of exposure at the reaction temperature. The peaks corresponding to Mg_2NiH_4 and MgH_2 decomposition are clearly separated on the TDS curves. This allows evaluating the hydrogen amount related to each of the processes from the peak areas. With an accuracy of 10%, the resulting values agreed with the XRD data.

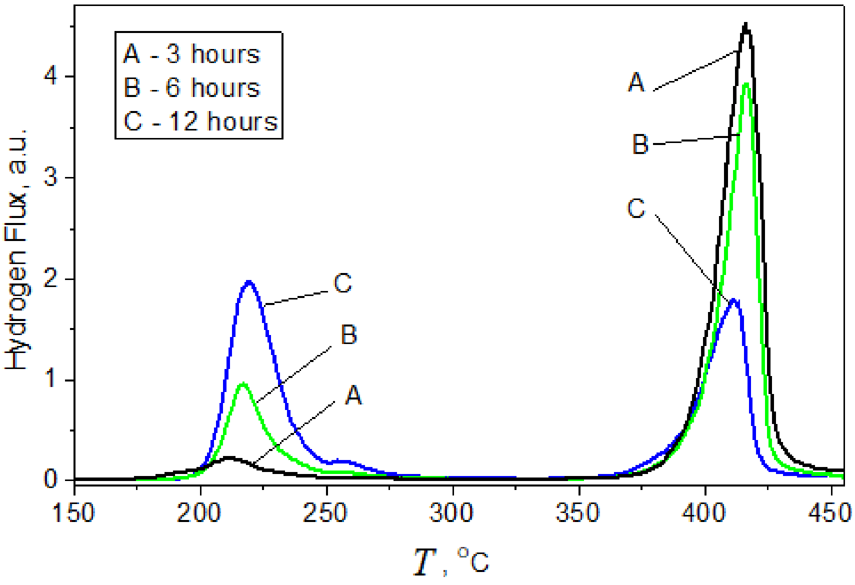

Fig. 4. TDS curves of the samples synthesized for 3 (A), 6 (B) and 12 (C) hours

The SEM image (Fig. 5) demonstrates a significant change in the sample morphology after the synthesis. According to EDX, a large particle in the center contains Mg and Ni at a molar ratio close to 2:1. Smaller particles marked by the arrows at the top right and left contain only Mg (and no Ni). They are likely to refer to the unreacted magnesium hydride.

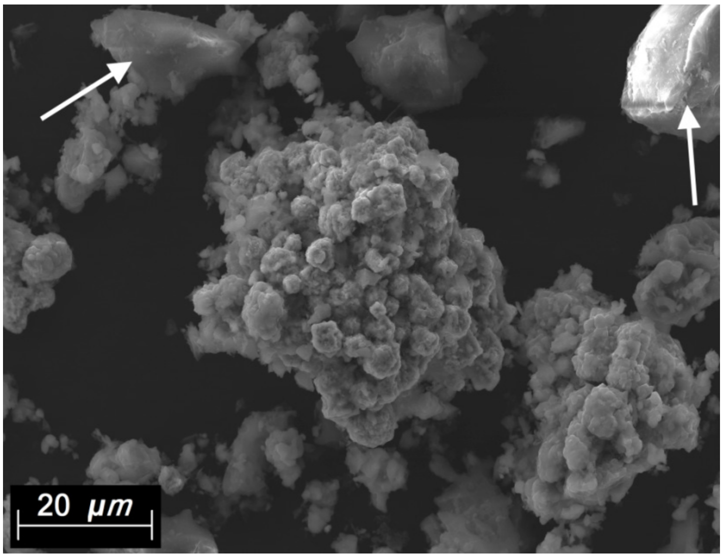

Fig. 5. The SEM image after the synthesis (8 hours, 450 °C)

The influence of the exposure time on the reaction yield was studied in a series of subsequent experiments. They were performed at the temperature of 450 °C under hydrogen pressure exceeding 60 bar. The results calculated from XRD data and expressed in terms of the reacted fraction are shown in Fig. 6. The circles correspond to pressed samples and the squares to unpressed samples. It is worth noting that the same synthesis procedure performed for powder samples, which were not subjected to preliminary pressing, significantly decreased the reaction yield.

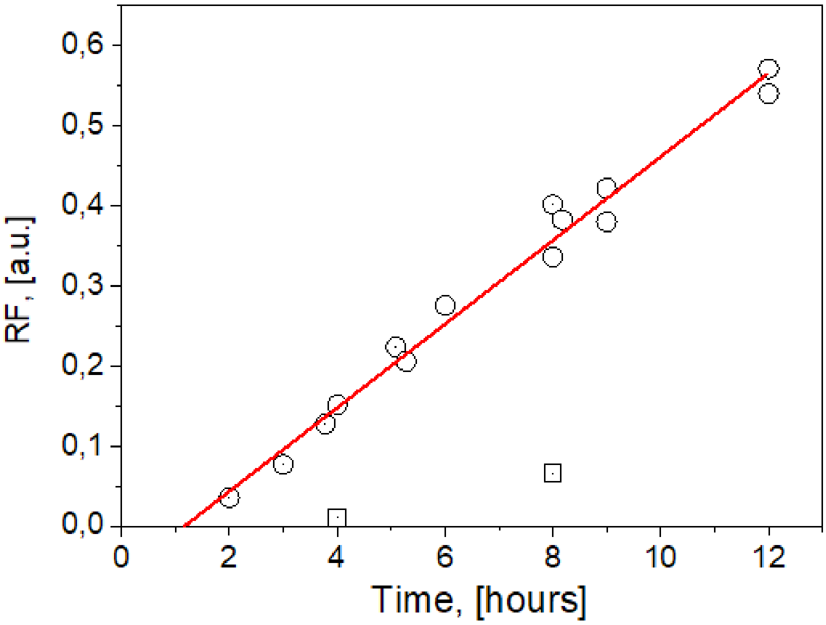

Fig. 6. Reacted fraction of Mg_2NiH_4 synthesis at 450 °C as a function of the exposure time (circles). The squares indicate the unpressed samples

For pressed samples the growth kinetics of the RF is fully consistent with that described in (Baraban et al. 2022) for the same temperature of 450 °C for a planar evolving reaction, namely, linear growth after some delay time (incubation). The red line in the graph represents a linear approximation. The cut-off on the abscissa in our case is 1.16 hours, while it was 1.2 hours in (Baraban et al. 2022), which can be considered a very good match. On the whole, the detailed similarity of the kinetics of the increase in the amount of synthesized Mg_2NiH_4 hydride indicates that the mechanisms of synthesis probably coincide as well.

Using the XRD method it was shown in this paper that the delay before the start of Mg_2NiH_4 synthesis is due to the formation of a Mg_2Ni sublayer. It grows to a certain thickness, after which the growth of Mg_2NiH_4 hydride begins. The Mg_2Ni–Mg_2NiH_4 interfacial boundary was identified as the place of synthesis. The linearity of Mg_2NiH_4 layer thickness increase with the synthesis time was explained by a constant rate of nickel atoms diffusion along the $MgNi_2$ sublayer from the substrate to the Mg_2Ni-Mg_2NiH_4 interface.

The analysis of changes in the synthesis rate due to the time factor for powder samples is radically more complex than that for the planar case. The magnesium hydride and nickel powders are mixed and pressed, but their concentrations can vary in different areas of the sample. Another difference is that for the planar samples the magnesium was supplied from the gas phase, while for the powdered samples the magnesium and nickel were pressed together. Therefore, direct diffusion through the solid is more likely. The supply of magnesium through the gas phase cannot be excluded, either. However, the radically lower synthesis rates for the unpressed samples suggest that this channel of magnesium supply is small.

However, the qualitative coincidence of the synthesis kinetics of powder samples with planar samples suggests that the reaction mechanisms are also similar. Firstly, during the incubation process the intermetallic compound $MgNi_2$ is formed. This process must be associated with the release of some hydrogen. However, the quantity of formed intermetallic compound is small and amounts to 0.5 ± 0.2 mole% for all experimental points, which is negligibly small for our conditions. Note that at the same time the percentage of synthesized Mg_2NiH_4 varies from 1.3 to 40 mole%. Then, at the Mg_2Ni-Mg_2NiH_4 interface the hydride Mg_2NiH_4 is synthesized, through which Mg and H atoms arrive from MgH_2 via the vacancy mechanism. Following (Baraban et al. 2022), we consider that the constant growth rate of the RF is limited by the constant diffusion rate of nickel atoms through the layer of intermetallic compound $MgNi_2$.

The observed chemical transformation can be expressed by equation (2):

$$2MgH_2 + Ni \xrightarrow{H_2} Mg_2NiH_4 \qquad (2)$$

Pressure invariability during the synthesis and, therefore, the absence of hydrogen evolution is the main argument in favor of the suggested reaction scheme.

Thus, using the XRD and TDS techniques, we demonstrate that the solid-state direct synthesis of Mg_2NiH_4 is feasible already at relatively low temperatures starting from 425 °C.

We have to emphasize two main features that are of special interest in the reaction between MgH_2 and Ni.

- Solid-phase interaction proceeds at a sufficiently low temperature without any intensive mechanical or catalytic assistance despite the fact that the reagents are nickel with a melting point of 1453 °C and MgH_2, which is a salt-like substance at 450 °C.
- No pre-milling or ultra-high pressures were used.

These specific features of synthesis may be of interest. Pressing is technologically simpler than ball milling, while temperature and pressure are significantly lower than in the mentioned articles (Kataoka et al. 2007; Martinez-Coronado et al. 2013; Takamura et al. 2002). Besides, we suggest that the process reported in the present work is applicable for a various set of metals and MgH_2. This opens a prospect of applying a simple approach to obtaining new intermetallic hydrides when conventional methods of synthesis are not efficient. Novel hydrogen-rich materials could be of particular interest for solid-state hydrogen storage and other applications in hydrogen energy.

Conclusions

We found that the exposure of a pressed mixture of MgH_2 and Ni in hydrogen at the pressure over 60 bar and the temperature of 450 °C results in the direct synthesis of Mg_2NiH_4. The presence of hydrogen prevents decomposition of the magnesium hydride and Mg_2NiH_4. Using the XRD, SEM, EDX and TDS techniques, we investigated this unconventional way of obtaining intermetallic hydride Mg_2NiH_4 in one step. This solid-state direct synthesis reaction of $2MgH_2 + Ni \xrightarrow{H_2} Mg_2NiH_4$ proceeds at low temperatures, starting at 425 °C.

The conditions of the reaction are:

- hydrogen pressure must be higher than the equilibrium pressure with MgH_2 and Mg_2NiH_4 in order to prevent decomposition of the hydrides. The invariability of the pressure evidences that the reaction proceeds without initial decomposition of magnesium hydride;
- since solid phase mass transfer is responsible for the ternary hydride formation, the pressing of MgH_2 and Ni powders ensures a good interfacing between the reagents.

The similarities in synthesis kinetics of powder samples and the planar ones described in (Baraban et al. 2022) suggest that the reaction mechanisms are also similar. Firstly, during incubation the intermetallic compound $MgNi_2$ is formed. Then, at the Mg_2Ni-Mg_2NiH_4 interface the hydride Mg_2NiH_4 is synthesized, through which Mg and H atoms arrive from MgH_2 by the vacancy mechanism. The constant growth rate of the RF is limited by the constant diffusion rate of nickel atoms through the layer of intermetallic compound $MgNi_2$.

Further investigation of such reactions is of great importance for a better understanding of the formation of multicomponent hydrides. Besides, it gives a promise of developing an original approach to obtaining new hydrogen-rich materials for various applications in hydrogen storage.

Conflict of Interest

The authors declare that there is no conflict of interest, either existing or potential.

Author Contributions

All the authors discussed the final work and took an equal part in writing the article.

Acknowledgements

The authors would like to thank the staff of the two Resource Centers of Saint-Petersburg State University — Nanotechnology and X-ray Diffraction Studies.

References

Akiyama, T., Isogai, H., Yagi, J. (1997) Hydriding combustion synthesis for the production of hydrogen storage alloy. *Journal of Alloys and Compounds*, 252 (1–2), L1–L4. https://doi.org/10.1016/S0925-8388(96)02674-6 (In English)

Akiyama, T., Isogai, H., Yagi, J. (1998) Reaction rate of combustion synthesis of an intermetallic compound. *Powder Technology*, 95 (2), 175–181. https://doi.org/10.1016/S0032-5910(97)03345-7 (In English)

Baraban, A. P., Chernov, I. A., Dmitriev, V. A. et al. (2022) The Mg_2NiH_4 film on nickel substrate: Synthesis, properties and kinetics of formation. *Thin Solid Films*, 762, article 139556. https://doi.org/10.1016/j.tsf.2022.139556 (In English)

Blomqvist, H., Noréus, D. (2002) Mechanically reversible conductor–insulator transition in Mg_2NiH_4. *Journal of Applied Physics*, 91 (8), 5141–5148. https://doi.org/10.1063/1.1461069 (In English)

Blomqvist, H., Rönnebro, E., Noréus, D., Kuji, T. (2002) Competing stabilisation mechanisms in Mg_2NiH_4. *Journal of Alloys and Compounds*, 330–332, 268–270. https://doi.org/10.1016/S0925-8388(01)01637-1 (In English)

Elets, D., Chernov, I., Voyt, A. et al. (2017) Influence of uniaxial pressing and nickel catalytic additive on activation of magnesium hydride thermal decomposition. *International Journal of Hydrogen Energy*, 42 (39), 24877–24884. https://doi.org/10.1016/j.ijhydene.2017.08.076 (In English)

Evard, E., Gabis, I., Yartys, V. (2010) Kinetics of hydrogen evolution from MgH_2: Experimental studies, mechanism and modeling. *International Journal of Hydrogen Energy*, 35 (17), 9060–9069. https://doi.org/10.1016/j.ijhydene.2010.05.092 (In English)

Humphries, T. D., Sheppard, D. A., Buckley, C. E. (2017) Recent advances in the 18-electron complex transition metal hydrides of Ni, Fe, Co and Ru. *Coordination Chemistry Reviews*, 342, 19–33. https://doi.org/10.1016/j.ccr.2017.04.001 (In English)

Kataoka, R., Goto, Y., Kamegawa, A. et al. (2007) High-pressure synthesis of novel hydride in Mg–Ni–H and Mg–Ni–Cu–H systems. *Journal of Alloys and Compounds*, 446–447, 142–146. https://doi.org/10.1016/j.jallcom.2007.04.221 (In English)

Leng, H., Pan, Y., Li, Q., Chou, K-C. (2014) Effect of LiH on hydrogen storage property of MgH_2. *International Journal of Hydrogen Energy*, 39 (25), 13622–13627. https://doi.org/10.1016/j.ijhydene.2014.02.131 (In English)

Li, L., Akiyama, T., Yagi, J. (1999) Reaction mechanism of hydriding combustion synthesis of Mg_2NiH_4. *Intermetallics*, 7 (6), 671–677. https://doi.org/10.1016/S0966-9795(98)00082-X (In English)

Li, L., Akiyama, T., Yagi, J. (2001) Activation behaviors of Mg_2NiH_4 at different hydrogen pressures in hydriding combustion synthesis. *International Journal of Hydrogen Energy*, 26 (10), 1035–1040. https://doi.org/10.1016/S0360-3199(01)00042-8 (In English)

Li, L., Saita, I, Akiyama, T. (2004) Intermediate products during the hydriding combustion synthesis of Mg_2NiH_4. *Journal of Alloys and Compounds*, 384 (1-2), 157–164. https://doi.org/10.1016/j.jallcom.2004.04.092 (In English)

Li, L., Saita, I, Akiyama, T. (2005) Intermediate products of hydriding combustion synthesis of Mg_2NiH_4 studied by optical microscopy and field-emission scanning electron microscopy. *Intermetallics*, 13 (6), 662–668. https://doi.org/10.1016/j.intermet.2004.10.006 (In English)

Martinez-Coronado, R., Retuerto, M., Alonso, J. A. (2012) Simplified mechano-synthesis procedure of Mg_2NiH_4. *International Journal of Hydrogen Energy*, 37 (5), 4188–4193. https://doi.org/10.1016/j.ijhydene.2011.11.129 (In English)

Martınez-Coronado, R., Retuerto, M., Torres, B. et al. (2013) High-pressure synthesis, crystal structure and cyclability of the Mg_2NiH_4 hydride. *International Journal of Hydrogen Energy*, 38 (14), 5738–5745. https://doi.org/10.1016/j.ijhydene.2013.02.108 (In English)

Mulas, G., Delogu, F., Pistidda, C., Cocco, G. (2008) Mechanochemical effects on hydrogen absorption in Mg_2Ni alloys under mechanical processing conditions. *Journal of Materials Science*, 43 (15), 5193–5198. https://doi.org/10.1007/s10853-008-2719-6 (In English)

Orimo, S., Fujii, H., Ikeda, K. (1997) Notable hydriding properties of a nanostructured composite material of the Mg_2Ni-H system synthesized by reactive mechanical grinding. *Acta Materialia*, 45 (1), 331–341. https://doi.org/10.1016/S1359-6454(96)00158-9 (In English)

Polanski, M., Nielsen, T., Kunce, I. et al. (2013) Mg_2NiH_4 synthesis and decomposition reactions. *International Journal of Hydrogen Energy*, 38 (10), 4003–4010. https://doi.org/10.1016/j.ijhydene.2013.01.119 (In English)

Reilly, J. J., Wiswall, R. H. (1968) Reaction hydrogen with alloys of magnesium and nickel and the formation of Mg_2NiH_4. *Inorganic Chemistry*, 7 (11), 2254–2256. https://doi.org/10.1021/ic50069a016 (In English)

Revesz, A., Gajdics, M., Schafler, E et al. (2017) Dehydrogenation-hydrogenation characteristics of nanocrystalline Mg_2Ni powders compacted by high-pressure torsion. *Journal of Alloys and Compounds*, 702, 84–91. https://doi.org/10.1016/j.jallcom.2017.01.261 (In English)

Saita, I., Li, L., Saito, K., Akiyama, T. (2003) Hydriding combustion synthesis of Mg_2NiH_4. *Journal of Alloys and Compounds*, 356–357, 490–493. https://doi.org/10.1016/S0925-8388(03)00230-5 (In English)

Takamura, H., Kakuta, H., Kamegawa, A., Okada, M. (2002) Crystal structure of novel hydrides in a Mg–Ni–H system prepared under an ultra high pressure. *Journal of Alloys and Compounds*, 330–332, 157–161. https://doi.org/10.1016/S0925-8388(01)01577-8 (In English)

Physics of Complex Systems, 2023, vol. 4, no. 3
www.physcomsys.ru

Theoretical physics.
Physics of atoms and molecules

UDC 530.182

EDN OUAIPE
https://www.doi.org/10.33910/2687-153X-2023-4-3-103-111

Interaction of subsystems in nonlinear dynamics problems. Various phases of chaos

A. V. Liaptsev✉[1]

[1] Herzen State Pedagogical University of Russia, 48 Moika Emb., Saint Petersburg 191186, Russia

Author
Alexander V. Liaptsev, ORCID: 0000-0002-8702-9062, e-mail: lav@herzen.spb.ru

For citation: Liaptsev, A. V. (2023) Interaction of subsystems in nonlinear dynamics problems. Various phases of chaos. *Physics of Complex Systems*, 4 (3), 103–111. https://www.doi.org/10.33910/2687-153X-2023-4-3-103-111 EDN OUAIPE

Received 6 June 2023; reviewed 22 June 2023; accepted 22 June 2023.

Funding: The study did not receive any external funding.

Abstract. A model of two interacting dissipative subsystems described by equations of nonlinear dynamics is considered. Each of the subsystems is a nonlinear oscillator driven by an external periodic field. The numerical calculation shows that chaotic oscillations can occur in this system. Their phase trajectories are described by a chaotic attractor in the limit of large times. It is shown that due to the symmetry of the system, different initial conditions can lead to different chaotic attractors. An analogy is discussed between various strange attractors of this model and different phases of matter in systems with a large number of particles.

Keywords: nonlinear dynamics, strange attractor, chaotic attractor, probability density, chaos, thermodynamic phase

Introduction

One of the characteristic features of systems described by nonlinear dynamics equations is the appearance of chaotic motion. In particular, in dissipative systems, the trajectory of a system in phase space may tend to a set of points called a chaotic (strange) attractor (Grinchenko et al. 2017; Malinetsky, Potapov 2000; Sagdeev et al. 1988; Schuster 1984). Chaos in such systems is interspersed with regular (periodic) movement when some parameters change. The corresponding parameters are called control parameters.

Note that the appearance of chaotic states is caused exactly by the nonlinearity of systems of differential equations and manifests itself in physical systems that are not described by the equations of classical dynamics. Currently, the methods of modern micro- and nanotechnology have made it possible to create objects with unusual electromagnetic properties, the so-called metamaterials (Soukoulis, Wegener 2010; Zheludev 2010). Among them of special interest are: 2D supercrystals of semiconductor quantum dots (Evers et al. 2013) and super crystals synthesized on the basis of aromatic 2D polymers (Liu et al. 2017). To date, the optical properties of these objects, especially nonlinear ones, including chaotic dynamics, are a promising and little-studied avenue of research (Ryzhov et al. 2017; 2021). In these nonlinear dynamical systems, under conditions of a degenerate doublet state, the problem can be reduced (if there are appropriate conservation laws) to the Duffing equation. Nonlinear optical dynamics based on quasi-resonator superradiance of a two-layer system with active walls (doped Λ-emitters) can be reduced to a system of two coupled Duffing oscillators considered in this article.

Chaotic motion in such systems has some features in many ways similar to the features in systems with a large number of particles. In particular, similarly to systems with a large number of particles, the states of chaotic systems in question can be described in terms of probability by defining the concept of probability density. As is in systems with a large number of particles, the probability density determines the probability of finding the system in a given region of phase space (Kuznetsov 2006; Liapzev 2019). For systems with some nontrivial symmetry, the probability density is transformed in accordance with a fully symmetric representation of the corresponding symmetry group (Liaptsev 2013; 2014).

Continuing the analogy between the chaotic state of a dissipative system described by a nonlinear dynamic equation and a system with a large number of particles, it can be noted that a strange attractor is analogous to the equilibrium state of a system with a large number of particles. This means that, regardless of the initial state, over time, systems tend to some equilibrium state described by some probability density function. It is the independence from the initial state that makes it possible to determine the chaotic attractor in problems of nonlinear dynamics. However, referring to systems with a large number of particles, one can find examples when, under the same external conditions, the existence of several equilibrium states with different properties is possible. In such cases, the states correspond to different phases.

A typical example is the states arising during the transition from the gas phase to the liquid phase, described by isotherms of a real gas (Fig. 1).

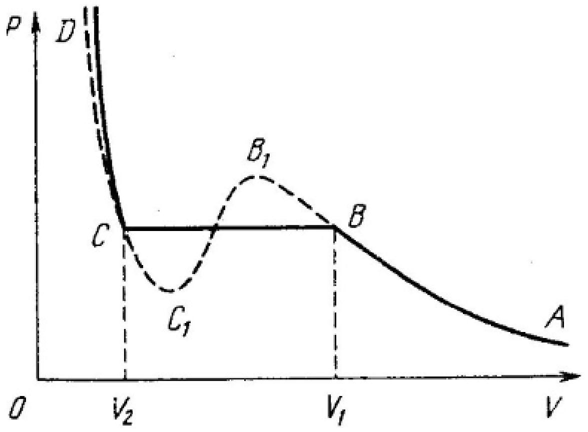

Fig.1. Isotherms of a real gas

In the interval of the isotherm described by the straight *BC*, the state is characterized by the equilibrium of two phases — liquid and gas. However, along with this stable state, states with a single phase are possible in intervals CC_1 and BB_1. This is the so-called "supercooled vapor" in the BB_1 interval and "superheated liquid" in the CC_1 interval. These states are less stable than the states on the *BC* line, and can only be obtained with an adiabatic change in the system parameters from some other states (Kondepudi, Prigogine 2015). In this paper, we consider a model of a dissipative system described by equations of nonlinear dynamics, the state of which may tend to various chaotic attractors depending on the initial states of the system. This is equivalent to the existence of states with different phases under the same conditions in systems with a large number of particles.

Formulation of the model

One of the systems in which chaos is observed is a model of a nonlinear oscillator driven by external periodic force. Such systems are described by the Duffing equation:

$$\ddot{x}(t) + \gamma \dot{x}(t) - \alpha x(t) + \beta x^3(t) = F \sin(\omega t) . \tag{1}$$

In this equation, the variable x describes the oscillations, the points above the variable are the standard notation of time derivatives, the parameters α and β determine the shape of the oscillator potential. In particular, at $\alpha > 0$ and $\beta > 0$, the so-called *W*-potential appears. The parameter γ characterizes the value of dissipation, and the parameters F and ω the amplitude and frequency of external action. A real system corresponding to this model can be a load that is located in the upper part of an elastic rod and swings in one plane to an external force (Fig. 2).

Fig. 2. A real system corresponding to the Duffing equation

Next, we will consider a model of two spring-coupled nonlinear oscillators (Fig. 3).

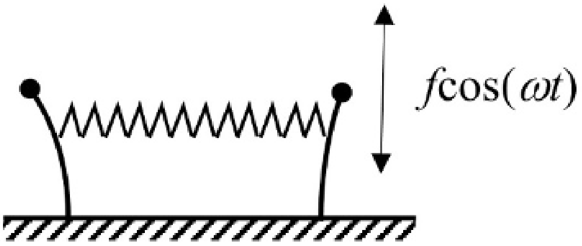

Fig. 3. A model of two oscillators connected by a spring

The stiffness of the spring k characterizes the magnitude of the interaction of subsystems. At $k \to 0$, the interaction of subsystems disappears. We will also assume that an external force acts vertically. In the case of a pendulum, the moment of such force is proportional to $\sin(x)$, where x is the angle of deviation from the vertical. To take into account the bending of the rod, we will model the moment of external force proportional to $\sin(px)$, where p is some constant. As a result, the system of dynamic equations for the formulated model takes the form:

$$\begin{aligned}\ddot{x}_1 &= f\sin(px_1)\sin(\omega t) - \gamma\dot{x}_1 + \alpha x_1 - \beta x_1{}^3 - k(x_1 - x_2),\\ \ddot{x}_2 &= f\sin(px_2)\sin(\omega t) - \gamma\dot{x}_2 + \alpha x_2 - \beta x_2{}^3 - k(x_2 - x_1).\end{aligned}$$

This system of equations can be written as an autonomous system of 1st order differential equations:

$$\begin{aligned}&\dot{x}_1 = v_1,\\ &\dot{x}_2 = v_2,\\ &\dot{v}_1 = f\sin(px_1)\sin\varphi + \alpha x_1 - \beta x_1^3 - \gamma v_1 - k(x_1 - x_2),\\ &\dot{v}_2 = f\sin(px_2)\sin\varphi + \alpha x_2 - \beta x_2^3 - \gamma v_2 - k(x_2 - x_1),\\ &\dot{\varphi} = \omega.\end{aligned} \tag{2}$$

The variables v_1 and v_2 are the velocities corresponding to the coordinates x_1 and x_2. The numerical calculation shows that this system of nonlinear differential equations has chaotic solutions for some parameter values. The set of points in the 5-dimensional phase space, to which the trajectory of this solution tends at large times, represents a chaotic attractor. In accordance with what was said above, the state in phase space can be characterized by a probability density $\rho(x_1, x_2, v_1, v_2, \varphi)$ determined in such a way that the probability of finding a system in a small volume of phase space $\Delta x_1 \Delta x_2 \Delta v_1 \Delta v_2 \Delta\varphi$ is equal to:

$$\Delta w = \rho(x_1, x_2, v_1, v_2, \varphi)\Delta x_1 \Delta x_2 \Delta v_1 \Delta v_2 \Delta\varphi . \tag{3}$$

The probability density satisfies a partial differential equation of the 1st order (Liapzev 2019) (see also (Kuznetsov 2006)), which takes the following form for the system of equations (2):

$$\begin{aligned}&\omega\frac{\partial\rho}{\partial\varphi} + v_1\frac{\partial\rho}{\partial x_1} + v_2\frac{\partial\rho}{\partial x_2} + \\ &\left(f\sin\varphi\sin(px_1) + \alpha x_1 - \beta x_1^3 - \gamma v_1 - k(x_1 - x_2)\right)\frac{\partial\rho}{\partial v_1} + \\ &\left(f\sin\varphi\sin(px_2) + \alpha x_2 - \beta x_2^3 - \gamma v_2 - k(x_2 - x_1)\right)\frac{\partial\rho}{\partial v_2} = 0\end{aligned} . \tag{4}$$

Analysis of particular solutions

Note, first of all, that the system of equations (2) has a trivial solution $x_1 = x_2 = v_1 = v_2 = 0,\ \varphi = \omega t$, which is realized under initial conditions $x_1(0) = x_2(0) = v_1(0) = v_2(0) = \varphi(0) = 0$. In the special case k=0, depending on the initial conditions, one of the subsystems may have an identically zero solution, and the second may have some non-zero solution, including a chaotic solution. These solutions, the initial conditions under which they are implemented, as well as the form of the solution for the probability density of the state in the case when one of the solutions is chaotic, are given in Table 1. In all cases $\varphi(t) = \omega t$.

Table 1. Probability density depending on initial conditions

№	Solutions	Initial conditions	Probability density of the state $\rho(x_1, x_2, v_1, v_2, \varphi)$
1	$x_2(t) = v_2(t) = 0,$ $x_1(t) \neq 0, \quad v_1(t) \neq 0$	$x_2(0) = v_2(0) = 0$	$\rho(x_1, v_1, \varphi)\delta(x_2)\delta(v_2)$
2	$x_1(t) = v_1(t) = 0,$ $x_2(t) \neq 0, \quad v_2(t) \neq 0$	$x_1(0) = v_1(0) = 0$	$\rho(x_2, v_2, \varphi)\delta(x_1)\delta(v_1)$
3	$x_1(t) = x_2(t),$ $v_1(t) = v_2(t)$	$x_1(0) = x_2(0),$ $v_1(0) = v_2(0)$	$\rho(x_1, v_1, \varphi)\delta(x_1 - x_2)\delta(v_1 - v_2)$
4	$x_1(t) = -x_2(t),$ $v_1(t) = -v_2(t)$	$x_1(0) = -x_2(0),$ $v_1(0) = -v_2(0)$	$\rho(x_1, v_1, \varphi)\delta(x_1 + x_2)\delta(v_1 + v_2)$

The right column of the table shows the standard designation for δ-function. The numerical calculation under the initial conditions given in the table confirms the existence of chaotic solutions satisfying the relations given in the table.

Symmetry properties of equations and solutions

A simple analysis allows us to determine the symmetry properties of the system of equations (2). Namely, the system of equations remains invariant with simultaneous replacement of indices and inversion of variables x_i and v_i. For linear systems of equations, certain relations for solutions of this system follow from such symmetry. In this case, the symmetry properties also allow us to obtain some properties of solutions. To obtain these properties, we introduce symmetric x_s and antisymmetric x_a coordinates and corresponding velocities:

$$x_s = \frac{x_1 - x_2}{2}, \quad x_a = \frac{x_1 + x_2}{2}, \quad v_s = \frac{v_1 - v_2}{2}, \quad v_a = \frac{v_1 + v_2}{2}. \tag{5}$$

The above symmetry transformations leave symmetric variables invariant and change the sign of antisymmetric variables.

The system of equations (2) for the new variables takes the form:

$$\begin{aligned}
&\dot{x}_a = v_a, \\
&\dot{x}_s = v_s, \\
&\dot{v}_a = f\sin(px_a)\cos(px_s)\sin\varphi + \alpha x_a - \beta x_a^3 - \gamma v_a, \\
&\dot{v}_s = f\sin(px_s)\cos(px_2)\sin\varphi + \alpha x_s - \beta x_s^3 - \gamma v_s - 2kx_s, \\
&\dot{\varphi} = \omega.
\end{aligned} \tag{6}$$

Obviously, in the special case k=0, solutions 3 and 4 given in Table 1 correspond to zero symmetric and antisymmetric solutions. However, from the analysis of the system of equations (6), more general conclusions that are valid for all values of parameter k can be deduced. Namely, under initial conditions $x_s(0) = v_s(0) = 0$, solutions are possible in which only antisymmetric variables are different from zero $x_a \neq 0$, $v_a \neq 0$. The obtained solutions, among which there can be both regular and chaotic solutions, do not depend on the parameter k. On the contrary, under initial conditions $x_a(0) = v_a(0) = 0$, solutions are possible in which only symmetric variables are different from zero $x_s \neq 0, v_s \neq 0$. Note that the above symmetry transformation and the identity transformation form a symmetry group isomorphic to the point symmetry group C_2. The probability density $\rho(x_1, x_2, v_1, v_2, \varphi)$ for any of the above solutions is transformed by the fully symmetric representation of this group. This means that equality $\rho(-x_2, -x_1, -v_2, -v_1, \varphi) = \rho(x_1, x_2, v_1, v_2, \varphi)$ or equality $\rho(-x_a, x_s, -v_a, v_s, \varphi) = \rho(x_a, x_s, v_a, v_s, \varphi)$ for the variables x_a, x_s, v_a, v_s is fulfilled.

Analysis of numerical solutions

Numerical calculations were carried out as follows. At the first step, the system of differential equations was numerically solved under given initial conditions over a time interval from 0 to $10T$, where T is the period of the driving force. At each of the periods, the values of the variables were calculated in increments of $T/360$. The final state was the initial state for the next interval of 10 periods of the driving force. Then the actions were repeated N times. The number N could be varied. The calculations below correspond to the values of N = 1000, that is, the full-time interval corresponded to 10,000 periods of the driving force.

Under arbitrary initial conditions, both symmetric and antisymmetric oscillations were excited. The calculations were carried out starting from the parameter k = 0 followed by a further increase of this parameter and preservation of the remaining parameters. The calculations have shown that with an increase in the value of k, the amplitude of symmetric oscillations decreased on average, and the amplitude of antisymmetric oscillations increased. To quantify this effect, the average volumes of phase space occupied by symmetric and antisymmetric oscillations were calculated. These volumes were defined by calculating the following averages:

$$V_s = \left\langle x_{si}^2 + v_{si}^2 \right\rangle, \quad V_a = \left\langle x_{ai}^2 + v_{ai}^2 \right\rangle, \tag{7}$$

where the index i numbers the values of variables in the arrays obtained during the calculations.

Fig. 4 shows graphs of the dependence of Vs and Va values under arbitrary initial conditions, denoted as Vs_{rand} and Va_{rand}. When constructing the graphs, the results obtained with the values of the variable k for regular (periodic in time) solutions were not taken into account.

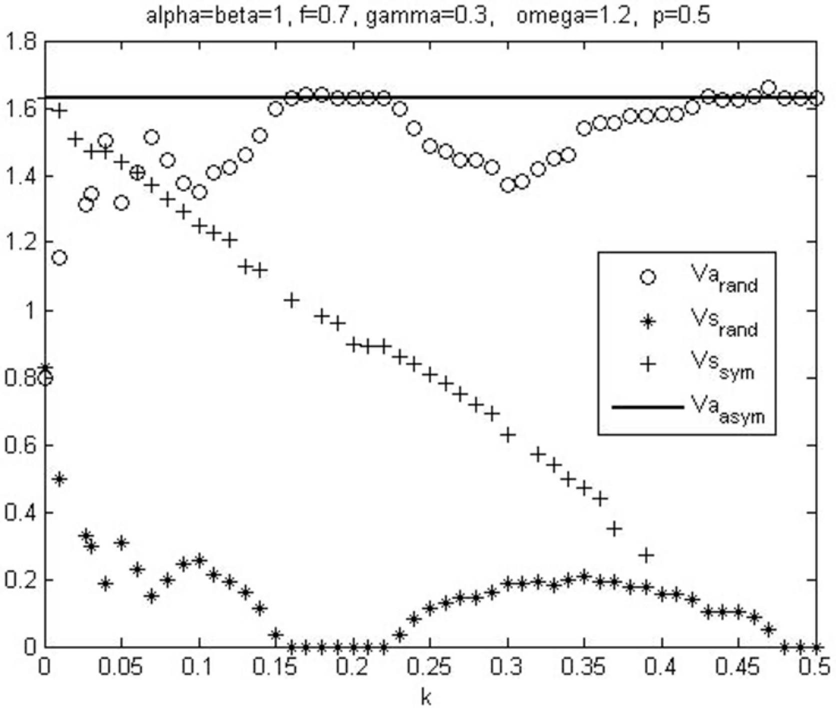

Fig. 4. Results of the numerical calculation

As can be seen from the graphs, the values of $Va_{rand}(0)$ and $Vs_{rand}(0)$ (no interaction of subsystems) are approximately the same. As the value of k increases (the spring stiffness increases), the values of $Va_{rand}(k)$ increase, and the values of $Vs_{rand}(k)$ decrease, although the corresponding dependencies are not monotonic. At the same time, the sum of $Va_{rand}(k) + Vs_{rand}(k)$ remains approximately constant. At values $k \geq 0.8$, the oscillations become completely antisymmetric: $Vs_{rand}(k) = 0$. This corresponds to the fact that the subsystems are rigidly connected and move as a whole. The solutions $Va_{rand}(k)$ and $Vs_{rand}(k)$ are stable, that is, under different initial conditions, the obtained values coincide. It should also be noted that there is a range of values $k \in [0.16, 0.22]$ for which $Vs_{rand}(k)$ turns to zero, that is, the oscillations become asymmetric.

A qualitatively different nature of solutions is obtained if the initial states correspond to a symmetric ($x_a(0) = v_a(0) = 0$) or an antisymmetric ($x_s(0) = v_s(0) = 0$) state. For the antisymmetric initial state, the numerical solutions obtained do not depend on the values of the parameter k, which corresponds to the above qualitative analysis. This means that $Va(k) = const$, $Vs(k) = 0$. The corresponding graph $Va(k)$ is shown in Fig. 4 as a straight line (Va_{asym}). For the symmetric initial state, the numerical calculation gives the result $Va(k) = 0$ and monotonically decreasing $Vs(k)$ dependencies, shown in Fig. 4 in the notation Vs_{sym}. In the range of values $k \in [0.39, 0.48]$, the solutions of the system of differential equations become regular with the amplitude decreasing with an increase in the value of k. For even larger values of k, the solutions become chaotic with a small amplitude, so that $Vs(k) \approx 0$.

Unlike the solutions obtained under arbitrary initial conditions, symmetric (Vs_{sym}) and antisymmetric (Va_{asym}) solutions are unstable. This instability can be detected as follows. As mentioned above, the calculation was carried out in such a way that the final state obtained by solving a system of equations at a certain time interval is the initial state at the next time interval. If the final state is changed to the value of machine precision and taken as the initial state at the next stage, then with further calculation, the state of the system loses its initial symmetry. That is, if at some value of *k* the system was in a state where only a symmetric oscillation was excited (the Vs_{sym} branch in Fig. 4), or only an antisymmetric oscillation (Va_{asym} branch in Fig. 4), then the system jumps into a state in which $Va \neq 0$, $Vs \neq 0$ (Va_{rand} and Vs_{rand} branches in Fig. 4). Such a transition is equivalent to the transition between the states of a real gas, when instead of an overheated liquid or supercooled gas, a state in the form of a mixture of liquid and gas phases occurs.

In systems described by equations of nonlinear dynamics, another important property, similar to what occurs in systems with a large number of particles, is manifested. Namely, with an adiabatic change of parameters, some properties of the system are described by various dependencies with decreasing and increasing parameters. In systems with a large number of particles, the corresponding property is called “hysteresis”. The simplest examples of the manifestation of hysteresis in nonlinear dynamics problems can be used in the educational process (task 2.9 from the textbook (Kondratyev, Liaptsev 2008)). In the model considered here, the phenomenon of hysteresis manifests itself with an adiabatic change in the parameter *k*. The adiabatic change of the parameter means that when the calculation is completed with some parameter *k*, the resulting final state is used as the initial state for the calculation with the parameter $k + \Delta k$. An example of hysteresis in the system considered in our work are the calculations whose results are shown in Fig. 4. In particular, if we start the calculation with the value $k = 0.1$ under unsymmetric initial conditions, when both symmetric and antisymmetric oscillations ($V_a \neq 0, V_s \neq 0$) are excited, and then adiabatically increase the parameter *k*, as described above, we can come to a region $k \in [0.16,\ 0.22]$, where only the antisymmetric oscillation is different from zero, that is, $Vs = 0$. If the parameter *k* is then reduced adiabatically, the state of the system will change so that, as before, the symmetric oscillation turns out to be unexcited. The diagram illustrating the above explanation is shown in Fig. 5.

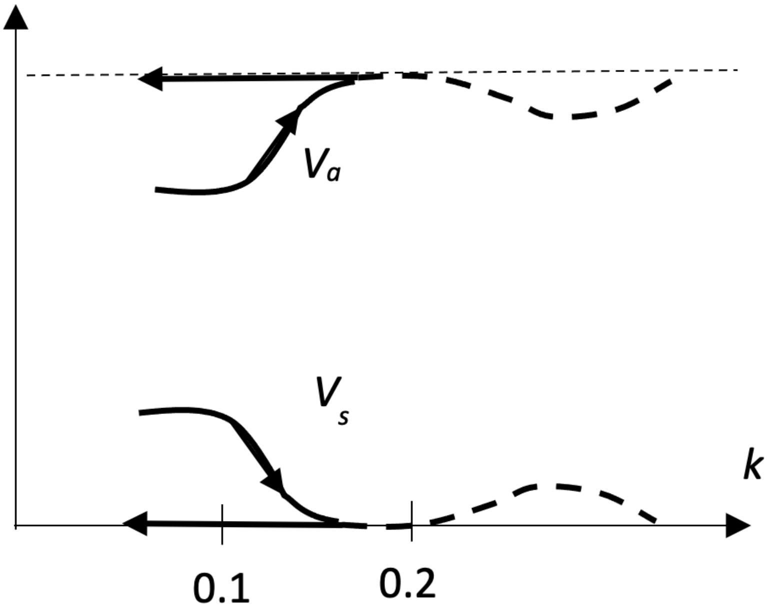

Fig. 5. A diagram illustrating the manifestation of hysteresis with an adiabatic change in the parameter *k*

Similar manifestations of hysteresis are processes on the isotherm of a real gas (Fig. 1). If, at the initial state (a mixture of gas and liquid on a rectilinear section of the *CB* isotherm), the volume is increased, then at point *B* the system is in a homogeneous gas state. If you then slowly reduce the volume, you can get superheated steam, that is, start moving along the section of the BB_1 isotherm.

Conclusions

Returning to the discussion of the analogy of the chaotic solutions obtained with the state of a real gas, the following analogies can be stated.

1) For an arbitrary initial state of the system under consideration, the solution corresponding to chaotic oscillations is a mixture of symmetric and antisymmetric oscillations. This is analogous to the fact that the state of the real gas in the *BC* isotherm region (Fig. 1) is a mixture of liquid and gaseous phases.
2) When the parameter k is changed, the contribution of symmetric and antisymmetric oscillations changes up to the moment when the contribution of symmetric oscillations becomes zero. This is analogous to the fact that when the volume of a real gas changes, the proportion of liquid and gas changes, too, and only one of the phases remains at points B or C (Fig. 1).
3) The "coexistence" of phases, that is, the state in which $Va \neq 0,\ Vs \neq 0$, is stable, similarly to the stable state of the real gas at the *BC* region.
4) In addition to the stable state as a "mixture of phases" ($Va \neq 0,\ Vs \neq 0$), there are unstable states formed under specific initial conditions (symmetric or antisymmetric initial state). An analog for the isotherm of a real gas is the presence of states with overheated liquid or supercooled gas.

These analogies indicate the possibility of the existence of various phases of a chaotic state in systems described by equations of nonlinear dynamics.

Conflict of Interest

The author declares that there is no conflict of interest, either existing or potential.

References

Grinchenko, V. T., Matsipura, V. T., Snarskij, A. A. (2007) *Vvedenie v nelinejnuyu dinamiku. Khaos i fraktaly [Introduction to Nonlinear dynamics. Chaos and fractals]*. 2nd ed. Moscow: URSS Publ., 283 p. (In Russian)

Evers, W. H., Goris, B., Bals, S. et al. (2013) Low-dimensional semiconductor superlattices formed by geometric control over nanocrystal attachment. *Nano Letters*, 13 (6), 2317–2323. https://doi.org/10.1021/nl303322k (In English)

Kondepudi, D. K., Prigogine, I. (2015) *Modern thermodynamics: From heat engines to dissipative structures*. Chichester: John Wiley & Sons Publ., 341 p. (In English)

Kondratiev, A. S., Liaptsev, A. V. (2008) *Fizika. Zadachi na komp'yutere [Physics. Tasks on the computer]*. Moscow: Physmatlit Publ., 400 p. (In Russian)

Kuznetsov, S. P. (2006) *Dinamicheskij khaos: Kurs lektsij [Dynamic chaos: A course of lectures]*. 2nd ed., comp. Moscow: Physmatlit Publ., 356 p. (In Russian)

Liaptsev, A. V. (2013) Simmetriya regulyarnykh i khaoticheskikh dvizhenij v zadachakh nelinejnoj dinamiki. Uravnenie Duffinga [The symmetry of regular and chaotic motions in nonlinear dynamic problems. Duffing equation]. *Izvestia Rossijskogo gosudarstvennogo pedagogicheskogo universiteta im. A. I. Gertsena — Izvestia: Herzen University Journal of Humanities & Sciences*, 157, 24–34. (In Russian)

Liaptsev, A. V. (2014) Simmetriya regulyarnykh i khaoticheskikh dvizhenij v zadachakh nelinejnoj dinamiki. Rotator v periodicheskom pole [Symmetry of regular and chaotic motions in nonlinear dynamic problems. Rotator in periodic field *Izvestia Rossijskogo gosudarstvennogo pedagogicheskogo universiteta im. A. I. Gertsena — Izvestia: Herzen University Journal of Humanities & Sciences*, 165, 23–34. (In Russian)

Liapzev, A. V. (2019) The calculation of the probability density in phase space of a chaotic system on the example of rotator in the harmonic field. *Computer Assisted Mathematics*, 1, 55–65. (In English)

Liu, W., Luo, X., Bao, Y. et al. (2017) A two-dimensional conjugated aromatic polymer via C–C coupling reaction. *Nature Chemistry*, 9 (6), 563–570. https://doi.org/10.1038/nchem.2696 (In English)

Malinetsky, G. G., Potapov, A. B. (2000) *Sovremennye problemy nelinejnoj dinamiki [Modern problems of nonlinear dynamics]*. Moscow: Editorial URSS Publ., 336 p. (In Russian)

Ryzhov, I. V., Vasil'ev, N. A., Kisiva, I. S. et al. (2017) Cooperative emission from an ensemble of three-level Λ radiators in a cavity: An insight from the viewpoint of dynamics of nonlinear systems. *Journal of Experimental and Theoretical Physics*, 124 (5), 683–700. https://doi.org/10.1134/S1063776117050053 (In English)

Ryzhov, I. V., Malikov, R. F., Malyshev, A. V., Malyshev, V. A. (2021) Quantum metasurfaces of arrays of Λ-emitters for photonic nano-devices. *Journal of Optics*, 23 (11), article 11510. https://doi.org/10.1088/2040-8986/ac2788 (In English)

Sagdeev, *R.* Z., Usikov, *D.* A., Zaslavsky, *G.* M. (1988) *Nonlinear Physics: From the pendulum to turbulence and chaos*. New York: Harwood Academic Publ., 675 p. (In English)

Schuster, G. H. (1984) Deterministic chaos. An introduction. Weinheim: Physik-Verlag, 304 p. (In English)

Soukoulis, C. M., Wegener, W. (2010) Optical metamaterials—more bulky and less lossy. *Science*, 330 (6011), 1633–1634. (In English)

Zheludev, N. I. (2010) The road ahead for metamaterials. *Science*, 328 (5978), 582–583. (In English)

Physics of Complex Systems, 2023, vol. 4, no. 3
www.physcomsys.ru

Theoretical physics.
Physics of atoms and molecules

UDC 533,51-73

EDN PXERKT
https://www.doi.org/10.33910/2687-153X-2023-4-3-112-123

Numerical simulation of the dynamics of an electrically charged multifractional aerosol moving in a channel under the action of the Coulomb force and aerodynamic forces

D. A. Tukmakov✉[1]

[1] IME Federal Research Center "Kazan Scientific Center of the Russian Academy of Sciences",
2 Lobachevskogo Str., Kazan 420111, Russia

Author
Dmetree A. Tukmakov, ORCID: 0000-0002-0335-8548, e-mail: tukmakovda@imm.knc.ru

For citation: Tukmakov, D. A. (2023) Numerical simulation of the dynamics of an electrically charged multifractional aerosol moving in a channel under the action of the Coulomb force and aerodynamic forces. *Physics of Complex Systems*, 4 (3), 112–123. https://www.doi.org/10.33910/2687-153X-2023-4-3-112-123 EDN PXERKT

Received 18 April 2023; reviewed 13 June 2023; accepted 13 June 2023.

Funding: The work was carried out as part of the state-commissioned assignment of the Federal Research Center of the Kazan Scientific Center of the Russian Academy of Sciences.

Abstract. This work focuses on mathematical modeling of the dynamics of an electrically charged aerosol in a channel. In particular, the study models the operation of an electric filter for dispersed media. To optimize technologies for electrical filtration of dispersed media, it is necessary to understand the regularities of the dynamics of charged dispersed particles in an electric field. The mathematical model is implemented as a computer program. The program code is a finite-difference numerical algorithm for solving the equations of a mathematical model. The simulated medium consists of two components: the first component is a viscous compressible heat-conducting gas, the dynamics of which is described using the system of Navier-Stokes equations; the second component is electrically charged particles. The mathematical model took into account the intercomponent exchange of momentum and heat. The disperse component of the aerosol was described taking into account the multifractional composition. Each fraction has its own particle size, density and heat capacity of the material. It was assumed in the work that an electric potential was applied to the channel walls: a negative potential was applied to the lower wall, while a positive potential was applied to the upper wall of the channel. Calculations of the motion of a multi-fraction electrically charged gas suspension in a channel are carried out. Two cases were considered. Case 1: all fractions of the dispersed aerosol component have the same physical density of the material and different particle sizes. Case 2: the particles have the same size and differ in the density of the material. It was found that with the same density of the material, the vertical velocity of the particle and the intensity of the deposition process are greater with increasing particle size. It was also found that with the same particle size, particles with a higher density of the material are more intensively deposited. The revealed regularities can be used in optimizing the technologies of electrical filtration of dispersed media.

Keywords: numerical simulation, aerosols, polydisperse gas suspension, electrically charged media

Introduction

One of the types of irreversible processes that often occur in nature and technology is hydrodynamic processes. Hydrodynamic processes are the processes accompanied by the movement of continuous media — liquids, gases, plasma. The movement of inhomogeneous media is often found in nature and industrial applications (Altunin et al. 2012; Bastykova et al. 2021; Chekalov et al. 2021; Fedorov et al. 2015;

Ignatov 2020; Kolotinskii et al. 2021; Kutushev 2003; Nigmatullin 1978; Sinkevich 2016; Tada et al. 2016; Tukinakov 2019; Tukmakov 2022a; 2022b; 2023). A special case of inhomogeneous media is heterogeneous media, i. e., mixtures of the components which have different states of aggregation (Fedorov et al. 2015; Kutushev 2003; Nigmatullin 1978). In some cases, it becomes necessary to simulate the dynamics of electrically charged inhomogeneous media (Altunin et al. 2012; Bastykova et al. 2021; Chekalov et al. 2021; Ignatov 2020; Kolotinskii et al. 2021; Sinkevich 2016; Tada et al. 2016; Tukinakov 2019; Tukmakov 2022a; 2022b; 2023; Tukmakov, Tukmakov 2017).

The monograph (Nigmatullin 1978) outlines the theoretical foundations of the dynamics of multiphase media, presents various approaches to modeling the dynamics of inhomogeneous media, including the theory of continual mathematical models of the dynamics of multiphase media. Another monograph (Kutushev 2003) developed one-dimensional mathematical models of the dynamics of electrically neutral gas suspensions, while (Fedorov et al. 2015) developed various mathematical models of the dynamics of electrically neutral gas suspensions with solid particles. The article (Altunin et al. 2012) analyzes scientific and technical literature in order to describe the results of research and practical application of electric fields in liquid and gaseous media. In the study reported in (Bastykova et al. 2021), the evolution of dust grains from various materials used in thermonuclear power plants was studied, and a mathematical model was built to describe dust formation. The work (Chekalov et al. 2021) discusses technologies for electrostatic precipitators of gas suspensions in relation to the problems of industrial energy. The article (Ignatov 2020) is devoted to the development of mathematical models for the dynamics of dust particles moving in plasma above an electrode. The study (Kolotinskii et al. 2021) presents a mathematical model of the dynamics of negatively charged dust particles in plasma. The work (Sinkevich 2016) analyzes the stability of relatively small perturbations of the stationary state of a flat electrically charged interface between a two-phase thundercloud and a humid turbulent atmosphere, taking into account the viscosity of the medium. The article (Tada et al. 2016) investigates the influence of the electric field on heat transfer in a gas suspension with an electrically charged dispersed component.

Aerosols are often used in various applications—solid particles suspended in a gas or liquid droplets. It should be noted that real aerosols have a polydisperse composition, which means that fractions have different particle sizes and material densities. In industry, the problem often arises of cleaning a gas stream from solid or liquid particles. For this, electrostatic precipitators are used. In this case, dispersed flows are first charged with an electric charge in the electrode, which forms a corona discharge, and then deposited on a plate with a potential of the opposite sign. In this paper, we consider the flow of an electrically charged aerosol in a channel in which potentials of different signs are applied to the channel walls.

The mathematical model implements a continuum approach to the dynamics of inhomogeneous media, in which, for each of the mixture components, a complete hydrodynamic system of equations is solved with terms that take into account intercomponent momentum exchange and heat transfer. The continuum approach to the dynamics of inhomogeneous media most fully describes the dynamics of a mixture at close mass fractions of the mixture components (Nigmatullin 1978).

The scientific novelty lies in the fact that the continuum mathematical model is used to study the dynamics of an electrically charged aerosol, taking into account the multi-fraction composition of the dispersed component in a channel with electric potentials on the walls. The mathematical model takes into account the multi-fractional composition of the dispersed component of the aerosol. Since all aerosol fractions have a positive charge, dispersed particles settle on the electrode surface with a negative potential. The paper considers the influence of the properties of the dispersed phase fractions (material density and particle size) on the parameters of particle dynamics in the channel.

Mathematical model

The motion of the carrier medium is described by the system of Navier-Stokes equations (Fletcher 1988; Loitsyansky 2003; Muzafarov, Utyuzhnikov 1993; Tukmakov 2003) for a compressible heat-conducting gas taking into account the interphase force interaction and heat transfer (Tukinakov 2019; Tukmakov 2022a; 2022b; 2023; Tukmakov, Tukmakov 2017) (1)–(5):

$$\frac{\partial \rho_j}{\partial t} + \nabla\left(\rho_j \mathbf{V}_j\right) = 0 \tag{1}$$

$$\frac{\partial \rho_1 V_1^k}{\partial t} + \nabla^i\left(\rho_1 V_1^k V_1^i + \delta_{ik} p - \tau_{ik}\right) = -\sum_{j=2}^{m} F_{kj} + \sum_{j=2}^{m} \alpha_j \nabla^k p \tag{2}$$

$$\frac{\partial \rho_j V_j^k}{\partial t} + \nabla^i\left(\rho_j V_j^i V_j^k\right) = F_{kj} - \alpha_j \nabla^k p \tag{3}$$

$$\frac{\partial\left(e_1\right)}{\partial t} + \nabla^i\left(V_1^i\left(e_1 + p - \tau_{ii}\right) - V_1^k \tau_{ki} - \lambda \nabla^i T_1\right) = -\sum_{j=2}^{m} Q_j - \sum_{j=2}^{m} \left|F_{kj}\right|\left(V_1^k - V_j^k\right) +$$

$$+\sum_{j=2}^{m} \alpha_j \nabla^k\left(p V_1^k\right) \tag{4}$$

$$\frac{\partial\left(e_j\right)}{\partial t} + \nabla^k\left(e_j V_j^k\right) = Q_j \tag{5}$$

$$\frac{\partial^2 \varphi}{\partial {x_1}^2} + \frac{\partial^2 \varphi}{\partial {x_2}^2} = \sum_{j=2}^{m} \rho_j q_0 \tag{6}$$

$$\boldsymbol{V}_j = \left[u_j, v_j\right]; \rho_j = \alpha_j \rho_{j0}, k, i = 1,2; j = 1..m.$$

The electric field (6) was also taken into account in the mathematical model using the Poisson equation. The viscous stress tensor of the carrier medium is calculated as follows (7):

$$\tau_{11} = \text{ì}\left(2\frac{\partial u_1}{\partial x_1} - \frac{2}{3}D\right), \tau_{22} = \text{ì}\left(2\frac{\partial v_1}{\partial x_2} - \frac{2}{3}D\right), \tau_{12} = \tau_{21} = \mu\left(\frac{\partial u_1}{\partial x_2} + \frac{\partial v_1}{\partial x_1}\right) \tag{7}$$

$$D = \frac{\partial u_1}{\partial x_1} + \frac{\partial v_1}{\partial x_2}$$

The vector components of interphase exchange of momentum F_{1i} (8), F_{2i} (9) were described by the following equations:

$$F_{1i} = 0.75\frac{\pm_i}{d_i} C_{di}\, \text{Á}_1 \sqrt{\left(u_1 - u_i\right)^2 + \left(v_1 - v_i\right)^2}\left(u_1 - u_i\right) - \alpha_i q_0 \rho_i \,\partial\varphi/\partial x_1 \tag{8}$$

$$F_{2i} = 0.75\frac{\pm}{d_i} C_d\, \text{Á}_1 \sqrt{\left(u_1 - u_i\right)^2 + \left(v_1 - v_i\right)^2}\left(v_1 - v_i\right) - \alpha_i \rho_{i0} q_0 \,\partial\varphi/\partial x_2 \tag{9}$$

The vector components of the interphase exchange of momentum include the aerodynamic drag force (Fedorov et al. 2015; Kutushev 2003), as well as the Coulomb force (Salyanov 1997). Here, p, ρ_1, u_1, v_1 are the pressure, density, Cartesian components of the velocity of the carrier medium in the direction of the x_1 and x_2 axes, respectively; T_1, e_1 are the temperature and total energy of the gas; α_i,ρ_{i0} ρ_i, T_i, e_i, u_i, v_i are the volumetric content, physical density, average density, temperature, internal energy, Cartesian components of the dispersed phase fractions velocity; Q_i is the heat flux between carrier medium and i-th fraction of the dispersed phase; λ and μ are the thermal conductivity and viscosity of the carrier medium, respectively. The temperature of the carrier medium is found from the equation $T_1 = (\gamma - 1)\cdot(e_1/\rho_1 - 0.5\cdot(u_1^2+v_1^2))/R$, where R is the gas constant of the carrier medium, γ is the heat capacity ratio. The internal energy of the *i*-th fraction of the dispersed phase suspended in gas is defined as $e_i = \rho_i C_{pi} T_i$, where C_{pi} is the specific heat at the constant pressure of the *i*-th fraction of the dispersed phase. Heat transfer between the *i*-th fraction of the dispersed phase and gas: $Q_i = 6\alpha_i\, Nu_{1i}\lambda\, (T_1 - T_i)\, /d_i^2$, d_i is the particle diameter of the *i*-th fraction of the dispersed phase. The Nusselt number (10) is determined using the well-known approximation depending on the relative Mach (11), Reynolds (12), and Prandtl (13) numbers (Kutushev 2003):

$$Nu_{1i} = 2\,exp(-M_{1i}) + 0.459\,Re_{1i}^{0.55}\,Pr^{0.33}, \tag{10}$$

$$M_{1i} = \left|\bar{V}_1 - \bar{V}_i\right| / c, \tag{11}$$

$$Re_{1i} = \rho_1 \left|\bar{V}_1 - \bar{V}_i\right| d_i / \mu, \tag{12}$$

$$Pr = C_p \mu / \lambda \tag{13}$$

The mathematical model assumed the absence of interaction between particles.

The drag coefficient of spherical particles (14) was calculated using the following expression (Kutushev 2003):

$$C_{di} = \frac{24}{Re_{1i}} + \frac{4}{Re^{0.5}_{1i}} + 0.4 \tag{14}$$

where q_0 is the specific charge per unit mass of the solid fraction and ϕ is the electric field potential. *E* is the electric field strength, ε is the relative dielectric constant of air, ε_0 is the absolute dielectric constant of air. The system of equations for the dynamics of a multiphase medium (1)–(5) was solved by the McCormack explicit finite difference method (Fletcher 1988) of the second order of accuracy in time and space. The calculation error is the largest value of the squared steps in spatial directions and time steps–Δx, Δy, Δt: max $(\Delta x^2, \Delta y^2, \Delta t^2)$. The monotonicity of the solution was achieved using the correction scheme (Muzafarov, Utyuzhnikov et al. 1993; Tukmakov 2003) after the transition from the *n*-th to a new time layer $t = t^{n+1}$. When calculating the flow of a two-phase mixture, the no-slip conditions were set for the velocity components of the carrier medium and the dispersed component at all solid boundaries; this formulation of the boundary conditions corresponds to a mathematical model of the viscous medium motion. The Poisson equation (Krylov et al. 1977; Salyanov 1997), which describes the electric field potential (6), was solved by the finite difference method using the iterative scheme (Krylov et al. 1977) on the mesh generated for gas dynamic calculations to take into account the influence of the Coulomb force (Salyanov 1997) when solving the equations of a two-phase medium dynamics, and also allow for the distribution of the “average density” of the fractions of the dispersed phase at the fragmentation nodes of the physical area at solving the Poisson equation.

When implementing the numerical algorithm, uniform Neumann boundary conditions were set at the outlet boundary of the channel for all dynamic functions of the carrier medium and fractions of the dispersed phase, except for the longitudinal components of the velocity. For the longitudinal component of the velocity of the gas and fractions of the dispersed component at the inlet boundary of the channel, the initial velocity u_0 was set; for the transverse components of the velocity, uniform Neumann boundary conditions were specified. At the inlet boundary of the channel, for the average density of the fractions of the dispersed component of the gas suspension, the input values of the average density were set. On solid surfaces, the components of the velocity of the carrier phase and fractions of the dispersed phase were set equal to zero; for the function of the potential of the electric field, the values of the potential on the side surfaces and the homogeneous Neumann boundary conditions on the remaining boundaries were set. For all other dynamic functions, the homogeneous Neumann boundary conditions were set:

$$u_1(t,1,j) = u_0,\, u_k(t,1,j) = u_0,$$

$$v_1(t,1,j)=v_1(t,2,j),v_k(t,1,j)=v_k(t,2,j),$$

$$u_1(t,N_x,j)=u_1(t,N_x-1,j),u_k(t,N_x,j)=u_k(t,N_x-1,j),$$

$$v_1(t,N_x,j)=v_1(t,N_x-1,j),v_k(t,N_x,j)=v_k(t,N_x-1,j),$$

$$u_1(t,i,1)=0,u_k(t,i,1)=0,\ v_1(t,i,1)=0,v_k(t,i,1)=0,$$

$$u_1(t,i,N_y)=0,u_k(t,i,N_y)=0,\ v_1(t,i,N_y)=0,v_k(t,i,N_y)=0,$$

$$\rho_1(t,1,j)=\rho_1(t,2,j),\rho_k(t,1,j)=\rho_{k0}\alpha_0,$$

$$\rho_1(t,N_x,j)=\rho_1(t,N_x-1,j),\rho_k(t,N_x,j)=\rho_k(t,N_x-1,j),$$

$$\rho_1(t,i,1)=\rho_1(t,i,2),\rho_k(t,i,1)=\rho_k(t,i,2),$$

$$\rho_1(t,i,N_y)=\rho_1(t,i,N_y-1),\ \rho_k(t,i,N_y)=\rho_k(t,i,N_y-1),$$

$$e_1(t,1,j)=e_1(t,2,j),e_k(t,1,j)=e_k(t,2,j),$$

$$e_1(t,N_x,j)=e_1(t,N_x-1,j),e_k(t,N_x,j)=e_k(t,N_x-1,j),$$

$$e_1(t,i,1)=e_1(t,i,2),e_k(t,i,1)=e_k(t,i,2),$$

$$e_1(t,i,N_y)=e_1(t,i,N_y-1),e_k(t,i,N_y)=e_k(t,i,N_y-1),$$

$$p(t,1,j)=p(t,2,j),\ p(t,N_x,j)=p(t,N_x-1,j),$$

$$p(t,i,1)=p(t,i,2),\ p(t,i,N_y)=p(t,i,N_y-1).$$

$$\varphi(t,1,j)=\varphi(t,2,j),\ \varphi(t,N_x,j)=\varphi(t,N_x-1,j),$$

$$\varphi(t,i,1)=\varphi_{0l},\ \varphi(t,i,N_y)=\varphi_{0u}.$$

In this work, we considered the motion of an electrically charged gas suspension of a polydisperse composition in a channel open on both sides. Channel length L = 1 meter, channel width h = 0.1 meters. The number of nodes in the longitudinal and transverse directions were $N_x = 300$, $N_y = 60$, respectively. The calculation accuracy can be determined as– $\Delta = O\left(max\left(\Delta x^2, \Delta y^2, \Delta t^2\right)\right) \approx 0.00001$. When modeling, the following parameters of the carrier phase of the gas suspension were set: M = 0.029 kg/mol is the molar mass of air, the thermal conductivity of the carrier medium was assumed to be λ = 0.02553 W/(m K), the dynamic viscosity of the carrier medium was μ = 1, 72 10-5 Pa s, γ = 1.4, R = 8.31 J/(mol K). It was assumed that at the initial moment the medium moves with a speed u_0=3.8 m/s, the initial vertical speed is equal to zero. The initial volume content of the gas suspension fractions was $\alpha_{k0} = \alpha_0 = 0.000033$, while carrier medium density, i. e., air density ρ_{10} = 1.2 kg/m^3. For the same density of the material ($\rho_{20} = \rho_{30} = \rho_{40}$ = 1850 kg/m^3) of particles, the dispersity of the particles was d_1 = 2 μm, d_2 = 4 μm, d_3 = 10 μm. For different densities of materials, dispersion was $d_1 = d_2 = d_3$ = 20 μm. The simulated process of movement of an electrically charged gas suspension in a channel with antifoam potentials on the walls corresponds to the process of functioning of an electrostatic precipitator (Chekalov et al. 2021).

Calculation results

An electric potential φ_1 = 25,000 V was applied to the upper wall of the channel (y = h), and an electric potential φ_2 = –25,000 V was applied to the lower wall (y = 0) (see Fig. 1). The specific mass charge of the dispersed phase was taken equal to q_0 = 0.0001 C/kg.

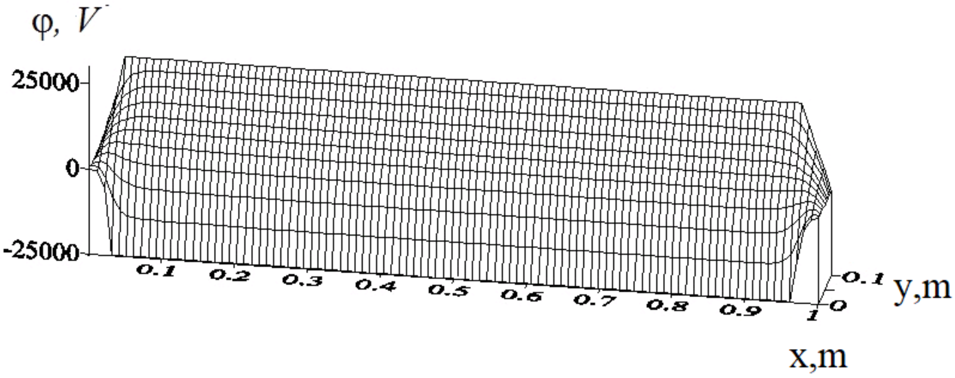

Fig. 1. Distribution of the electric field potential

Fig. 2 shows the spatial distribution of the velocity modulus of the carrier medium $V_1 = \sqrt{u_1^2 + v_1^2}$ at the time t = 0.5 s. One can observe a “parabolic” viscous profile of the flow of the carrier medium in the channel (Loitsyansky 2003).

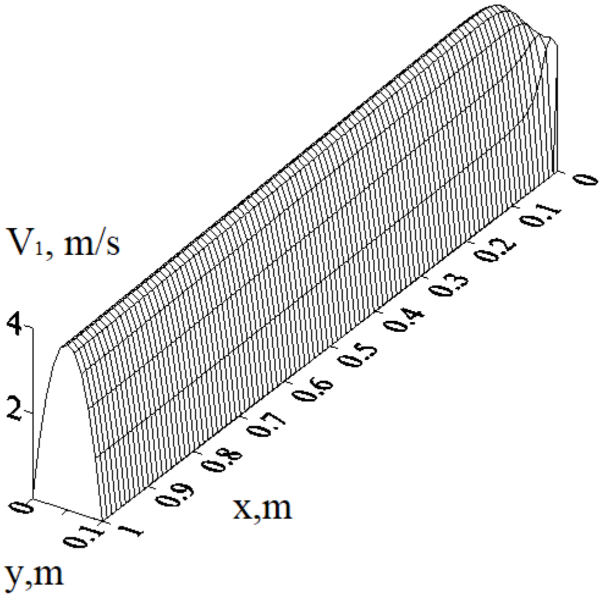

Fig. 2. Distribution of the modulus of gas velocity in the channel, time t = 0.5 s

The results of calculations of the specific Coulomb force demonstrate that at the entrance to the channel, the particles are slowed down by the Coulomb force, and at the exit from the channel, the Coulomb force accelerates the movement of the dispersed phase fractions in the longitudinal direction (see Fig. 3). Thus, we can note the influence of the boundaries of the computational domain, i. e., the "edge effect" on the specific Coulomb force acting on the dispersed component of the aerosol. Along the channel in the direction of the x-axis, the value of the y-component of the specific Coulomb force is directed to the bottom plate. In the direction of the x-axis, the y-component of the specific Coulomb force is distributed evenly (Fig. 4a). In the transverse direction, the specific Coulomb force acts in the direction of the lower negatively charged plate (Fig. 4b). The highest absolute value of the specific Coulomb force is observed near the bottom wall of the channel.

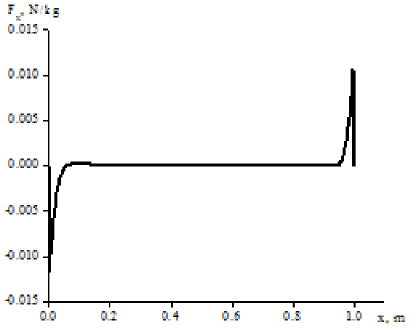

Fig. 3. Spatial distribution of the x-component of the specific Coulomb force in the direction of the x-axis, time t = 0.5 s

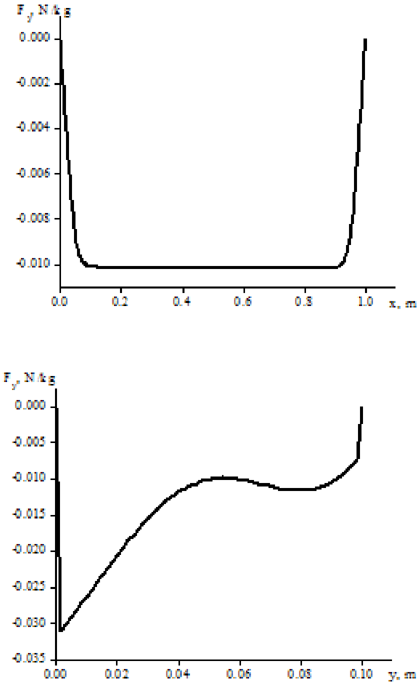

Fig. 4. Distribution of the y-component of the Coulomb force in the direction of the x-axis (y = h/2).
Fig. 4a. Distribution of the y-component of the Coulomb force in the direction of the y-axis (x = L/2);
Fig. 4b. time point t = 0.5 s

Let us consider the effect of particle dispersion of the same particle material density (ρ_{i0} = 1,850 kg/m^3, i = 2–4) on the process of mass transfer of fractions of the dispersed component of a gas suspension in an electric field. Both in the direction of the x-axis (Fig. 5a) and in the direction of the y-axis (Fig. 5b), large particles have a greater value of the y-component of the velocity of movement in the direction of the lower plate, to which the potential of the opposite value is applied. This can be explained by the fact that larger particles have more mass, which means that in the mass model of electric charge, the electric charge of larger particles is greater and thus they are more affected by the electric field. For all particle sizes, the distribution of the vertical component of the velocity of fractions of the dispersed component of the gas suspension reaches the maximum value in modulus on the lower, negatively charged plate and is uniformly distributed in the longitudinal direction.

The action of the Coulomb force on particles of different fractions, differing in particle size, determines the volume content of the fractions in the longitudinal and transverse directions. As the particle size of the fractions of the dispersed component increases, the absorption of the volume content of the fractions increases when moving through the channel in transverse and longitudinal sections (Fig. 6 (a–b)).

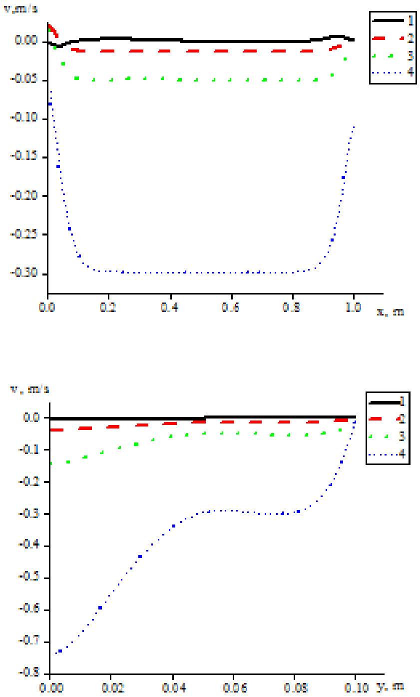

Fig. 5. Distributions of the y-component of the velocity of the gas suspension components along the x-axis (y = h/2). Fig. 5a. Distribution of the y-component of the velocity of the gas suspension components along the y-axis (x = L/2); Fig. 5b. Line 1—carrier medium, line 2—d = 2 μm, line 3—d = 4 μm, line 4—d = 10 μm, time t = 0.5 s

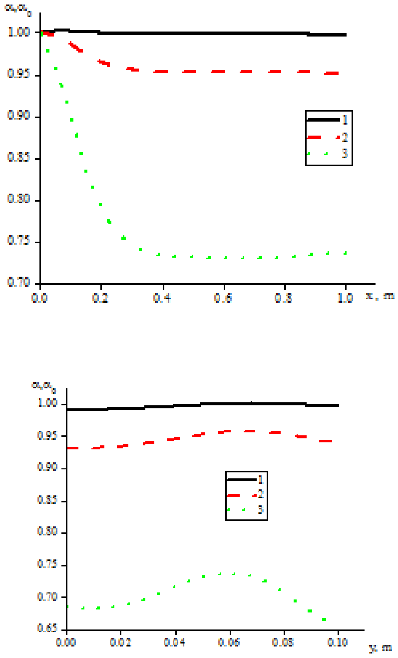

Fig. 6. Distribution of the volume content of the fractions of the dispersed component of the gas suspension along the x axis (y = h/2); Fig. 6a. Distribution of the volume content of fractions of the dispersed component along the y-axis (x = L/2); Fig. 6b. (ρ_{i0} = 1850 kg/m^3) line 1—d = 2 μm, line 2—d = 4 μm, line 3—d = 10 μm, time t = 0.5 s

Let us consider the influence of the physical density of the material of dispersed particles on the dynamics of particles in the Coulomb field with the same dispersion of particles, d_i = 20 μm, i = 2–4. Particles of denser materials have a higher settling rate (Fig. 7 (a–b)). This can be explained by the fact that in the mass model of the electric charge of the dispersed aerosol component, the charge of a dispersed particle with the same size is determined by its mass. For the same size of electrically charged dispersed particles, the density of the material affects the volume content of gas suspension fractions. For the same dispersion of particles and different densities of the particle material, the distribution of the vertical component of the velocity of the fractions of the dispersed component of the gas suspension reaches the maximum value in modulus on the lower negatively charged plate and is uniformly distributed in the longitudinal direction.

Distribution of the volume content of fractions as in the longitudinal section of the channel (Fig. 8a) and in the cross section (Fig. 8b), demonstrate that the loss of the volume content of fractions during the passage of the channel with the same dispersion of particles is directly proportional to the density of the material of the fraction. This pattern can be explained by the influence of the particle material density on the settling rate of particles having the same size.

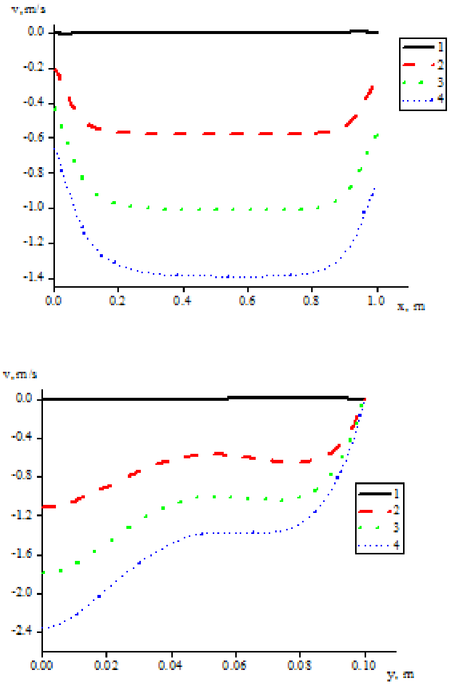

Fig. 7. Distributions of the y-component of the velocity of the gas suspension components along the x-axis (y = h/2). Fig. 7a. Distribution of the y-component of the velocity of the gas suspension components along the y-axis (x = L/2); Fig. 7b (d = 20 μm) line 1—carrier medium, line 2—ρ_{20} = 1,000 kg/m³, line 3—ρ_{30} = 1,850 kg/m³, line 4—ρ_{40} = 2,700 kg/m³, time t = 0.5 s

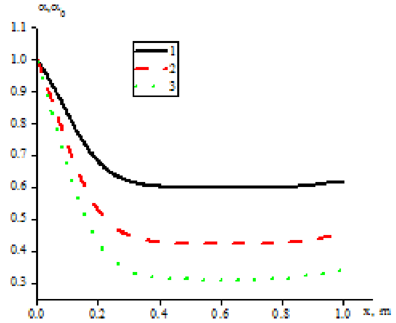

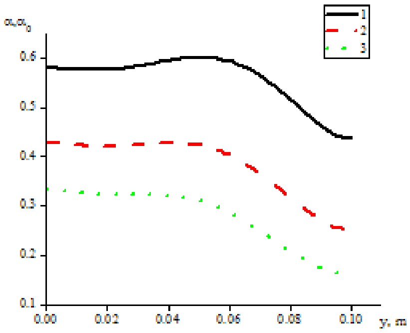

Fig. 8. Distribution of the volume content of the fractions of the dispersed component of the gas suspension along the x axis (y = h/2). Fig. 8a. Distribution of the volume content of fractions of the dispersed component along the y-axis (x = L/2); Fig. 8b. (d = 20 μm) line 1—ρ_{20} = 1,000 kg/m^3, line 2—ρ_{30} = 1,850 kg/m^3, line 3—ρ_{40} = 2,700 kg/m^3, time t = 0.5 s

To determine the volume of precipitated particles of the j-th fraction, the scheme of right-handed rectangles was used for the numerical integration of a certain integral of right-handed rectangles (Verzhbitsky 2002):

$$V_j(t)=\int_0^L \alpha_j(x,0,t)\,dx \approx \sum_{i=2}^{N_x}\alpha_j(x_i-x_{i-1})=\sum_{i=2}^{N_x}\alpha_j(x_i,0,t)\Delta x\,. \tag{15}$$

The volumes of fractions of the dispersed phase deposited on the lower surface of the channel are directly proportional to the particle size of the fraction at the same density of the particle material (Fig. 9). The volumes of precipitated fractions are also directly proportional to the density of the particle material (Fig.10). Calculations indicate that deposition of dispersed particles on the electrode surface in an electric field is determined by the mass of the particles. With the same particle material density, larger particles are more intensively deposited since larger particles are more massive. With the same particle size, particles from denser materials are more intensively deposited.

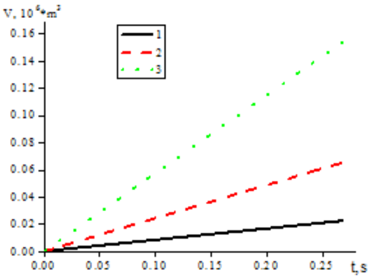

Fig. 9. Time dependence of the volume of dispersed particles of gas suspension deposited on the bottom plate for different particle sizes (ρ_{i0} = 1,850 kg/m^3), line 1—d = 2 μm, line 2—d = 4 μm, line 3—d = 10 μm

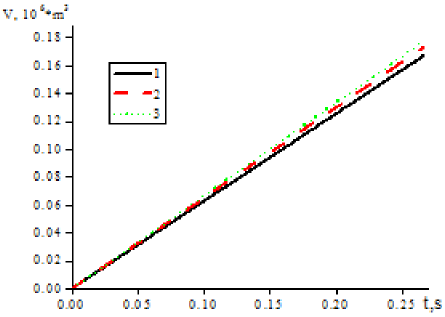

Fig. 10. Time dependence of the volume of dispersed particles of gas suspension deposited on the bottom plate for different particle material densities (d_i = 20 μm), line 1—ρ_{20} = 1,000 kg/m^3, line 2—ρ_{30} = 1,850 kg/m^3, line 3—ρ_{40} = 2,700 kg/m^3

Conclusions

In this work, numerical calculations of the dynamics of an electrically charged polydisperse gas suspension in a channel in which potentials of different signs are applied to the side surfaces are carried out. The influence of the parameters of dispersed particles on the dynamics of particles in a channel under the action of aerodynamic forces and the Coulomb force has been analyzed. When moving along the channel, the vertical component of the particle velocity is directed to the plate, to which a potential with a sign opposite to the sign of the charge of dispersed particles is applied. It was determined that at the same density of the material, the intensity of sedimentation of the fraction is determined by the size of the particles; at the same dispersion of particles, the fractions of particles with a higher density of the material are most intensively deposited. In this case, the dispersity of the particles of the fraction has a greater effect on the volume of the fraction deposited on the electrode plate than the density of the material of the fraction.

The vertical component of the velocity of the fraction of the dispersed component increases with an increase in the particle size; at a fixed particle size, the vertical component of the particle velocity increases with an increase in the density of the material.

The influence of the parameters of the fractions of the electrically charged dispersed aerosol component on the dynamics of a multifractional aerosol in an external electric field is considered. As a result of the analysis of the results of numerical calculations, the influence of the particle size and density of the fraction material on the vertical component of the velocity, the volume content of the fraction in various sections of the channel, and the rate of deposition of particles of the fraction on the electrode plate were determined.

The regularities obtained by numerical simulation can be explained by the fact that particles of a larger size or particles of denser material (provided particles are of the same size), have a larger electric charge and, therefore, a larger Coulomb force acts on them. In this case, particles of large sizes overcome the aerodynamic resistance of the gas more easily. As a result of mathematical modeling, it was determined that the intensity of fraction filtration by an electric filter is determined by particle size and material density. The revealed regularities can be used in optimizing electric filters for gas suspensions. The regularities revealed in the work suggest the possibility of separating fractions of an electrically charged aerosol into fractions with different density and particle size. The development of the presented mathematical model of the dynamics of an electrically charged multifractional aerosol will take into account different charges of particles of different fractions.

Conflict of Interest

The author declares that there is no conflict of interest, either existing or potential.

References

Altunin, V. A., Altunin, K. V., Aliev, I. N. et al. (2012) Analysis of investigations of electric fields in different media and conditions. *Journal of Engineering Physics and Thermophysics*, 85 (4), 959–976. https://doi.org/10.1007/s10891-012-0736-4 (In English)

Bastykova, N. K., Kodanova, S. K., Ramazanov, T. S. et al. (2021) Investigation of the evolution of Be, Ni, Mo, and W dust grains in fusion plasma. *Plasma Physics Reports*, 47 (1), 92–95. https://doi.org/10.1134/S1063780X21010049 (In English)

Chekalov, L. V., Guzaev, V. A., Smirnov, M. E. (2021) *Povyshenie effektivnosti elektrofil'trov teplovykh elektrostantsij putem sovershenstvovaniya osaditel'nykh elektrodov [Enhancement the efficiency of electrostatic precipitators of thermal power plants by improving the electrodes volume]. Elektricheskie stantsii — Electrical Stations*, 7, 48–54. http://dx.doi.org/10.34831/EP.2021.1080.7.008 (In Russian)

Fedorov, A. V., Fomin, V. M., Khmel, T. A. (2015) *Volnovye protsessy v gazovzvesyakh chastits metallov [Wave processes in gas suspensions of metal particles]*. Novosibirsk: Parallel' Publ., 305 p. (In Russian)

Fletcher, C. A. (1988) *Computation techniques for fluid dynamics*. Berlin: Springer-Verlag, 502 p. (In English)

Ignatov, A. M. (2020) Nonlinear dynamics of a linear dust particle chain. *Plasma Physics Reports*, 46 (9), 936–942. https://doi.org/10.1134/S1063780X20090044 (In English)

Kolotinskii, D. A., Nikolaev, V. S., Timofeev, A. V. (2021) Effect of structural inhomogeneity and nonreciprocal effects in the interaction of macroparticles on the dynamic properties of a dusty plasma monolayer. *Journal of Experimental and Theoretical Physics Letters*, 113 (8), 510–517. https://doi.org/10.1134/S0021364021080063 (In English)

Krylov, V. I., Bobkov, V. V., Monastyrnyj, P. I. (1977) *Vychislitel'nyye metody. T. 2 [Computational methods. Vol. 2]*. Moscow: Nauka Publ., 401 p. (In Russian)

Kutushev, A. G. (2003) *Matematicheskoe modelirovanie volnovykh protsessov v aerodispersnykh i poroshkoobraznykh sredakh [Mathematical simulation of wave processes in aero dispersed and powdered media]*. Saint Petersburg: Nedra Publ., 284 p. (In Russian)

Loitsyansky, L. G. (2003) *Mekhanika zhidkosti i gaza [Mechanics of fluid and gas]*. Moscow: Drofa Publ., 784 p. (In Russian)

Muzafarov, I. F., Utyuzhnikov, S. V. (1993) Primenenie kompaktnykh raznostnykh skhem k issledovaniyu nestatsionarnykh techenij szhimaemogo gaza. [Application of compact difference schemes to the study of unsteady flows of a compressible gas]. *Matematicheskoe modelirovanie*, 5 (3), 74–83. (In Russian)

Nigmatullin, R. I. (1978) *Osnovy mekhaniki geterogennykh sred [Fundamentals of the mechanics of heterogeneous media]*. Moscow: Nauka Publ., 336 p. (In Russian)

Salyanov, F. A. (1997) *Osnovy fiziki nizkotemperaturnoj plazmy, plazmennykh apparatov i tekhnologij [Fundamentals of low-temperature plasma physics, plasma apparatuses and technologies]*. Moscow: Nauka Publ., 240 p. (In Russian)

Sinkevich, O. A. (2016) On the instability of the electrically charged interface between a two-phase thundercloud and turbulent atmosphere. *High Temperature*, 54 (6), 775–781. https://doi.org/10.1134/S0018151X16060201 (In English)

Tada, Y., Yoshioka, S., Takimoto, A., Hayashi, Y. (2016) Heat transfer enhancement in a gas–solid suspension flow by applying electric field. *International Journal of Heat and Mass Transfer*, 93, 778–787. https://doi.org/10.1016/j.ijheatmasstransfer.2015.09.063 (In English)

Tukinakov, D. A. (2019) Numerical simulation of shock-wave flows in a gas suspension with inhomogeneous concentration of the dispersed phase. *Russian Aeronautics*, 62 (1), 59–65. https://doi.org/10.3103/S1068799819010082 (In English)

Tukmakov, A. L. (2003) Origination of in-phase oscillations of thin plates with aeroelastic interaction. *Journal of Applied Mechanics and Technical Physics*, 44 (1), 64–68. https://doi.org/10.1023/A:1021729729960 (In English)

Tukmakov, A. L., Tukmakov, D. A. (2017) Dynamics of a charged gas suspension with an initial spatially nonuniform distribution of the average dispersed phase density during the transition to the equilibrium state. *High Temperature*, 55 (4), 491–495. (In English)

Tukmakov, D. A. (2022a) One-dimensional continuum finite-difference model of the dynamics of a dusty medium in aerodynamic, electric and gravitational fields. *Journal of Physics: Conference Series*, vol. 2270. II International Conference "Gas Discharge Plasma and Synthesis of Nanostructures", article 012016. http://dx.doi.org/10.1088/1742-6596/2270/1/012016 (In English)

Tukmakov, D. A. (2022b) One-dimensional unsteady numerical model of gas suspension flow caused by gravitational sedimentation of particles with a constant velocity. *Journal of Applied Mechanics and Technical Physics*, 63 (7), 1218–1226. https://doi.org/10.1134/S0021894422070148 (In English)

Tukmakov, D. A. (2023) Numerical simulation of oscillations of aerosol with a low dispersed phase concentration in a closed tube by the continuum mathematical model. *Technical Physics*, 67 (12), 764–770. https://doi.org/10.1134/S1063784222110032 (In English)

Verzhbitsky, V. M. (2002) *Osnovy chislennykh metodov [Fundamentals of numerical methods]*. Moscow: Vysshaya shkola Publ., 840 p. (In Russian)

Physics of Complex Systems, 2023, vol. 4, no. 3
www.physcomsys.ru

Theoretical physics.
Physics of atoms and molecules

UDC 539.1

EDN QEBNZO
https://www.doi.org/10.33910/2687-153X-2023-4-3-124-130

Atomic data on inelastic collisional process for YH

V. A. Vasileva[1], S. A. Yakovleva✉[1]

[1] Herzen State Pedagogical University of Russia, 48 Moika Emb., Saint Petersburg 191186, Russia

Authors

Vera A. Vasileva, ORCID: 0009-0009-9622-9128, e-mail: veravasilieva2000@gmail.ru

Svetlana A. Yakovleva, ORCID: 0000-0002-8889-7283, e-mail: cvetaja@gmail.com

For citation: Vasileva, V. A., Yakovleva, S. A. (2023) Atomic data on inelastic collisional process for YH. *Physics of Complex Systems*, 4 (3), 124–130. https://www.doi.org/10.33910/2687-153X-2023-4-3-124-130 EDN QEBNZO

Received 9 June 2023; reviewed 5 July 2023; accepted 5 July 2023.

Funding: This study was supported by the Russian Science Foundation (the Russian Federation), Project No. 22-23-01181.

Abstract. The cross sections and rate coefficients for inelastic processes in low-energy collisions of yttrium and hydrogen atoms and ions are calculated. Three ionic states of $Y^+ + H^-$ are considered. Calculations of non-adiabatic nuclear dynamics in all molecular symmetries of each ionic state are performed. Inelastic processes due to non-adiabatic transitions between 65 different states of the YH quasimolecule are considered. In total, 1,796 inelastic processes are treated and their cross sections for collision energy range from 0.001 to 100 eV and rate coefficients for temperatures from 1,000 to 10,000 K are calculated and analyzed. Inelastic processes with large rate coefficients are important for treating Non-LTE effects in astrophysical modeling.

Keywords: atomic data, inelastic processes, non-adiabatic transitions, yttrium, hydrogen

Introduction

Chemical elements that are formed in neutron-capture processes (n-processes) such as Sr, Ba, Y, La, Zr are of great interest to astrophysical studies. The information on the abundances of these elements in stars and star clusters is important in order to understand n-processes as a source of gaseous environment enrichment (Busso et al. 2001), chemical evolution of galactic disks (Chiappini, Gratton 1997; Serminato et al. 2009) and the production of star clusters (Brewer, Carney 2006).

Neutron capture involves two main processes that depend on the density of the neutron flux: a slow process (s-process) and a rapid process (r-process). The main sources of elements produced in neutron capture (primarily, yttrium and barium) are stars with small and intermediate masses in the asymptotic giant branch. They enrich the interstellar medium with these chemical elements that enter stars during their formation (Travaglio et al. 1999).

In astrophysical modeling of various gaseous environments, a model atom for each chemical element is constructed. It includes energy levels and the data on radiative and non-radiative inelastic processes due to collisions with electrons, atoms, and molecules. Collisions of different atoms and ions with hydrogen atoms and negative ions are one of the greatest uncertainties in astrophysical modeling as hydrogen is the most abundant element in the universe. For this reason, a theoretical calculation of molecular data on inelastic hydrogen collisions is important for astrophysics.

Brief theory

Inelastic processes in collisions of yttrium atoms and positive ions and hydrogen atoms and negative ions are studied within the Born-Oppenheimer formalism using asymptotic model approach (Belyaev 2013).

This approach allows to model non-adiabatic regions due to ionic-covalent interaction via constructing the electronic Hamiltonian matrix in the diabatic representation. The diagonal matrix elements are the diabatic potential energies determined by the Coulomb potential in case of the ionic term and by the asymptotic energy of the scattering channel in case of the covalent term; off-diagonal matrix elements that represent ionic-covalent interaction are calculated using a semi-empirical formula from (Olson et al. 1971).

Non-adiabatic nuclear dynamics is treated within the Landau-Zener multichannel model. Transition probabilities in one non-adiabatic region are calculated using an adiabatic potential-based formula (Belyaev, Lebedev 2011), while state-to-state transition probability $p_{if}(J, E)$ for a particular collision energy E and total angular momentum quantum number J is calculated using analytical expressions that take all non-adiabatic regions into account (Yakovleva et al. 2016). Inelastic cross sections $\sigma_{if}(E)$ and rate coefficients K_{if} for exothermic processes ($i > f$) are then calculated using the following equations:

$$\sigma_{if}\left(E\right)=\frac{\pi\hbar^2 p_i^{stat}}{2\mu E}\sum_{J=0}^{J_{max}} P_{if}\left(J,E\right)\left(2J+1\right),$$

$$K_{if}=\sqrt{\frac{8}{\pi\mu\left(k_B T\right)^3}}\int_0^{\infty}\sigma_{if}\left(E\right)E\exp\left(-\frac{E}{k_B T}\right)dE,$$

where μ is the reduced nuclear mass, p_i^{stat} is the statistical probability of population of the initial channel i, k_B is the Boltzmann constant. For endothermic processes ($k < j$) cross sections and rate coefficients are calculated using detailed balance equations:

$$\sigma_{kj}\left(E\right)=\sigma_{kj}\left(E+\Delta E_{kj}\right)\frac{p_k^{stat}}{p_j^{stat}}\frac{E+\Delta E_{kj}}{E},$$

$$K_{kj}\left(T\right)=K_{jk}\left(T\right)\frac{p_k^{stat}}{p_j^{stat}}\exp\left(\frac{\Delta E_{kj}}{k_B T}\right),$$

where ΔE_{kj} is the energy defect between the asymptotic energies E_k and E_j.

YH calculations

The present study of inelastic processes in ytterbium-hydrogen collisions is performed for three sets of molecular states. As the asymptotic model approach (Belyaev 2013) allows taking into account only ionic-covalent interaction, we include only those covalent molecular states that have the same molecular symmetries. Each set contains one of the ionic molecular terms $Y^{+}+H^{-}$ and the covalent molecular states that have the same core electrons configuration. All the molecular states, corresponding scattering channels and asymptotic energies for these tree sets are summarized in Tables 1, 2 and 3:

Table 1: 5 covalent $Y(5s^2\ {}^2L) + H(1s\ {}^2S)$ molecular states and ionic state $Y^{+}(5s^2\ {}^1S) + H^{-}(1s^2\ {}^1S)$ with ${}^1\Sigma^{+}$ molecular symmetry;

Table 2: 35 covalent $Y(4d5s\ {}^{2,4}L) + \mathrm{H}(1s\ {}^2S)$ molecular states and ionic state $Y^{+}(4d5s\ {}^3D) + H^{-}(1s^2\ {}^1S)$ with ${}^3\Sigma^{+}$, ${}^3\Pi$, ${}^3\Delta$ molecular symmetries;

Table 3: 22 covalent $Y(4d5s\ {}^{1,3}L) + H(1s^2S)$ molecular states and ionic state $Y^{+}(4d5s\ {}^1D) + \mathrm{H}^{-}(1s^2\ {}^1S)$ with ${}^1\Sigma^{+}$, ${}^1\Pi$, ${}^1\Delta$, molecular symmetries.

Table 1. The $Y({}^2L) + H(1s\ {}^2S)$ and $Y^{+}(5s^2\ {}^1S) + H^{-}(1s^2\ {}^1S)$ molecular channels, the corresponding asymptotic atomic states, and the asymptotic energies with respect to the ground state

j	Asymptotic atomic states	Molecular symmetries	Asymptotic energies (eV)
1	$Y(4d5s^2\ {}^2D) + H(1s\ {}^2S)$	${}^1\Sigma^{+}$	0.03885
2	$Y(5s^2\ 5p\ {}^2P) + H(1s\ {}^2S)$	${}^1\Sigma^{+}$	1.37165
3	$Y(5s^2\ 6s\ {}^2S) + H(1s\ {}^2S)$	${}^1\Sigma^{+}$	3.92677

Table 1. Completion

4	$Y(5s^2\,(^2D)5d\;^2D) + H(1s\;^2S)$	$^1\Sigma^+$	4.24606
5	$Y(5s^2\,(^1S)6p\;^2P) + H(1s\;^2S)$	$^1\Sigma^+$	4.61472
ionic	$Y+\,(5s^2\;^1S) + H-\,(1s^2\;^1S)$	$^1\Sigma^+$	5.46326

Table 2. The $Y(^{2,4}L) + H(1s\;^2S)$ and $Y^+(4d5s\;^3D) + H^-(1s^2\;^1S)$ molecular channels, the corresponding asymptotic atomic states, and the asymptotic energies with respect to the ground state

j	Asymptotic atomic states	Molecular symmetries			Asymptotic energies (eV)
1	$Y(4d5s^2\;^2D) + H(1s\;^2S)$	$^3\Sigma^+$	$^3\Pi$	$^3\Delta$	0.03885
2	$Y(4d^2(^3F)5s\;^4F) + H(1s\;^2S)$	–	$^3\Pi$	$^3\Delta$	1.39762
3	$Y(4d^2\,(^3P)5s\;^4P) + H(1s\;^2S)$	–	$^3\Pi$	–	1.90689
4	$Y(4d^2\,(^3F)5s\;^2F) + H(1s\;^2S)$	–	$^3\Pi$	$^3\Delta$	1.93805
5	$Y(4d5s(^3D)5p\;^4F) + H(1s\;^2S)$	$^3\Sigma^+$	$^3\Pi$	$^3\Delta$	1.94401
6	$Y(4d^2\,(^1D)5s\;^2D) + H(1s\;^2S)$	$^3\Sigma^+$	$^3\Pi$	$^3\Delta$	1.99508
7	$Y(4d5s(^3D)5p\;^2D) + H(1s\;^2S)$	–	$^3\Pi$	$^3\Delta$	1.99599
8	$Y(4d5s(^3D)5p\;^4D) + H(1s\;^2S)$	–	$^3\Pi$	$^3\Delta$	2.08841
9	$Y(4d^2(^1G)5s\;^2G) + H(1s\;^2S)$	$^3\Sigma^+$	$^3\Pi$	$^3\Delta$	2.29434
10	$Y(4d5s(^3D)5p\;^4P) + H(1s\;^2S)$	$^3\Sigma^+$	$^3\Pi$	–	2.36513
11	$Y(4d^2\,(^3P)5s\;^2P) + H(1s\;^2S)$	–	$^3\Pi$	–	2.39859
12	$Y(4d5s(^3D)5p\;^2F) + H(1s\;^2S)$	$^3\Sigma^+$	$^3\Pi$	$^3\Delta$	2.69638
13	$Y(4d^2(^1S)5s\;^2S) + H(1s\;^2S)$	$^3\Sigma^+$	–	–	2.90930
14	$Y(4d5s(^3D)5p\;^2P) + H(1s\;^2S)$	$^3\Sigma^+$	$^3\Pi$	–	3.04487
15	$Y(4d5s(^1D)5p\;^2F) + H(1s\;^2S)$	$^3\Sigma^+$	$^3\Pi$	$^3\Delta$	3.06669
16	$Y(4d5s(^1D)5p\;^2D) + H(1s\;^2S)$	–	$^3\Pi$	$^3\Delta$	3.06818
17	$Y(4d5s(^1D)5p\;^2P) + H(1s\;^2S)$	$^3\Sigma^+$	$^3\Pi$	–	3.47492
18	$Y(4d5s(^3D)6s\;^4D) + H(1s\;^2S)$	$^3\Sigma^+$	$^3\Pi$	$^3\Delta$	4.15074
19	$Y(4d5s(^3D)6s\;^2D) + H(1s\;^2S)$	$^3\Sigma^+$	$^3\Pi$	$^3\Delta$	4.51635
20	$Y(4d5s(^1D)6s\;^2D) + H(1s\;^2S)$	$^3\Sigma^+$	$^3\Pi$	$^3\Delta$	4.58576
21	$Y(4d5s(^3D)5d\;^4D) + H(1s\;^2S)$	$^3\Sigma^+$	$^3\Pi$	$^3\Delta$	4.79801
22	$Y(4d5s(^3D)6p\;^4D) + H(1s\;^2S)$	–	$^3\Pi$	$^3\Delta$	4.81911
23	$Y(4d5s(^3D)6p\;^4F) + H(1s\;^2S)$	$^3\Sigma^+$	$^3\Pi$	$^3\Delta$	4.82798
24	$Y(4d5s(^3D)5d\;^4G) + H(1s\;^2S)$	$^3\Sigma^+$	$^3\Pi$	$^3\Delta$	4.82840
25	$Y(4d5s(^3D)6p\;^2F) + H(1s\;^2S)$	$^3\Sigma^+$	$^3\Pi$	$^3\Delta$	4.83337
26	$Y(4d5s(^3D)5d\;^4S) + H(1s\;^2S)$	$^3\Sigma^+$	–	–	4.83556
27	$Y(4d5s(^3D)5d\;^2P) + H(1s\;^2S)$	–	$^3\Pi$	–	4.85594
28	$Y(4d5s(^3D)6p\;^2D) + H(1s\;^2S)$	–	$^3\Pi$	$^3\Delta$	4.86874
29	$Y(4d5s(^3D)6p\;^4P) + H(1s\;^2S)$	$^3\Sigma^+$	$^3\Pi$	–	4.90231
30	$Y(4d5s(^3D)5d\;^4F) + H(1s\;^2S)$	–	$^3\Pi$	$^3\Delta$	4.92456
31	$Y(4d5s(^3D)5d\;^2F) + H(1s\;^2S)$	–	$^3\Pi$	$^3\Delta$	4.92681
32	$Y(4d5s(^3D)5d\;^4P) + H(1s\;^2S)$	–	$^3\Pi$	–	5.01564

Table 2. Completion

33	$Y(4d5s(^3D)5d\ ^2D) + H(1s\ ^2S)$	–	$^3\Pi$	$^3\Delta$	5.14169
34	$Y(4d5s(^1D)5d\ ^2D) + H(1s\ ^2S)$	$^3\Sigma^+$	$^3\Pi$	$^3\Delta$	5.16591
35	$Y(4d5s(^1D)5d\ ^2P) + H(1s\ ^2S)$	–	$^3\Pi$	–	5.29103
ionic	$Y^+(4d5s\ ^3D) + H^-(1s^2\ ^1S)$	$^3\Sigma^+$	$^3\Pi$	$^3\Delta$	5.61116

Table 3. The $Y(^{1,3}L) + H(1s\ ^2S)$ and $Y^+(4d5s\ ^1D) + H^-(1s^2\ ^1S)$ molecular channels, the corresponding asymptotic atomic states, and the asymptotic energies with respect to the ground state

j	**Asymptotic atomic states**	**Molecular symmetries**			**Asymptotic energies (eV)**
1	$Y(4d5s^2\ ^2D) + H(1s\ ^2S)$	$^1\Sigma^+$	$^1\Pi$	$^1\Delta$	0.03885
2	$Y(4d^2(^3F)5s\ ^2F) + H(1s\ ^2S)$	–	$^1\Pi$	$^1\Delta$	1.93805
3	$Y(4d^2(^1D)5s\ ^2D) + H(1s\ ^2S)$	$^1\Sigma^+$	$^1\Pi$	$^1\Delta$	1.99508
4	$Y(4d5s(^3D)5p\ ^2D) + H(1s\ ^2S)$	–	$^1\Pi$	$^1\Delta$	1.99599
5	$Y(4d^2(^1G)5s\ ^2G) + H(1s\ ^2S)$	$^1\Sigma^+$	$^1\Pi$	$^1\Delta$	2.29434
6	$Y(4d^2(^3P)5s\ ^2P) + H(1s\ ^2S)$	–	$^1\Pi$	–	2.39859
7	$Y(4d5s(^3D)5p\ ^2F) + H(1s\ ^2S)$	–	$^1\Pi$	$^1\Delta$	2.69638
8	$Y(4d2(^1S)5s\ ^2S) + H(1s\ ^2S)$	$^1\Sigma^+$	–	–	2.90930
9	$Y(4d5s(^3D)5p\ ^2P) + H(1s\ ^2S)$	$^1\Sigma^+$	$^1\Pi$	–	3.04487
10	$Y(4d5s(^1D)5p\ ^2F) + H(1s\ ^2S)$	$^1\Sigma^+$	$^1\Pi$	$^1\Delta$	3.06669
11	$Y(4d5s(^1D)5p\ ^2D) + H(1s\ ^2S)$	–	$^1\Pi$	$^1\Delta$	3.06818
12	$Y(4d5s(^1D)5p\ ^2P) + H(1s\ ^2S)$	$^1\Sigma^+$	$^1\Pi$	–	3.47492
13	$Y(4d5s(^3D)6s\ ^2D) + H(1s\ ^2S)$	$^1\Sigma^+$	$^1\Pi$	$^1\Delta$	4.51635
14	$Y(4d5s(^1D)6s\ ^2D) + H(1s\ ^2S)$	$^1\Sigma^+$	$^1\Pi$	$^1\Delta$	4.58576
15	$Y(4d5s(^3D)6p\ ^2F) + H(1s\ ^2S)$	$^1\Sigma^+$	$^1\Pi$	$^1\Delta$	4.83337
16	$Y(4d5s(^3D)5p\ ^2P) + H(1s\ ^2S)$	–	$^1\Pi$	–	4.85594
17	$Y(4d5s(^3D)6p\ ^2D) + H(1s\ ^2S)$	–	$^1\Pi$	$^1\Delta$	4.86874
18	$Y(4d5s(^3D)5d\ ^2F) + H(1s\ ^2S)$	–	$^1\Pi$	$^1\Delta$	4.92681
19	$Y(4d5s(^3D)5d\ ^2D) + H(1s\ ^2S)$	$^1\Sigma^+$	$^1\Pi$	$^1\Delta$	5.14169
20	$Y(4d5s(^1D)5d\ ^2D) + H(1s\ ^2S)$	$^1\Sigma^+$	$^1\Pi$	$^1\Delta$	5.16591
21	$Y(4d5s(^1D)5d\ ^2P) + H(1s\ ^2S)$	–	$^1\Pi$	–	5.29103
22	$Y(4d5s(^1D)5d\ ^2F) + H(1s\ ^2S)$	–	$^1\Pi$	$^1\Delta$	5.46192
ionic	$Y^+(4d5s\ ^1D) + H^-(1s^2\ ^1S)$	$^1\Sigma^+$	$^1\Pi$	$^1\Delta$	5.87193

The data for the atomic levels of yttrium atom and ion and their energy values are taken from NIST (Kramida et al. 2022). Asymptotic energies are averaged over the total angular momentum quantum number *J*. It is worth noting that only one-electron transitions are included in the present investigation as two-electron transitions generally have negligible probabilities, cross sections and rate coefficients because of the narrow non-adiabatic regions (Belyaev et al. 2016; 2019; Vlasov et al. 2018).

For all the transitions between the states in the three sets of molecular states, calculations of partial cross sections and rate coefficients are performed within each molecular symmetry separately and then summed over initial and final states of the process. Cross sections are calculated for the collision energy range from 0.01 eV to 100 eV and rate coefficients — for the temperature range from 1,000 K to 10,000 K.

Results and analysis

Graphical representation of rate coefficients for the temperature T = 6,000K for all the treated processes is shown in Figs 1, 2 and 3 for the three sets of molecular states from Tables 1, 2 and 3, respectively. The rate coefficient order of magnitude is shown with color from blue to red (see the respective legend). The initial and final states labels in graphical representations correspond to those in Tables 1, 2 and 3. White color denotes either the elastic processes that are not studied in the present work (diagonal squares) or transitions between molecular states that do not have the same symmetries.

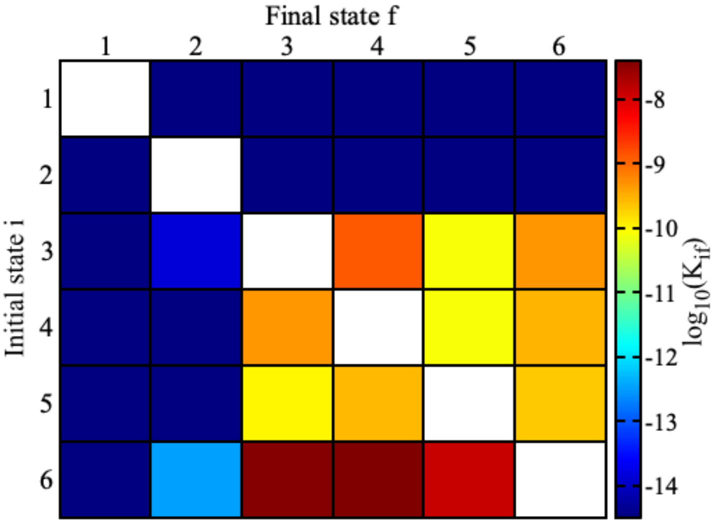

Fig. 1. Graphical representation of the inelastic processes rate coefficients in $Y(^2L) + H(1s\ ^2S)$ and $Y^+(5s^2\ ^1S) + H^-(1s^2\ ^1S)$ collisions. The labels for the initial and final states are given in Table 1.

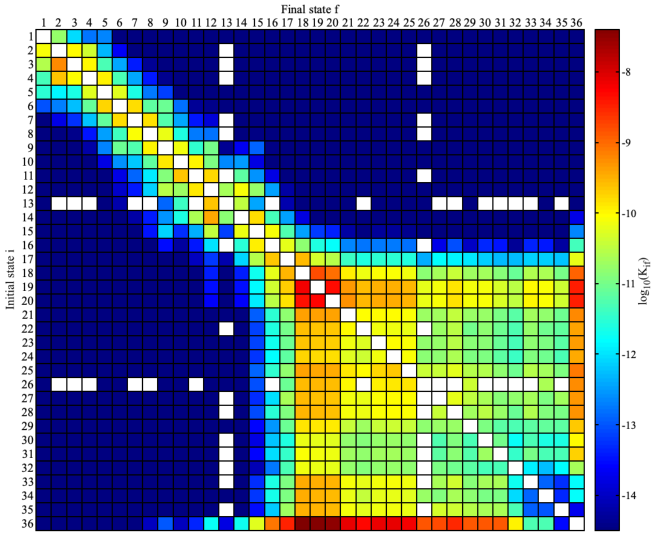

Fig. 2. Graphical representation of the inelastic processes rate coefficients in $Y(^{2,4}L) + H(1s\ ^2S)$ and $Y^+(4d5s\ ^3D) + H^-(1s^2\ ^1S)$ collisions. The labels for the initial and final states are given in Table 2.

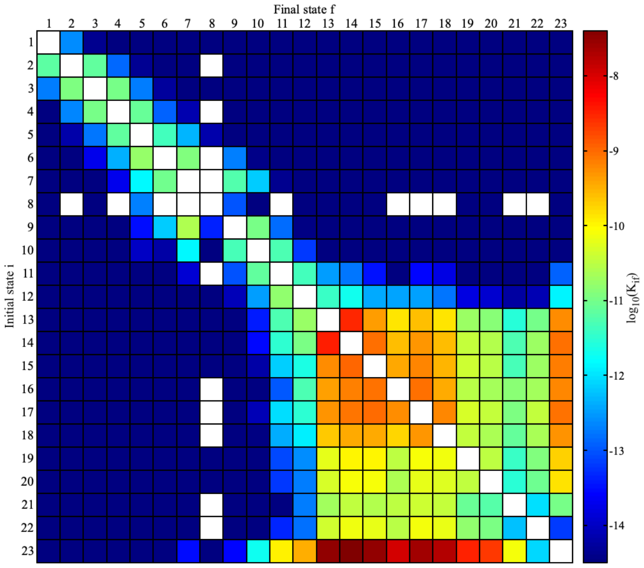

Fig. 3. Graphical representation of the inelastic processes rate coefficients in $Y(^{1,3}L) + H(1s\ ^2S)$ and $Y^+(4d5s\ 1D) + H^-(1s^2\ ^1S)$ collisions. The labels for the initial and final states are given in Table 3.

For the first group of molecular states (see Table 1) the largest rate coefficients at T = 6,000 K correspond the neutralization processes $Y^+(5s^2\ ^1S) + H^- \to Y(5s^2\ nl\ \ ^2L) + H$ (j = 6 to j = 3, 4, 5) with values:

$K_{6\to3} = 3.59 \times 10^{-8}$ cm^3 s^{-1},
$K_{6\to4} = 5.86 \times 10^{-8}$ cm^3 s^{-1},
$K_{6\to5} = 1.24 \times 10^{-8}$ cm^3 s^{-1}.

In the second molecular states group (Table 2) the largest rate coefficients at T = 6,000 K correspond the neutralization processes $Y^+(4d5s\ ^3D) + H^- \to Y(4d5s\ nl\ ^{2,4}L) + H$ (j = 36 to j = 18, 19, 20) with values:

$K_{36\to18} = 4.72 \times 10^{-8}$ cm^3 s^{-1},
$K_{36\to19} = 3.67 \times 10^{-8}$ cm^3 s^{-1},
$K_{36\to20} = 3.13 \times 10^{-8}$ cm^3 s^{-1}.

In case of the third group (Table 3) the largest rate coefficients at T = 6,000 K correspond the neutralization processes $Y^+(4d5s\ ^1D) + H^- \to Y(4d5s\ nl\ ^{1,3}L) + H$ (j = 23 to j = 13 – 18) with values:

$K_{23\to13} = 3.01 \times 10^{-8}$ cm^3 s^{-1},
$K_{23\to14} = 4.12 \times 10^{-8}$ cm^3 s^{-1},
$K_{23\to15} = 2.93 \times 10^{-8}$ cm^3 s^{-1},
$K_{23\to16} = 1.05 \times 10^{-8}$ cm^3 s^{-1},
$K_{23\to17} = 2.33 \times 10^{-8}$ cm^3 s^{-1},
$K_{23\to18} = 1.75 \times 10^{-8}$ cm^3 s^{-1},

Conclusions

The reported study of inelastic yttrium and hydrogen collisions is performed for the three sets of ionic molecular states of $Y^+ + H^-$. For each set, the study of non-adiabatic nuclear dynamics is carried out within all the molecular symmetries of a particular ionic state. Inelastic processes due to nonadiabatic transitions between 65 different states of the YH quasimolecule are considered. In total, 1,796 inelastic processes are studied, cross sections are calculated for the collision energy range from 0.001 eV to 100 eV and the rate coefficients are calculated for temperatures from 1,000 K to 10,000 K. Inelastic processes with large values of the rate coefficients may find application in non-LTE astrophysical modeling.

Conflict of Interest

The authors declare that there is no conflict of interest, either existing or potential.

Author Contributions

All the authors discussed the final work and took an equal part in writing the article.

Acknowledgements

Authors gratefully acknowledge discussions with Prof. Andrey K. Belyaev.

References

Belyaev, A. K. (2013) Model approach for low-energy inelastic atomic collisions and application to Al + H and Al+ + H−. *Physical Review A*, 88 (5), article 052704. https://doi.org/10.1103/PhysRevA.88.052704 (In English)

Belyaev, A. K., Lebedev, O. V. (2011) Nonadiabatic nuclear dynamics of atomic collisions based on branching classical trajectories. *Physical Review A*, 84 (1), article 014701. https://doi.org/10.1103/PhysRevA.84.014701 (In English)

Belyaev, A. K., Vlasov, D. V., Mitrushchenkov, A., Feautrier, N. (2019) Quantum study of inelastic processes in low-energy calcium–hydrogen collisions. *Monthly Notices of the Royal Astronomical Society*, 490 (3), 3384–3391. https://doi.org/10.1093/mnras/stz2763 (In English)

Belyaev, A. K., Yakovleva, S. A., Guitou, M. et al. (2016) Model estimates of inelastic calcium-hydrogen collision data for non-LTE stellar atmospheres modeling. *Astronomy & Astrophysics*, 587, article A114. https://doi.org/10.1051/0004-6361/201527651 (In English)

Brewer, M. M., Carney, B. W. (2006) A comparison of the chemical evolutionary histories of the galactic thin disk and thick disk stellar populations. *The Astronomical Journal*, 131 (1), article 431. https://doi.org/10.1086/498110 (In English)

Busso, M., Gallino, R., Lambert, D. L. et al. (2001) Nucleosynthesis and mixing on the asymptotic giant branch. III. Predicted and observed s-process abundances. *The Astrophysical Journal*, 557 (2), article 802. https://doi.org/10.1086/322258 (In English)

Chiappini, C., Gratton, A. R. (1997) The chemical evolution of the galaxy: The two-infall model. *The Astrophysical Journal*, 477 (2), article 765. https://doi.org/10.1086/303726 (In English)

Kramida, A., Ralchenko, Yu., Reader, J. et al. (2022). NIST Atomic Spectra Database (ver. 5.10). *National Institute of Standards and Technology*. [Online]. Available: https://doi.org/10.18434/T4W30F (accessed 23.04.2023). (In English)

Olson, R. E., Smith, F. T., Bauer, E. (1971) Estimation of the coupling matrix elements for one-electron transfer systems. *Applied Optics*, 10 (8), 1848–1855. https://doi.org/10.1364/AO.10.001848 (In English)

Serminato, A., Gallino, R., Travaglio, C. et al. (2009) Galactic chemical evolution of the s-process from AGB stars. *Publications of the Astronomical Society of Australia*, 26 (3), 153–160. https://doi.org/10.1071/AS08053 (In English)

Travaglio, C., Galli, D., Gallino, R. et al. (1999) Galactic chemical evolution of heavy elements: From barium to europium. *The Astrophysical Journal*, 521 (2), article 691. https://doi.org/10.1086/307571 (In English)

Vlasov, D. V., Rodionov, D. S., Belyaev, A. K. (2018) The hybrid diabatization method and its application to the CaH quasi-molecule. *Optics and Spectroscopy*, 124 (5), 611–617. https://doi.org/10.1134/S0030400X18050223 (In English)

Yakovleva, S. A., Voronov, Ya. V., Belyaev, A. K. (2016) Atomic data on inelastic processes in low-energy beryllium-hydrogen collisions. *Astronomy and Astrophysics*, 593, article A27. https://doi.org/10.1051/0004-6361/201628659 (In English)

Physics of Complex Systems, 2023, vol. 4, no. 3
www.physcomsys.ru

Physics of Semiconductors. Phase equilibria and phase transitions

UDC 538.9
EDN QMUSSM
https://www.doi.org/10.33910/2687-153X-2023-4-3-131-138

Admittance of AgI films in the temperature range of the semiconductor-superionic phase transition

A. V. Ilinskiy[1], R. A. Castro Arata[2], V. A. Klimov[1], A. A. Kononov[2], M. E. Pashkevich[3], I. O. Popova[2], E. B. Shadrin✉[1]

[1] Ioffe Physical-Technical Institute, 26 Politekhnicheskaya Str., Saint Petersburg 194021, Russia
[2] Herzen State Pedagogical University of Russia, 48 Moika Emb., Saint Petersburg 191186, Russia
[3] Peter the Great Saint Petersburg Polytechnic University, 29 Politekhnicheskaya Str., Saint Petersburg 195251, Russia

Authors

Aleksandr V. Ilinskiy, ORCID: 0000-0002-1548-1180, e-mail: Ilinskiy@mail.ioffe.ru

Rene Alejandro Castro Arata, ORCID: 0000-0002-1902-5801, e-mail: recastro@mail.ru

Vladimir A. Klimov, ORCID: 0000-0002-9096-7594, e-mail: vlad.a.klimov@mail.ioffe.ru

Alexey A. Kononov, ORCID: 0000-0002-5553-3782, e-mail: kononov_aa@icloud.com

Marina E. Pashkevich, ORCID: 0000-0002-3373-4129, e-mail: marpash@yandex.ru

Irina O. Popova, ORCID: 0000-0002-0822-985X, e-mail: timof-ira@yandex.ru

Evgeniy B. Shadrin, ORCID: 0000-0002-1423-2852, e-mail: shadr.solid@mail.ioffe.ru

For citation: Ilinskiy, A. V., Castro Arata, R. A., Klimov, V. A., Kononov, A. A., Pashkevich, M. E., Popova, I. O., Shadrin, E. B. (2023) Admittance of AgI films in the temperature range of the semiconductor-superionic phase transition. *Physics of Complex Systems*, 4 (3), 131–138. https://www.doi.org/10.33910/2687-153X-2023-4-3-131-138 EDN QMUSSM

Received 13 June 2023; reviewed 5 July 2023; accepted 5 July 2023.

Funding: This study was supported by the Ministry of Education of the Russian Federation as part of the state-commissioned assignment (project No. VRFY-2023-0005).

Abstract. In the temperature range (80–250) ^{0}C, the frequency dependence of the admittance of thin (90 nm) AgI films with a semiconductor-superionic phase transition has been studied. The applicability of the Debye theory for modeling the physical mechanism of the dielectric response of a material to the action of an alternating electric field is shown. It has been found that the reported experimental technique makes it possible to separately determine the parameters of the electronic and ionic components of the electrical conductivity of a superionic.

***Keywords**:* impedance, admittance, dielectric measurements, AgI, phase transition, superionic

Introduction

Dielectric spectroscopy is a method for obtaining the parameters of the electrical response of the material under study to the action of a low-frequency alternating electric field ($f \leq 10^7$Hz) (Kremer, Schonhals 2003).

The measured parameters are the frequency dependence of the current density $j(f)$ flowing through the cell of the dielectric spectrometer at voltage $v(f)$, as well as the angle between the voltage and current vectors.

For an ideal dielectric, the bias current leads the voltage in phase by an angle $\psi = \pi/2$ at any frequency. For a non-ideal dielectric, the angle ψ depends on the frequency and turns out to be smaller than $\pi/2$ by some amount $\delta(f) = \pi/2 - \psi(f)$ (Sidorovich 1984).

The angle δ(f) is measured in degrees or radians. For the analysis, however, the dimensionless quantity tg*δ*(*f*) is usually used, which is equal to the ratio of the charge carrier drift current density to the bias current density flowing through the measuring cell of a dielectric spectrometer (Macdonald 2006).

The drift current is accompanied by energy losses. It follows from this that the smaller the angle *δ*(*f*), the lower the energy loss. Therefore, the value of tg*δ*(*f*) is positioned as the tangent of the dielectric loss angle (Fröhlich 1958).

Recently, dielectric spectroscopy has been rapidly developed in connection with the creation of industrial dielectric spectrometers with high sensitivity, equipped with high-speed computers with modern software (Egorov et al. 2018). Spectrometers calculate a large number of dielectric parameters based on $j(f)$ and tg$\delta(f)$. Namely, the frequency dependences of the complex permittivity $\varepsilon^*(f)$, complex resistance $z^*(f)$, complex conductivity $\sigma^*(f)$, electric capacitance of the cell, etc., are calculated. No new information arises when the spectra $\varepsilon^*(f)$ are rebuilt to the spectra $z^*(f)$ or $\sigma^*(f)$. But such a restructuring allows to choose a specific type of spectra. This choice is related to the convenience of interpreting the spectra. In this case, it becomes possible to build special functional dependencies. For example, excluding such a parameter as frequency *f* from the formulas allows you to construct a function $\varepsilon''(\varepsilon')$, called the Cole-Cole diagram, or $z''(z')$, called the impedance, or $\sigma''(\sigma')$, called the admittance of the substance under study. Such dependences do not contain new information, either. Instead, they clarify specific features of the registered dielectric spectra.

This article explores the mechanism of the phase transition from the hexagonal β-phase to the cubic body-centered α-phase in thin AgI crystalline films. This transition occurs near the critical temperature of 147 ^{0}C and is a semiconductor-superionic phase transition. In the high-temperature α-phase in an external electric field, along with an increase in electronic conductivity, ionic conductivity arises. Ionic conductivity is due to the partial “melting” of the silver sublattice and the abrupt motion of silver ions along the direction of the external electric field. It turned out that these processes are clearly manifested in the dielectric spectra. The article reports and analyses the results of the study.

Experimental technique

AgI samples

We synthesized 95 nm thick nanocrystalline AgI films on 40 µm thick optical mica substrates. The first phase of synthesis was thermal deposition of an 80 nm thick layer of metallic silver on a mica substrate. At the next phase of the synthesis, thermal iodination of metallic silver was performed according to the Ag + I = AgI reaction. The mica temperature stabilized at $T = 150\ ^0$C, and crystalline iodine was sublimated at $T = 110\ ^0$C.

Dielectric measurements

Dielectric measurements were carried out with Concept 81 (Novocontrol Technologies GmbH & Co. KG, Montabaur, Germany; “Modern physical and chemical methods of formation and study of materials for the needs of industry, science and education”, Herzen University). The film under study was placed in the measuring device of the spectrometer, made in the form of a flat capacitor. The region of frequency variation corresponded to the range $f = (10^{-1} \div 10^7)$ Hz.

The frequency spectra were studied at fixed temperatures, which varied with a step of 10 ^{0}C in the range of (80–250) ^{0}C.

In this case, the frequency dependences of the real $\sigma'(f)$ and imaginary $\sigma''(f)$ parts of the complex electrical conductivity σ^* of the sample were recorded separately. For the convenience of analysis, the results of the experimental determination of $\sigma'(f)$ and $\sigma''(f)$ were presented as the admittance $\sigma''(\sigma')$ of the AgI films. In addition, the frequency dependences of the dielectric loss tangent tgδ (f) were recorded.

Since the AgI film is studied together with the substrate by the dielectric method, we performed a separate measurement of the conductivity of mica free of the AgI film. It turned out that the value of the specific conductivity of mica is small ($< 10^{-15}$ S/cm) and does not depend on the frequency of the electric field. It is independent of the sample temperature, either. Consequently, the obtained results characterize only the AgI film.

When analyzing the results of dielectric measurements, we proceeded from the fact that the electrical response of the sample is linear if a sinusoidal voltage of frequency ω and amplitude U_o is applied to the measuring cell. The linearity of the response makes it possible to apply the symbolic calculation method, when the frequency dependences of current and voltage are presented in a complex form (Tolstykh, Gozbenko 2010):

$$U(t) = U_0 \sin(\omega t) = Im\left[U^* \exp(i\omega t)\right], \tag{1}$$

$$I(t) = I_0 \sin(\omega t + \phi) = Im\left[I^* \exp(i\omega t)\right], \tag{2}$$

where the symbols U^* and I^* represent the complex voltage and current amplitudes, respectively. We set $U^* = U_o$ and extract explicitly the real and imaginary parts of complex quantities. Therefore, we can write $I^* = I_0 \exp(i\phi) = I_0 \cos(\phi) + iI_0 \sin(\phi)$, where $I_0 = (I' + I'')^{1/2}$, and i is the imaginary unit. From the complex form of Ohm's law $I^*(t) = U^*(t)/Z^*$ we obtain $Z^* = [U_0 \exp(i\omega t)]/[I^* \exp(i\omega t)]$, that is $\left(Z' + iZ''\right) = \dfrac{U_0}{I' + iI''}$ or $Z' = (U_0/I_0)I'$ and $Z'' = (U_0/I_0)I''$.

The design of the dielectric spectrometer makes it possible to measure the real amplitudes U_o and I_o, as well as the tangent of the angle between the total impedance vector of the sample and the real axis. This angle coincides with the angle ϕ of the phase difference between current fluctuations through the sample and voltage fluctuations applied to the sample. That's why $tg\delta = I''/I'$. Given expressions $Z' = (U_0/I_0)I'$ and $Z'' = (U_0/I_0)I''$, we get $tg\delta = Z''/Z'$.

As mentioned above $I_0 = (I')^2 + (I'')^2$ and $tg\delta = I''/I'$. Thus, we get $I' = I_0/\,[1 + (tg\phi)^2]^{-1/2}$ and $I'' = (I_0 tg\phi)\,/\,[1 + (tg\phi)^2]^{-1/2})$, where I_o and ϕ are experimental values measured by the spectrometer for each frequency $\omega = 2\pi f$ of input voltage fluctuations. The frequency f varies in the range $f = 10^1 – 10^6$ Hz. This allows us to experimentally determine the real and imaginary parts of the complex impedance Z^* according to the expressions $Z' = (U_0/I_0)I'$ and $Z'' = (U_0/I_0)I''$.

The design of the measuring cell of the spectrometer is such that the inductive component of the total impedance of the film sample is negligibly small. It follows from this that when analyzing the frequency dependence of the reactive component of the complex impedance Z^*, only the complex electrical capacitance C^* of the measuring cell with the sample should be taken into account. Therefore, the complex permittivity of the sample $\varepsilon^* = \varepsilon' + i\varepsilon''$ is introduced into consideration, which is obtained from the relationship $Z^* = 1/(i\omega C^*) = 1/(i\omega C_0\varepsilon^*)$. After that, simple calculations lead to the expression $\varepsilon' + i\varepsilon'' = 1/(\omega C_0 Z'' + i\omega C_0 Z'))$. Getting rid of the imaginary in the denominator and equating to each other the real and imaginary parts of ε^*, we obtain the relations:

$$\varepsilon' = -Z''/\left\{\omega C_0\left[\langle Z''\rangle^2 + \langle Z'\rangle^2\right]\right\}, \tag{3}$$

$$\varepsilon'' = -Z''/\left\{\omega C_0\left[\langle Z''\rangle^2 + \langle Z'\rangle^2\right]\right\}, \tag{4}$$

where Z' and Z'' are the real and imaginary parts of the complex impedance of the sample, thus determined for each frequency ω of input voltage oscillations.

Taking into account expressions $Z' = (U_0/I_0)I'$ и $Z'' = -(U_0/I_0)I''$ and expressions $I' = I_0/\,[1 + (tg\phi)^2]^{-1/2}$ and $I'' = (I_0 tg\phi)/\,[1+(tg\phi)^2]^{-1/2}$, we get a connection between ε', ε'' and measured quantities I_o, U_o and ϕ:

$$|\varepsilon'| = (I_0 tg\phi)/\left[\omega C_0 U_0\left(1 + (tg\phi)^2\right)^{-1/2}\right], \tag{5}$$

$$|\varepsilon''| = I_0/\left[\omega C_0 U_0\left(1 + (tg\phi)^2\right)^{-1/2}\right]. \tag{6}$$

The use of the general formulas of complex analysis (Krantz et al. 1999) allows us to proceed to obtain the real part $\sigma'(f)$ and the imaginary part $\sigma''(f)$ of the specific conductivity.

Experimental results

Fig. 1 shows the frequency spectra of the real part $\sigma'(f)$ (a) and the imaginary part $\sigma''(f)$ (b) of the specific conductivity of the spectrometer cell with the AgI film. The measurements were carried out at fixed temperatures near b→α phase transition (140 ^{0}C < T < 167 ^{0}C). In this case, the measurements were carried out with a step of 3 ^{0}C. At the first stage, the sample was heated from 140 ^{0}C to 167 ^{0}C, and then cooled to 140 ^{0}C in order to register a thermal hysteresis loop. In addition, with a wider step equal to 10 ^{0}C, the dielectric spectra of the AgI film were measured at higher temperatures of up to 250 ^{0}C.

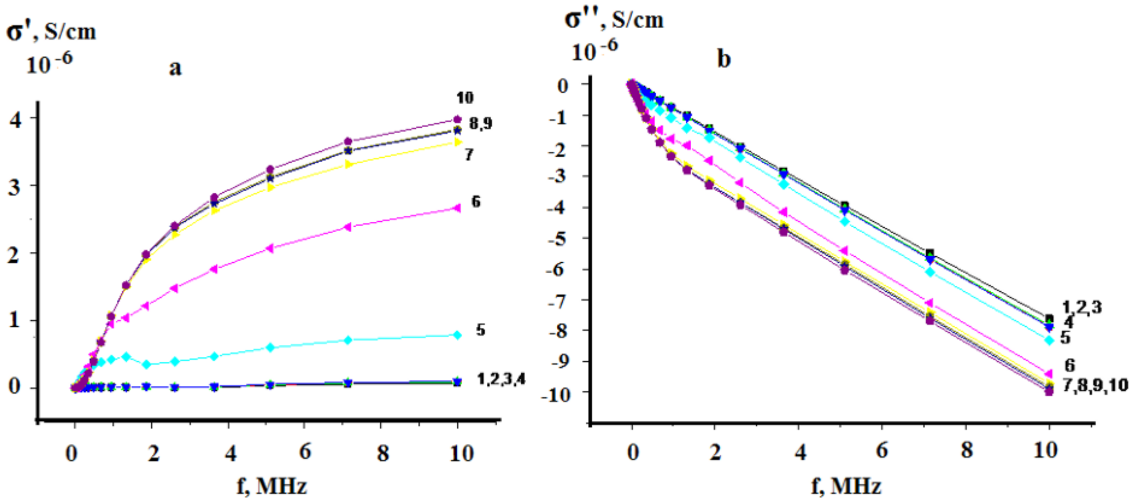

Fig. 1. Frequency dependences of the real *σ'*(*f*) and imaginary *σ''*(*f*) parts (b) of the specific conductivity of a spectrometer cell containing a sample of silver iodide (AgI). 1—140, 2—143, 3—146, 4—149, 5—152, 6—155, 7—158, 8—161, 9—164, 10—167 ^{0}C

Fig. 1a shows the dependence of the spectra *σ'*(*f*) on temperature (curves 1–10). The strongest dependence was observed near the temperature b→α phase transition (curves 4–7). It turned out that the specific conductivity *σ'*(*f*) has the highest value at high frequencies (*f* = 1 GHz). The imaginary part of the conductivity *σ''*(*f*) at frequencies *f* > 1 MHz linearly increases in absolute value with increasing frequency (Fig. 1b). At low frequencies (*f*→0) the imaginary part tends to 0 (*σ''*(*f*)→0 at *f*→0). However, in Fig. 1a, the features of the spectra *σ'*(*f*) at low and medium frequencies are not clearly visible. Therefore, for the convenience of analysis, these spectra are presented in Fig. 2 on a double logarithmic scale. Fig. 2 shows that the graphs of the functions *s'*(*f*) at medium frequencies have a complex shape. Since the reason for the mutual intersection at frequency *f* = 104 Hz of the graphs of the functions *σ'*(*f*) recorded at different temperatures remains unclear, the analysis of the results of these experiments requires additional research.

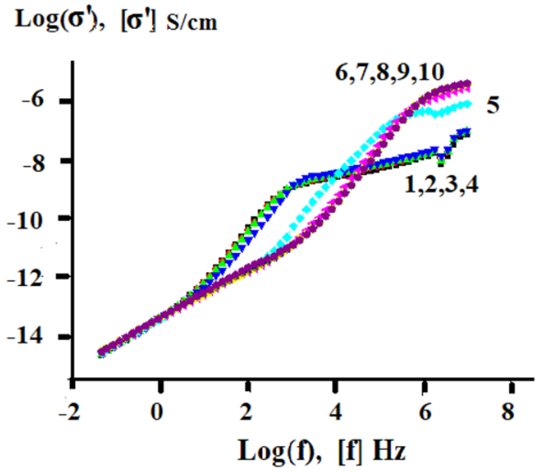

Fig. 2. Log-log frequency dependence of the real *σ'*(*f*) part of the conductivity of a spectrometer cell containing a sample of silver iodide (AgI). 1—140, 2—143, 3—146, 4—149, 5—152, 6—155, 7—158, 8—161, 9—164, 10—167 ^{0}C

To facilitate the analysis of the dielectric spectra, we performed their rearrangement in the form of Cole-Cole diagrams $\varepsilon''(\varepsilon')$, complex impedance $Z''(Z')$ and complex conductivity admittance $\sigma''(\sigma')$. Fig. 3 shows a graph of the complex admittance, that is, the dependence of the imaginary part of the conductivity σ'' on its real part σ'.

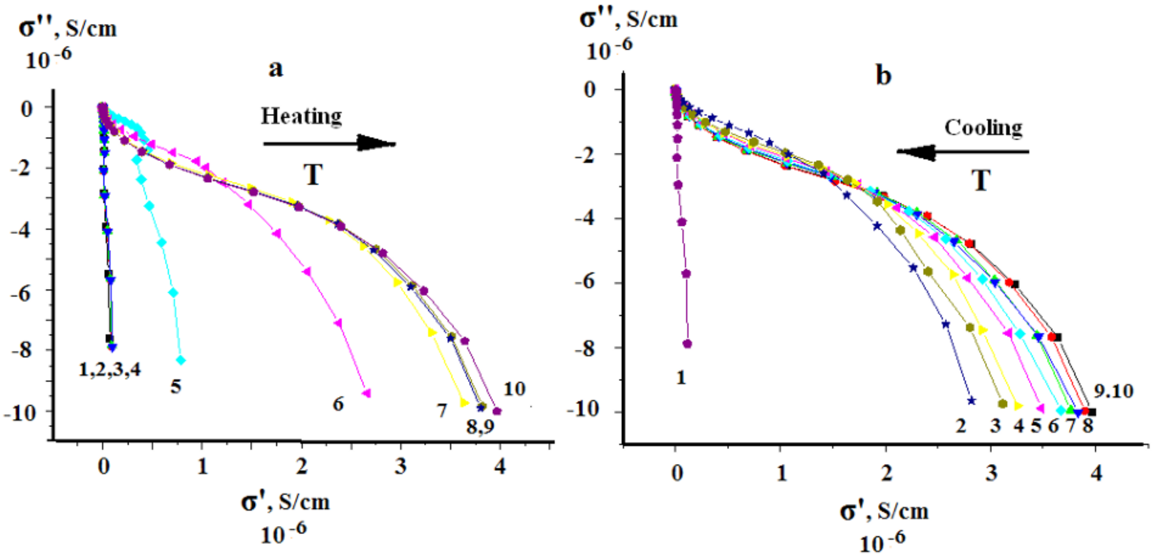

Fig. 3. Admittance $s''(s')$ of the specific conductivity of a spectrometer cell containing a silver iodide (AgI) sample in the temperature range of 140–167 0C: a—heating, b—cooling. 1—140, 2—143, 3—146, 4—149, 5—152, 6—155, 7—158, 8—161, 9—164, 10—167 ^{0}C

Fig. 4a shows the frequency dependences of the dielectric loss tangent tg$\delta(f)$ in a wide temperature range (80 < T < 240 ^{0}C).

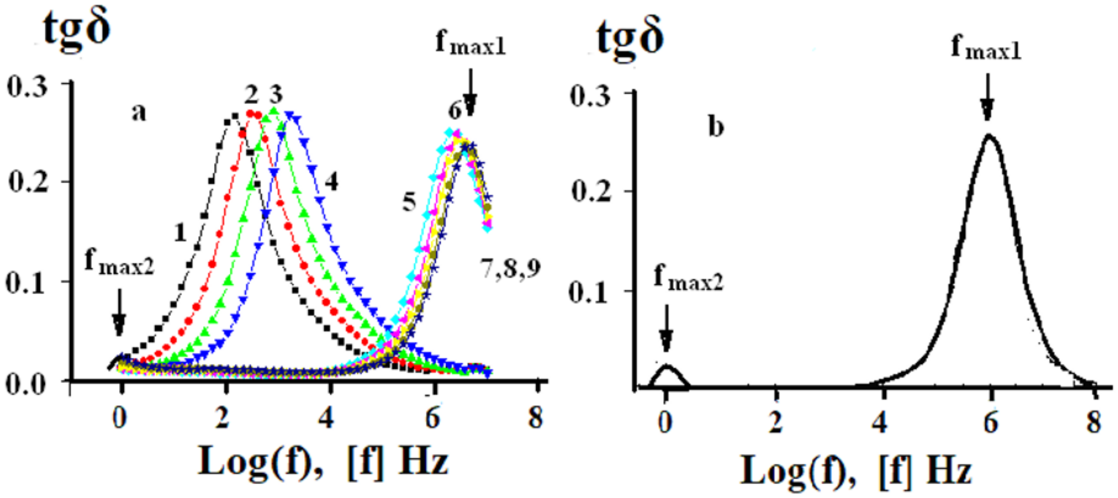

Fig. 4. Frequency dependences of the dielectric loss tangent tg$\delta(f)$: a) experiment for T = 80 – 240 ^{0}C (1—80, 2—100, 3—120, 4—140, 5—160, 6—180, 7—200, 8—220, 9—240 ^{0}C), b) calculation with formula tg$\delta(f) = \varepsilon''(f)/\varepsilon'(f)$ for T = 240 ^{0}C

Admittance $\sigma''(\sigma')$ of AgI films in the temperature range of 140–160 ^{0}C is a system of graphs approaching the real axis σ' at high frequencies (Fig. 3a—heating, Fig. 3b—cooling). Fig. 3 shows the difference in the graphs of the functions $\sigma''(\sigma')$ for different temperatures. Extrapolation of the graphs to the real axis σ' ($f \to \infty$) makes it possible to determine the specific conductivity σ(T) of the AgI film for different temperatures. Note that the admittance of silver iodide films $\sigma''(\sigma')$ at high temperatures T = (200, 210, 220, 230, 240, 250) ^{0}C reveals an additional feature at low frequencies (Fig. 5).

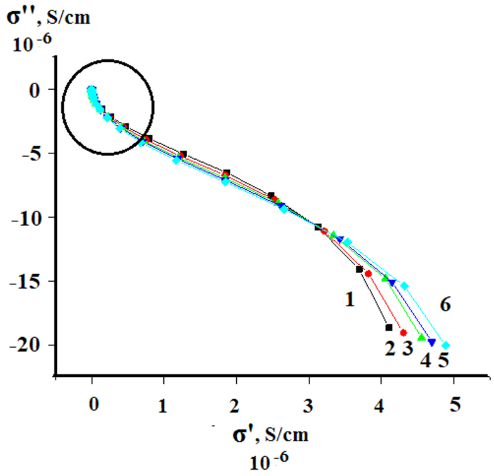

Fig. 5. Admittance *s*”(*s*’) of the specific conductivity of a spectrometer cell containing a sample of silver iodide (AgI), in the temperature range 210–250 ⁰C. (1—210, 2—220, 3—230, 4—240, 5—250 ⁰C)

The spectrum tg*δ*(*f*) (Fig. 4a) has a maximum at the frequency f_{max1} corresponding to the relaxation time $τ_1$ = 1/2pf_1. The position of the maximum of the function tg*δ*(*f*) depends on the temperature and is located at the frequency f_{max1} =100 Hz at *T* = 80 °C. Its absolute value is tg*δ*(f_{max1}) = 0.27. As the temperature increases, this maximum shifts towards higher frequencies without changing the absolute value. In the temperature range of 140–160 ⁰C (curves 4,5, Fig. 4a) there is an abrupt increase in the frequency position of this maximum. With further heating (up to 240 ⁰C), a second weak maximum tg*δ*(*f*) appears in the low-frequency region (curves 8, 9). It is located at the frequency f_{max2} = 1 Hz. Consequently, the spectral dependence tg*δ*(*f*) at high temperatures is characterized by two relaxation times: $τ_1$(T) and $τ_2$(T). When the spectrometer cell is cooled, the maximum tg*δ*(*f*) returns to its original positions, but with a temperature delay of 10 ⁰C.

Fig. 6 shows thermal hysteresis loops for f_{max1}(*T*), *σ*(T), and *σ*’(T). The values of *σ*(T) are determined from the frequency position f_{max1} of the maximum of dielectric loss tangent using the formula $τ_M$=1/(2pf_1). This uses the definition of the Maxwellian relaxation time in the form $t_M = ee_o / σ$. The specific conductivity *σ* (T) of the AgI film is determined from Fig. 3 by extrapolating the imaginary part *σ*” to the real axis *σ*’. The loop width is taken to be the temperature difference corresponding to those points of the heating and cooling branches of the loop, which are located at half the height of the frequency jump. The experiment showed that the widths of all three loops are equal to 10 ⁰C. The shape and height of the loops also coincide (Figs. 6b and 6c) within experimental errors (5%).

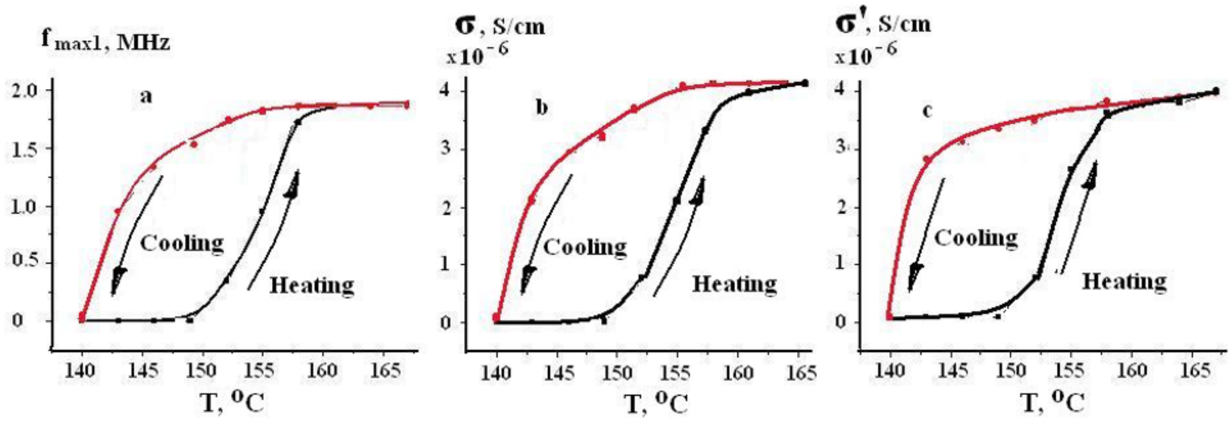

Fig. 6. Temperature hysteresis loops. Fig. 6a. Frequency position f_1 of maximum 1 dielectric loss tangent;
Fig. 6b. Conductivity *σ* of an AgI film, determined from Fig. 6a using the formula $σ_M = ee_o/τ_M = ee_o$ × 2p*f*;
Fig. 6c. Conductivity *σ*’ of the AgI film, determined from Fig. 3 by extrapolation of the imaginary part *σ*” to the real axis *σ*’

Calculation results

Creating a model of the reaction mechanism of a thin film of silver iodide to an applied low-frequency sinusoidal electric field requires the calculation of the functions $\varepsilon'(f)$ and $\varepsilon''(f)$. In the reported study, this calculation was carried out on the basis of the Debye theory. After performing the calculation, the frequency dependence of the function $\mathrm{tg}\delta(f) = \varepsilon''(f)/\varepsilon'(f)$ was plotted.

The calculations are performed for a system with two types of relaxators with relaxation times τ_1 and τ_2. This kind of model of a relaxing system makes it possible to apply the expression for $\varepsilon^*(\omega)$ in the form

$$\varepsilon^*(\omega) = \varepsilon_\infty + \frac{\Delta\varepsilon_1}{1+(i\omega\tau_1)} + \frac{\Delta\varepsilon_2}{1+(i\omega\tau_2)} \quad , \tag{7}$$

ε_∞—high-frequency limit of the real part of the permittivity ε^*, $\Delta\varepsilon_1$ и $\Delta\varepsilon_2$—jumps in the real part ε^*, $\omega = 2\pi f$—cyclic frequency.

Fig. 4b reproduces on a logarithmic scale the graphical representation of the function $\mathrm{tg}\delta(f) = \varepsilon''/\varepsilon'$ based on expression (7). Dependence $\mathrm{tg}\delta(f)$ has two maxima at frequencies $f_{\max1}$ and $f_{\max2}$. The parameters of formula (7) correspond to experimental data at $T = 240\ {}^0$C. At this temperature, the high-frequency and low-frequency features of the DS are clearly expressed in the experiment. Comparison of plots of experimental (Fig. 4a, curve 9) and calculated functions $\mathrm{tg}\delta(f) = \varepsilon''/\varepsilon'$ (Fig. 4b) confirms the applicability of the Debye theory for a qualitative explanation of the shape of the experimental dielectric spectra of AgI (Figs. 1–3).

Results and discussion

According to our model, the experimental features of the function $\mathrm{tg}\delta(f)$ are determined by the physical properties of the relaxators. Specifically, high frequency features are determined by free electrons; low frequency features are determined by positively charged free silver ions. The relaxation times in this model coincide with the Maxwellian relaxation times $\tau_M = \varepsilon\varepsilon_o/\sigma$. Here, σ is the electrical conductivity of the material.

The expression for the Maxwellian relaxation time makes it possible to transform the thermal hysteresis loop $f_{\max1}(T)$ (Fig. 6a) into the hysteresis loop of the electrical conductivity $\sigma(T)$ of the crystal (Fig. 6b). Comparison of the characteristics of the hysteresis loops of electrical conductivity (Fig. 6b and Fig. 6c) shows the qualitative and quantitative agreement of these characteristics. Loop parameters (Fig. 6c) were obtained by calculating the electrical admittance of the AgI films (Fig. 3). The obtained agreement confirms the legitimacy of using the concept of Maxwellian relaxation time for analysis.

For free silver ions at $T = 240\ {}^0$C the Maxwellian relaxation time is very long $\tau_{M2} = 1.6 \times 10^{-1}$ s ($f_{\max2} = 1$ Hz—line 9, Fig. 4a).

At T=80 ^{0}C, that is, away from temperatures g→β and b→α phase transitions, the Maxwellian relaxation time is large: $\tau_{M1}=1.6 \times 10^{-3}$ s ($f_{\max1} = 10^3$ Hz and $f_{\max1} = 10^6$ Hz—lines 4, 5, Fig. 4a), 150 ^{0}C Maxwellian time decreases by several orders to $\tau_{M1} = 1.6 \times 10^{-7}$ s near these phase transitions at $T = (140 \div 150)\ {}^0$C.

The difference of several orders of magnitude between the Maxwellian relaxation times of free electrons and free silver ions is due to the fact that the electrical conductivity of the material is due to two types of free charge carriers. It is expressed by the formula $\sigma = en_e\mu_e + qn_q\mu_q$, where e and q are the charges of the electron and silver ion, while n_e, n_q and m_e, m_q are their concentration and drift mobility, respectively. The difference in the numerical values is due to the large difference in the drift mobilities of free electrons and ions.

An increase in the rate of thermal generation of free electrons reduces the Maxwellian relaxation time and shifts the maxima of the function $\mathrm{tg}\delta(f)$ in the direction of increasing frequency. In addition, at a temperature higher than the a→β phase transition temperature, quasi-free silver ions appear. Therefore, the electrical conductivity of the AgI crystal acquires an additional ionic character. Consequently, the strong difference in the frequency position of the maxima of the function $\mathrm{tg}\delta(f)$ confirms the possibility of using the dielectric spectroscopy method to separately study electronic and ionic processes in superionics.

Due to the above reasons the integrity of the superionic crystal is preserved despite the presence of free silver ions, which provide the ionic conductivity of the superionic.

For the α-phase, both the Ag+ ion and the I⁻ ion are at the centers of the cubes of their Bravais lattices. Each of the ions forms eight hybrid orbitals capable of forming seven low-strength donor-acceptor (coordination) bonds and one high-strength sigma bond. We are talking about the bonds between ions of opposite sign located at the corners of the cube of the Bravais lattices. In this case, the Ag atom donates only one electron taken from the $5s^1$ atomic orbital to eight hybrid orbitals. To create hybrid orbitals, he gives away seven of his empty $4f^0$ orbitals. Atom I, on the contrary, gives 15 electrons to eight hybrid orbitals.

Namely, it donates one electron from the $5p_z^{\,1}$ atomic orbital and 14 electrons from the rest of the orbitals participating in the hybridization. Thus, for eight Ag-I sigma bonds, there are, as required by the theory, a total of 16 electrons. But since the Ag atom donates only one electron, out of eight bonds, only one bond turns out to be a high-strength sigma bond of the usual type. This bond is formed by introducing into it one electron from each of the Ag^+ and I^- ions. The remaining seven electron-free $4f^0$ orbitals of the Ag ion receive 14 electrons donated by the I atom. Therefore, the remaining seven bonds turn out to be low-strength donor-acceptor bonds. At the same time, inside the ion-conducting channels, along which quasi-free Ag^+ ions move, all eight bonds are low-strength coordination bonds.

Thus, the obtained results show that drift ionic conduction arises in the α-phase of an AgI crystal in an external electric field. This conductivity arises due to directed jumps of “mobile” silver ions between crystal cells located along ion-conducting channels (see Fig. 7).

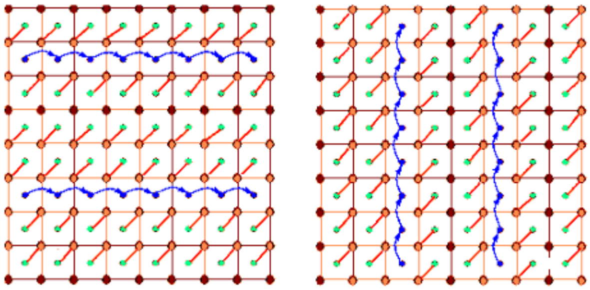

Fig. 7. Schematic representation of polytypes and ion-conducting channels

Conflict of Interest

The authors declare that there is no conflict of interest, either existing or potential.

Author Contributions

All the authors discussed the final work and took an equal part in writing the article.

References

Egorov, N. V., Karpov, A. G., Yanovskiy, V. V. (2018) Sistema issledovaniya dielektricheskikh materialov s pomoshch’yu shirokopolosnoj dielektricheskoj spektrometrii [System for research of dielectric materials by broadband dielectric spectrometry]. *Izvestiya SPbGETU “LETI” — Proceedings of Saint Petersburg Electrotechnical University*, 7, 31–37. (In Russian)

Fröhlich, H. (1958) *Teoriya dielektrikov [Theory of dielectrics]*. Moscow: “Izdatel’stvo inostr. lit.” Publ., 341 p. (In Russian)

Krantz, S. G., Kress, S., Kress, R. (1999) *handbook of complex variables*. Boston: Birkhäuser Publ., 792 p. (In English)

Kremer, K., Schonhals, A. (2003) *Broadband dielectric spectroscopy*. Berlin: Springer Publ., 729 p. https://doi.org/10.1007/978-3-642-56120-7 (In English)

Macdonald, D. D. (2006) Reflections on the history of electrochemical impedance spectroscopy. *Electrochimica Acta*, 51 (8-9), 1376–1388. https://doi.org/10.1016/j.electacta.2005.02.107 (In English)

Sidorovich, A. M. (1984) Dielektricheskaya spektr vody [Dielectric spectrum of water]. *Ukrainskij fizicheskij zhurnal*, 29 (8), 1175–1181. (In Russian)

Tolstykh, O. D., Gozbenko, V. E. (2010) *Kompleksnye chisla [Complex numbers]*. Irkutsk: IrGUPS Publ., 64 p. (In Russian)

Physics of Semiconductors. Semiconductors

UDC 538.9

EDN LUCXDA
https://www.doi.org/10.33910/2687-153X-2023-4-3-139-143

Mössbauer spectroscopy of ^{67}Zn impurity atoms in lithium and rubidium halides

G. A. Bordovsky[1], A. V. Marchenko[1], K. U. Bobokhuzhaev[2], V. S. Kiselev[1], P. P. Seregin✉[1]

[1] Herzen State Pedagogical University of Russia, 48 Moika Emb., Saint Petersburg 191186, Russia
[2] Chirchiq State Pedagogical Institute of Tashkent Region, 104 Amir Temur Ave., Chirchik, Uzbekistan

Authors
Gennady A. Bordovsky, ORCID: 0000-0002-8520-6758, e-mail: president@herzen.spb.ru
Alla V. Marchenko, ORCID: 0000-0002-9292-2541, e-mail: al7140@rambler.ru
Kudrat U. Bobokhuzhaev, e-mail: qudratman@mail.ru
Valentin S. Kiselev, e-mail: kiselev.valentin@gmail.com
Pavel P. Seregin, ORCID: 0000-0001-5004-2047, e-mail: ppseregin@mail.ru

For citation: Bordovsky, G. A., Marchenko, A. V., Bobokhuzhaev, K. U., Kiselev, V. S., Seregin, P. P. (2023) Mössbauer spectroscopy of ^{67}Zn impurity atoms in lithium and rubidium halides. *Physics of Complex Systems*, 4 (3), 139–143. https://www.doi.org/10.33910/2687-153X-2023-4-3-139-143 EDN LUCXDA

Received 26 May 2023; reviewed 22 June 2023; accepted 22 June 2023.

Funding: The study did not receive any external funding.

Abstract. Central shifts of the Mössbauer emission spectra on impurity atoms ^{67}Cu(^{67}Zn) in the crystal lattices of lithium and rubidium halides are determined. Relativistic Doppler shifts of the spectra are calculated and, as a result, isomeric shifts are obtained. The are compared with the nature of the chemical bond of zinc atoms with halogen atoms in the crystals under study. The values of the quadrupole interaction constants for zinc impurity centers in lithium and rubidium halide are consistent with the values obtained in the ionic model calculations.

***Keywords**:* crystals of lithium and rubidium halides, impurity zinc atoms, Mössbauer spectroscopy, relativistic Doppler shifts, isomeric shifts, central shifts

Introduction

One of the advantages of Mössbauer spectroscopy (MS) is the ability to determine the valence and coordination states of the probe atom, as well as the symmetry of its local environment, based on the values of the isomeric shift *(IS)* and quadrupole splitting (*QS*) of the spectrum. The Mössbauer isotope ^{67}Zn with an isomeric transition energy of 93.3 keV is of particular interest in this regard. Firstly, it has the smallest natural spectral line width of 0.32 μm/s among all other isotopes (the value of 3.1 microns/s has been experimentally achieved). Secondly, the high value of the spin of its ground state $I = 5/2$ makes it possible to extract complete information about the quadrupole interaction tensor of the nucleus from the experimental spectrum, i. e., its main value and the asymmetry parameter (Mitchell et al. 1993; Terukov et al. 2018).

However, it should be borne in mind that only the central shift *CS* can be determined directly from the experimental Mössbauer spectrum, which is the sum of the isomeric shift *IS* and the relativistic Doppler shift *DS*

$$CS = IS + DS. \quad (1)$$

Thus, to determine the values of the isomeric shift of the Mössbauer spectra (MS) of ^{67}Zn, which carries basic information about the electronic structure of zinc centers, it is necessary to take into account *DS*, which significantly limits the practical use of MS on the ^{67}Zn isotope in solid state physics, since the calculation of *DS* for ^{67}Zn is still an unsolved theoretical problem. Attempts to use model vibrational spectra in theoretical calculations of *DS* (e. g., the Debye model) did not give satisfactory results (Forster et al. 1980) and, therefore, the authors (Mitchell et al. 1993), when studying oxides, chalcogenides and zinc fluoride by the MS method on the ^{67}Zn isotope, calculated the *DS* values for each compound using complex lattice-dynamic models. However, this approach can hardly be used for routine interpretation of spectra. In addition, such calculations will require even more complication in the case of impurity probe atoms.

In this paper, a Mössbauer study of ^{67}Zn impurity atoms in the crystal lattices of lithium and rubidium halides was carried out in order to obtain information simultaneously on the central, isomeric and Doppler shifts of the Mössbauer ^{67}Zn spectra. The principal possibility of calculating the quadrupole interaction constant for ^{67}Zn impurity centers in lithium halides LiHal and rubidium RbHal (Hal = F, Cl, Br, I) within the ion model of point charges is also demonstrated.

Experiments

The Mössbauer sources were prepared by diffusion of ^{67}Cu into lithium and rubidium halide tablets pressed from powders. For this purpose, a solution of the non-bearing $^{67}CuC1_2$ in 0.1 N HCl was applied to the surface of the tablet, which was then dried and annealed in halogen. The Mössbauer spectra of ^{67}Cu(^{67}Zn) were taken at 4.2 K with a ZnS absorber. The central and isomeric shifts are attributed to a ZnO absorber with a wurtzite structure at 4.2 K.

Results and discussion

The ^{67}Cu(^{67}Zn) spectra of all lithium and rubidium halide samples are quadrupole triplets corresponding to the centers of divalent zinc $^{67}Zn^{2+}$ (see Figs. 1 and 2). The parameter of asymmetry of all triplets turned out to be close to zero ($\eta_{exp} < 0.1$).

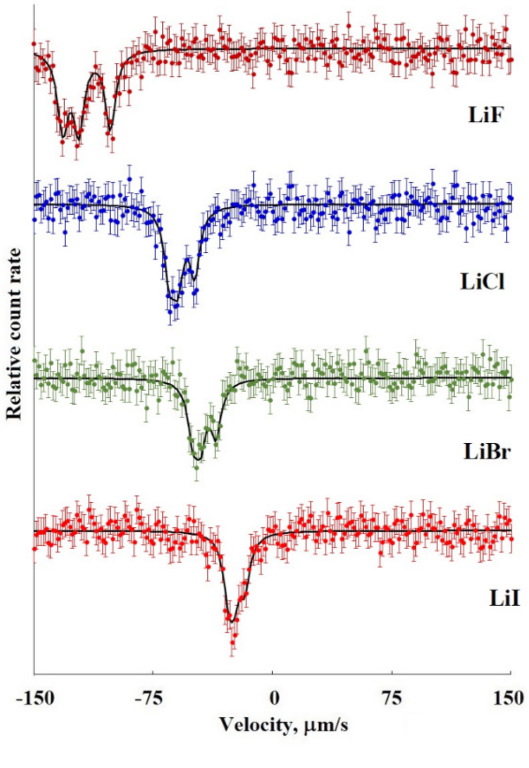

Fig. 1. Mössbauer emission spectra of ^{67}Cu(^{67}Zn) in lithium halides relative to the ZnS absorber. When measuring emission spectra, the direction of the velocity scale is rotated relative to the natural scale in such a way that higher values of the transition energy correspond to more positive velocities

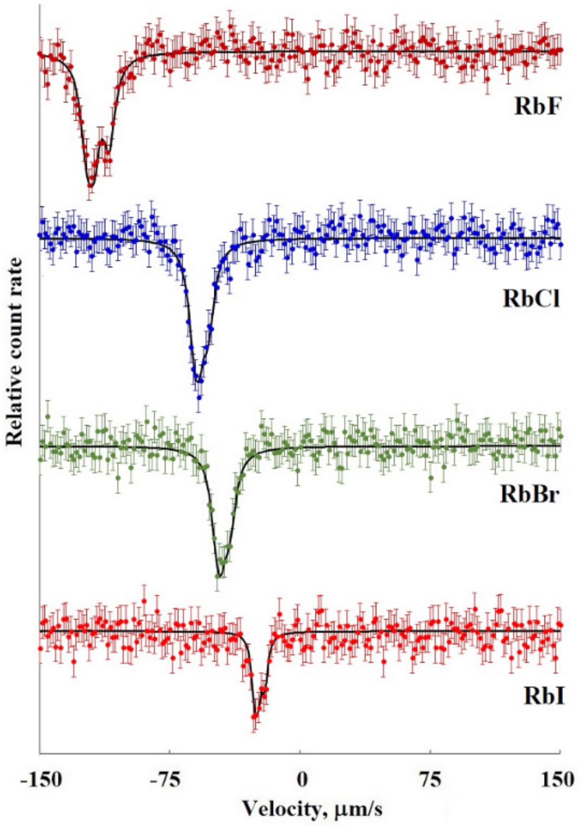

Fig. 2. Mössbauer emission spectra of ^{67}Cu(^{67}Zn) in rubidium halides relative to the ZnS absorber. When measuring emission spectra, the direction of the velocity scale is rotated relative to the natural scale in such a way that higher values of the transition energy correspond to more positive velocities

Apparently, halogen annealing of LiHal and RbHal samples doped with copper stabilizes the parent ^{67}Cu atoms in cationic positions in a divalent six-coordinated form, while the excess charge of ^{67}Cu^{2+} ions is compensated by cationic vacancies forming associates with Cu^{2+} centers. This leads to a decrease in the local symmetry of the ^{67}Zn^{2+} centers and, as a result, to the appearance of quadrupole splitting of the spectrum. This interpretation of the spectra is supported by the results reported in (Seregin et al. 2001). The study focused on the state of ^{67}Cu(^{67}Zn) impurity atoms introduced into AgCl crystals during diffusion doping in vacuum by Mössbauer spectroscopy and in the chlorine atmosphere. In the former case, Cu^{+} centers appear in the nodes of monovalent silver and Mössbauer spectrum is a singlet line corresponding to ^{67}Zn^{2+} centers in an undistorted octahedral environment of chlorine atoms. In the latter case, Cu^{2+} centers appear in the nodes of monovalent silver and the spectrum is a quadrupole triplet, corresponding to ^{67}Zn^{2+} centers in a distorted octahedral environment of chlorine atoms due to the formation of associates with Cu^{2+} centers by cationic vacancies.

The dependence of the central shift of the ^{67}Cu(^{67}Zn) spectra for lithium and rubidium halides on the difference in the Pauling electronegativity for zinc atoms and Δx ligand atoms is shown in Fig. 3 (for octahedrally coordinated zinc centers, this difference is multiplied by a factor of 1.5 to take into account the greater number of nearest neighbors of the zinc atom).

We did not use calculations to find the values of the relativistic Doppler shift *DS*. Instead, we used empirical dependences $DS = f(\Delta x)$ for four and six coordinated zinc centers, established from the analysis of data on the values of *DS* and Δx for oxides, chalcogenides and zinc fluoride (Mitchell et al. 1993). The *DS* values obtained this way make it possible, using ratio (1), to determine the isomeric shifts of the *IS* of the Mössbauer spectra of ^{67}Zn impurity atoms in copper and sodium halides. Such *IS* estimates do not claim to be more accurate, since the authors (Mitchell et al. 1993) indicate errors of ± 8 miμ/s for the *DS* values calculated by them, but they allow us to identify trends in *IS*. Fig. 3 shows the dependence $IS = f(\Delta \mathrm{x})$, which indicate a linear correlation between the isomeric shifts of the Mössbauer spectra of ^{67}Zn impurity atoms in the octahedral positions of the crystal lattices of lithium and rubidium halides and the degree of ionization of the chemical bond of zinc and chalcogen atoms.

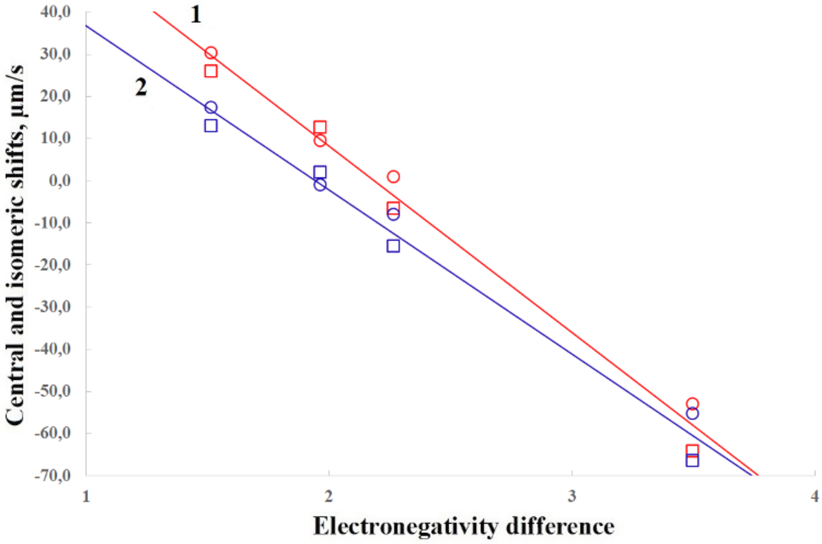

Fig. 3. Dependences of the central shift *CS* (line 1) and isomeric shift *IS* (line 2) relative to ZnO (wurtzite) from the difference of electronegativity of atoms for lithium halides (squares) and rubidium (circles)

The spatial localization of the cationic vacancy in the local environment of the ^{67}Zn^{2+} center can be established by comparing the experimental parameters of the nuclear quadrupole interaction (NQI) determined by the MS methods on the ^{67}Zn isotope and the parameters of the electric field gradient tensor calculated in the point charge model. The parameters of the NQI are the quadrupole interaction constant $C_{\text{exp}} = eQU_{zz}$ (here, eQ is the quadrupole moment of the probe core) and the parameters of the diagonalized electric field gradient (EFG) tensor on ^{67}Zn^{2+} probe cores in the crystal lattice are the main component U_{zz} and the asymmetry parameter $\eta = (U_{xx} - U_{yy})/U_{zz}$, where the components of the EFG tensor U_{xx}, U_{yy}, U_{zz} are related by the ratios $U_{xx} + U_{yy} + U_{zz} = 0$ and $|U_{xx}| \leq |U_{yy}| \leq |U_{zz}|$. In the general case

$$eQU_{zz} = eQ(1 - \gamma)V_{zz} + eQ(1 - R)W_{zz},\ \eta = (1/U_{zz})[(1 - \gamma)V_{zz}\eta_{\text{lat}} + (1 - \text{R})W_{zz}\,\eta_{\text{val}}], \tag{2}$$

where V_{zz}, W_{zz}, U_{zz} are the main components of the lattice, valence and total EFG tensors, $\eta_{\text{lat}} = (V_{xx} - V_{yy})/V_{zz}$, $\eta_{\text{val}} = (W_{xx} - W_{yy})/W_{zz}$ are the asymmetry parameters of the lattice and valence EFG tensors, γ and R are the Sternheimer coefficients that take into account the antishielding and shielding of the gap created by external charges or internal electron shells of the probe atom.

For probes with a fully (or half) filled valence shell $W_{zz} \approx 0$, the calculation of the lattice EFG tensor can be carried out using the point charge model. Since a regular lattice of the NaCl type does not create an EFG in its nodes, the cationic vacancy in the immediate environment of the Zn center was considered the only source of the EFG. The values of the main component of the lattice EFG tensor on zinc nuclei were calculated according to the ratio $V_{zz} = 2e^*/r^3$. Here, r is the Zn-vacancy distance equal to $r_1 = a_0/2^{½}$ or $r_2 = a$ for the first and second coordination shells, and a_0 is the lattice constant. The vacancy charge e^* was considered negative and equal in modulus to the electron charge. The asymmetry parameter of the EFG tensor in agreement with the experimental spectra was assumed to be 0 due to axial symmetry. Further, the experimental constants of the quadrupole interaction were compared with the contribution of the lattice gap $C = \alpha V_{zz}$, where $\alpha = eQ(1 - \gamma)$. Fig. 4 shows the calculated dependences $C = f(V_{zz})$ for Zn^{2+} centers in the LiHal and RbHal lattices, as well as experimental values of C.

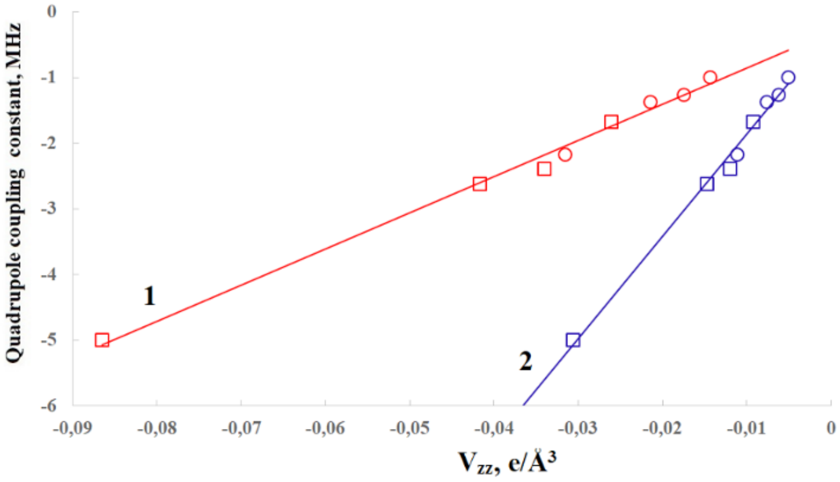

Fig. 4. Dependences of the quadrupole interaction constant on the main component of the lattice gap tensor V_{zz} for ^{67}Zn impurity atoms in lithium halides (squares) and rubidium (circles). Lines 1 and 2 correspond to vacancies in the first and second coordination spheres of impurity zinc atoms, respectively

Both dependences are linear, and it is possible to determine their angular coefficients α. For a vacancy in the first coordination shell $\alpha = (55 \pm 1)$ *MHz*·Å-3/*e*. If we take the value $\gamma = -12.2$ for the Sternheimer coefficient (Sternheimer 1966), then for the quadrupole moment of the nucleus ^{67}Zn we have $Q = 0.12(3)$ *b*, which is in agreement with the data reported in (Bieroń et al. 2018; Pyykko 2008). For a vacancy in the second coordination shell, $\alpha = (156 \pm 1)$ *MHz*.Å^{-3}/*e*, which results in $Q = 0.34(3)$ *b*. This differs significantly from the generally accepted values. The difference in the electrostatic energies of the Zn-vacancy pair $e^{2/4}\pi\varepsilon_0 r$ is 1–1.5 eV for r_1 and r_2 (0.16–0.25 eV, if we take into account the polarization of the medium using static permittivity). Apparently, this difference is sufficient to capture the vacancy during annealing at a minimum distance from the center of Zn.

Conflict of Interest

The authors declare that there is no conflict of interest, either existing or potential.

Author Contributions

All the authors discussed the final work and took an equal part in writing the article.

References

Bieroń, J., Filippin, L., Gaigalas, G. et al. (2018) Ab initio calculations of the hyperfine structure of zinc and evaluation of the nuclear quadrupole moment $Q(^{67}\mathrm{Zn})$. *Physical Review A*, 97 (6), article 062505. https://doi.org/10.1103/PhysRevA.97.062505 (In English)

Forster, A., Potzel, W., Kalvius, G. M. (1980) Mössbauer spectroscopy with the 93 keV-resonance in^{67}Zn. *Zeitschrift für Physik B Condensed Matter*, 37 (3), 209–219. https://doi.org/10.1007/BF01323034 (In English)

Mitchell, D. W., Das, T. P., Potzel, W. et al. (1993) First-principles investigation of ^{67}Zn isomer shifts in ZnF_2 and chalcogenides ZnO, ZnS, ZnSe, and ZnTe. *Physical Review B*, 48 (22), article 1649. https://doi.org/10.1103/PhysRevB.48.16449 (In English)

Pyykko, P. (2008) Year-2008 nuclear quadrupole moments. *Molecular Physics*, 106 (16-18), 1965–1974. https://doi.org/10.1080/00268970802018367 (In English)

Seregin, N. P., Nasredinov, F. S., Bondarevskii, S. I. et al. (2001) The charge state of copper impurity atoms in AgCl annealed in vacuum or chlorine. *Journal of Physics: Condensed Matter*, 13 (11), article 2671. https://doi.org/10.1088/0953-8984/13/11/321 (In English)

Sternheimer, R. M. (1966) Shielding and antishielding effects for various ions and atomic systems. *Physical Review*, 146 (1), article 140. https://doi.org/10.1103/PhysRev.146.140 (In English)

Terukov, E. I., Marchenko, A. V., Seregin, P. P. et al. (2018) Parameters of nuclear quadrupole interaction and spatial distribution of electronic defects in $YBa_2Cu_3O_7$ and $La_{2-x}Sr_xCuO_4$ lattices. *Physics of the Solid State*, 60 (10), 1908–1915. https://doi.org/10.1134/S106378341810027X (In English)

Summaries in Russian / Информация о статьях на русском языке

Физика конденсированного состояния

ПРЯМОЙ СИНТЕЗ MG_2NIH_4 ИЗ MGH_2 И NI

Барабан Александр Петрович, Дмитриев Валентин Александрович, Габис Игорь Евгеньевич, Войт Алексей Петрович, Клямкин Семен Нисонович, Шикин Илья Викторович

Аннотация. Показано, что экспозиция прессованной смеси порошков MgH_2 и Ni в атмосфере водорода при 450 °C приводит к прямому синтезу гидрида Mg_2NiH_4. Предварительный помол в шаровой мельнице не проводился. Реакция велась при давлении водорода, превышающем равновесное над MgH_2 и Mg_2NiH_4. Неизменность давления в ходе синтеза свидетельствует об отсутствии стадии разложения гидрида магния и стабильности синтезированного гидрида. Количество Mg_2NiH_4 определялось методами XRD и TDS. SEM с микроанализом EDX использовались для изучения морфологии продуктов реакции. Исследовано влияние времени экспозиции и температуры синтеза на эффективность реакции.

Ключевые слова: гидриды металлов, материалы для хранения водорода, твердотельный прямой синтез, тройной гидрид Mg_2NiH_4, интерметаллид $MgNi_2$

Для цитирования: Baraban, A. P., Dmitriev, V. A., Gabis, I. E., Voyt, A. P., Klyamkin, S. N., Shikin, I. V. (2023) Direct synthesis of Mg_2NiH_4 from MgH_2 and Ni. *Physics of Complex Systems*, 4 (3), 94–102. https://www.doi.org/10.33910/2687-153X-2023-4-3-94-102 EDN TODSJI

Теоретическая физика

ВЗАИМОДЕЙСТВИЕ ПОДСИСТЕМ В ЗАДАЧАХ НЕЛИНЕЙНОЙ ДИНАМИКИ. РАЗЛИЧНЫЕ ФАЗЫ ХАОСА

Ляпцев Александр Викторович

Аннотация. Рассматривается модель двух взаимодействующих диссипативных подсистем, описываемых уравнениями нелинейной динамики. Каждая из подсистем является нелинейным осциллятором, возбуждаемым внешним периодическим полем. Численный расчет показывает, что в данной системе могут возникать хаотические колебания, фазовые траектории которых в пределе больших времен описываются хаотическим аттрактором. Показано, что в силу симметрии системы различные начальные условия могут приводить к различным хаотическим аттракторам. Обсуждается аналогия между различными странными аттракторами данной модели и различными фазами вещества в системах с большим числом частиц.

Ключевые слова: нелинейная динамика, странный аттрактор, хаотический аттрактор, плотность вероятности, хаос, термодинамическая фаза

Для цитирования: Liaptsev, A. V. (2023) Interaction of subsystems in nonlinear dynamics problems. Various phases of chaos. *Physics of Complex Systems*, 4 (3), 103–111. https://www.doi.org/10.33910/2687-153X-2023-4-3-103-111 EDN OUAIPE

ЧИСЛЕННОЕ МОДЕЛИРОВАНИЕ ДИНАМИКИ ЭЛЕКТРИЧЕСКИ ЗАРЯЖЕННОГО МНОГОФРАКЦИОННОГО АЭРОЗОЛЯ, ДВИЖУЩЕГОСЯ В КАНАЛЕ ПОД ДЕЙСТВИЕМ СИЛЫ КУЛОНА И АЭРОДИНАМИЧЕСКИХ СИЛ

Тукмаков Дмитрий Алексеевич

Аннотация. Данная работа посвящена математическому моделированию динамики электрически заряженного аэрозоля в канале. Исследование связано с моделированием процессов работы электрического фильтра дисперсных сред. Для оптимизации технологий электрической фильтрации дисперсных сред необходимо понимание закономерностей динамики заряженных дисперсных частиц в электрическом поле. Математическая модель реализована в виде компьютерной программы. Программный код представляет собой конечно-разностный численный алгоритм решения уравнений математической модели. Моделируемая среда состоит из двух компонент: первая компонента — вязкий сжимаемый теплопроводный газ, для описания динамики

которого используется система уравнений Навье-Стокса; вторая компонента представляет собой электрически заряженные частицы. Математическая модель учитывала межкомпонентный обмен импульсом и теплом. Дисперсная составляющая аэрозоля описывалась с учетом многофракционного состава. Каждая фракция имеет свой размер частиц, плотность и теплоемкость материала. В работе предполагалось, что к стенкам канала прикладывался электрический потенциал: отрицательный потенциал прикладывался к нижней стенке, а положительный — к верхней стенке канала.

Проведены расчеты движения многофракционной электрически заряженной газовзвеси в канале. Рассматривалось два случая — в первом случае все фракции дисперсной компоненты аэрозоля имеют одну физическую плотность материла и различные размеры частиц. Второй случай — частицы имеют один размер и отличаются плотностью материала. Выявлено, что при одинаковой плотности материала вертикальная скорость частицы и интенсивность процесса осаждения больше при увеличении размера частиц. Также выявлено, что при одинаковом размере частиц более интенсивно осаждаются частицы с большей плотностью материала. Выявленные закономерности возможно использовать при оптимизации технологий электрической фильтрации дисперсных сред.

Ключевые слова: численное моделирование, аэрозоли, полидисперсная газовзвесь, электрически заряженные среды

Для цитирования: Tukmakov, D. A. (2023) Numerical simulation of the dynamics of an electrically charged multifractional aerosol moving in a channel under the action of the Coulomb force and aerodynamic forces. *Physics of Complex Systems*, 4 (3), 112–123. https://www.doi.org/10.33910/2687-153X-2023-4-3-112-123 EDN PXERKT

АТОМНЫЕ ДАННЫЕ О НЕУПРУГИХ СТОЛКНОВИТЕЛЬНЫХ ПРОЦЕССАХ В СИСТЕМЕ YH

Васильева Вера Антоновна, Яковлева Светлана Анатольевна

Аннотация. В работе рассчитаны сечения и константы скоростей неупругих процессов, происходящих при низкоэнергетических столкновениях атомов и ионов иттрия и водорода. Рассмотрены три ионных состояния . Проведены расчеты неадиабатической ядерной динамики внутри всех молекулярных симметрий, образованных каждым из ионных состояний. Исследованы неупругие процессы, происходящие за счет неадиабатических переходов между 65 различными состояниями квазимолекулы YH. Суммарно рассмотрено 1796 неупругих процессов, для которых посчитаны сечения для энергий от 0.001 до 100 эВ и константы скоростей для температур от 1000 до 10000 К. Неупругие процессы с большими значениями констант скоростей важны при астрофизическом моделировании с учетом НЛТР эффектов.

Ключевые слова: атомные данные, неупругие процессы, неадиабатические переходы, иттрий, водород

Для цитирования: Vasileva, V. A., Yakovleva, S. A. (2023) Atomic data on inelastic collisional process for YH. *Physics of Complex Systems*, 4 (3), 124–130. https://www.doi.org/10.33910/2687-153X-2023-4-3-124-130 EDN QEBNZO

Физика полупроводников

АДМИТТАНС ПЛЕНОК AGI В ТЕМПЕРАТУРНОМ ДИАПАЗОНЕ ФАЗОВОГО ПЕРЕХОДА ПОЛУПРОВОДНИК-СУПЕРИОННИК

Ильинский Александр Валентинович, Кастро Арата Рене Алехандро, Климов Владимир Александрович, Кононов Алексей Андреевич, Пашкевич Марина Эрнстовна, Попова Ирина Олеговна, Шадрин Евгений Борисович

Аннотация. В диапазоне температур (80–250) ^{0}С исследована частотная зависимость адмиттанса тонких пленок AgI (90 нм) с фазовым переходом полупроводник-суперионник. Показана применимость теории Дебая для моделирования физического механизма диэлектрического отклика материала на действие переменного электрического поля. Установлено, что использованная экспериментальная методика позволяет раздельно определять параметры электронной и ионной составляющих электропроводности суперионика.

Ключевые слова: импеданс, адмиттанс, диэлектрические измерения, AgI, фазовый переход, суперионник

Для цитирования: Ilinskiy, A. V., Castro Arata, R. A., Klimov, V. A., Kononov, A. A., Pashkevich, M. E., Popova, I. O., Shadrin, E. B. (2023) Admittance of AgI films in the temperature range of the semiconductor-superionic phase transition. *Physics of Complex Systems*, 4 (3), 131–138. https://www.doi.org/10.33910/2687-153X-2023-4-3-131-138 EDN QMUSSM

МЕССБАУЭРОВСКАЯ СПЕКТРОСКОПИЯ ПРИМЕСНЫХ АТОМОВ ^{67}ZN В ГАЛОГЕНИДАХ ЛИТИЯ И РУБИДИЯ

Бордовский Геннадий Алексеевич, Марченко Алла Валентиновна, Бобохужаев Кудрат Умарович, Киселев Валентин Сергеевич, Серегин Павел Павлович

Аннотация. Определены центральные сдвиги эмиссионных мессбауэровских спектров на примесных атомах ^{67}Cu(^{67}Zn) в кристаллических решетках галогенидов лития и рубидия, рассчитаны релятивистские доплеровские сдвиги спектров и, как результат, получены изомерные сдвиги, которые сопоставлены с характером химической связи атомов цинка с атомами галогенов в исследованных кристаллах. Величины постоянных квадрупольного взаимодействия для примесных центров цинка в галогенидах лития и рубидия согласуются с результатами расчета этих величин в рамках ионной модели.

Ключевые слова: кристаллы галогенидов лития и рубидия, примесные атомы цинка, мессбауэровская спектроскопия, релятивистские доплеровские сдвиги, изомерные сдвиги, центральные сдвиги

Для цитирования: Bordovsky, G. A., Marchenko, A. V., Bobokhuzhaev, K. U., Kiselev, V. S., Seregin, P. P. (2023) Mössbauer spectroscopy of ^{67}Zn impurity atoms in lithium and rubidium halides. *Physics of Complex Systems*, 4 (3), 139–143. https://www.doi.org/10.33910/2687-153X-2023-4-3-139-143 EDN LUCXDA